Analysis of Near-Surface Flow Measurements Beneath Clean and Contaminated Wind-Driven Water Surfaces

Mandana Jokardris

A Thesis

in

The Department

of

Mechanical and Industrial Engineering

Presented in Partial Fulfillment of the Requirements
for the Degree of Master of Applied Science (Mechanical Engineering) at
Concordia University
Montreal, Quebec, Canada

November 2004

Your file Votre référence
ISBN: 0-494-04420-9
Our file Notre référence
ISBN: 0-494-04420-9

ABSTRACT

Analysis of Near-Surface Flow Measurements Beneath Clean
and Contaminated Wind-Driven Water Surfaces

Mandana Jokardris

In natural water bodies like oceans and lakes, biological organisms and other chemical species cover the water surface affecting the air-sea boundary conditions. At moderate wind speeds, short gravity wind waves occur on the water surface. It has been speculated that most of these short gravity waves are microscale breaking waves, which play a significant role in air-sea gas and heat transfer. This work reports on results from a series of laboratory experiments investigating the impact of surface contamination on the flow characteristics in the near surface region beneath short gravity waves at moderate wind speeds. In addition, the characteristics of parasitic capillary waves and their relation with microscale breaking waves are explored. In this study, the two-dimensional velocity fields were measured using digital particle image velocimetry (DPIV) and water surface temperature measurements were made simultaneously using infrared imagery. Results are reported for two wind speeds, 6.3 and 8.1 m s^{-1}.

The results show that in the presence of surfactant, the energy of dominant wave was reduced by approximately 40% to 60%. The mean velocity profiles confirm the existence of a viscous sublayer where the mean velocity varies linearly with depth. The mean streamwise velocity gradients within the viscous sublayer were a factor of 2 to 2.3 larger beneath the surfactant-contaminated surfaces compared to the clean surfaces. The

results also indicate that the surfactant increases the waterside friction velocity by approximately 30-50%. A thin layer of enhanced vorticity was observed beneath the surfactant-contaminated surface, which coincides with the region where the mean velocity gradients were significantly larger.

The detailed characteristics of the parasitic capillary waves were also investigated. The results show that the presence of a surfactant did not affect the length and amplitude of capillary waves. However, in the presence of surfactant, the number of capillary waves was reduced by 50-70% and the number of gravity waves with parasitic capillary waves was decreased by 30-60%. A scheme was developed to detect microscale breaking waves using infrared imagery. It was found that the percentage of breaking waves was reduced by approximately 50% in the presence of a surfactant. The results also indicate that 75-95% of parasitic capillary waves appeared on the crests of incipient breaking wave. Thus, it was concluded that the capillary waves initiate the breaking process and that the reduction in the percentage of microscale breaking waves beneath the surfactant-contaminated surfaces is due to the damping of capillary waves by the surfactant.

ACKNOWLEDGMENTS

I would like to extend my sincere gratitude and thanks to my supervisors Dr. Kamran Siddiqui and Dr. Mark R. Loewen for their invaluable guidance, assistance and inspiration throughout the span of this work and for their helpful financial supports. I also want to thank M. Elkamash and M. Atmane for their help in the conducting of experiments.

CONTENTS

List of Figures.....ix

List of Tables.....xiv

Nomenclature.....xvi

CHAPTER 1 Introduction.....1

1.1 Parasitic Capillary Waves.....3

1.2 Microscale Breaking Waves.....5

1.3 Turbulent Flow Beneath Wind Waves.....9

1.4 Surfactant.....13

1.5 Objectives.....17

CHAPTER 2 Experimental Setup and Methods.....22

2.1 Experimental Setup and Instrumentation.....22

2.2 Synchronization and Collocation of the DPIV, Profile and IR Cameras.....25

2.3 Environmental Measurements.....26

2.4 Surface Temperature Measurements.....26

2.5 Wave Profile Measurements.....27

2.6 DPIV Technique.....28

2.7 Computation of the Instantaneous Velocity Field.....32

CHAPTER 3 Wind Drift Layer Characteristics.....46

3.1 Wave Properties.....46

3.2 Velocity Analysis.....47

3.2.1 Mean Velocity.....48

3.2.2 Wave Velocity.....49

3.3 Shear Stress Analysis.....51

3.3.1 Wind Stress.....51

3.3.2 Total Waterside Stress.....52

3.3.2.1 Viscous Stress.....53

3.3.2.2 Water Stress.....53

3.3.3 Friction Velocity.....54

3.3.4 Mean Velocity in Wall Coordinates.....55

3.4 Spectral Analysis.....56

3.5 Energy Dissipation.....56

3.6 Discussion and Conclusion.....59

CHAPTER 4 Parasitic Capillary Waves and Microscale Breaking Waves.....80

4.1 Parasitic Capillary Waves.....80

4.2 Detection of Microscale Breaking Waves.....85

4.3 Parasitic Capillary Waves and Microscale Breaking Waves.....89

4.4 Dynamics of Coherent Structures.....91

4.5 Discussion and Conclusion.....93

CHAPTER 5 Summary and Suggestions for Future Work 108

5.1 Summary... 108

5.2 Suggestions for Future Work 112

REFRENCES.....114

Appendix A Error Estimate for the DPIV Measurements.....119

List of Figures

Figure 1.1: (Top) A conceptual sketch of a microscale breaking wave. The characteristic feature of a microscale breaking wave is a bore-like crest preceded by capillary waves riding along the forward face. (Below) A digital video image of a microscale breaking wave with a wavelength of approximately 10 cm (Jessup 1997a).....19

Figure 1.2: A schematic showing the three phases of gentle mechanically generated breaking waves for weak and strong surface tension effects (Duncan 2001).....20

Figure 1.3: Disruption and recovery of the skin layer due to wave breaking (Jessup 1997a).....20

Figure 1.4: A thermal wake created due to the disruption of the cool skin layer by a microscale breaking wave in an IR image at 8.1 m s^{-1} wind speed. The images is 14.1 by 14.1 cm in size.....21

Figure 1.5: A typical surfactant film orientation at the air-water interface; O, the hydrophilic head; _____, the hydrophobic head.....21

Figure2.1: A schematic of the experimental setup and instrumentation in the wind-wave flume (no to scale).....35

Figure 2.2: A flow chart showing the synchronization of the DPIV, profile, and IR cameras, and the laser. The vertical sync signal from the profile camera was used to synchronize the IR and DPIV cameras. The vertical sync signal from the DPIV camera was used to synchronize the laser.....36

Figure 2.3: Flow chart showing the trigging sequence for the data acquisition.....37

Figure 2.4: (a) The rigid block with vertical shafts and a ruler. The collocation images from (b) profile camera, (c) DPIV camera, (d) IR imager.....38

Figure 2.5: (a), A digital video image from the profile camera taken at a wind speed of 8.1 m s^{-1}. The difference in the gray scale values on the airside and waterside is visible in the image; (b), The image after applying the gray-scale threshold and morphological operations; (c), The computed air-water interface (white line) over laid on the profile image.....39

Figure 2.6: The diagram showing the timing of the laser pulses in an image pair. A pulse generator controls the timing and duration of each laser pulse (Siddiqui 2002).....40

Figure 2.7: (a), A PIV image pair. Each image pair is divided into small interrogation regions; (b), Correlation plane, obtained by cross-correlating the interrogation region in the first image with the corresponding search region in the second image; (c), The peak in the correlation plane gives the average displacement of the particles within the interrogation region (figure not to scale) (Siddiqui 2002).....41

Figure 2.8: (a), A raw image from the DPIV camera. The air-water interface is clearly visible in the down wind region of the image;(b), The imported surface profile from the corresponding profile image is plotted in the DPIV image. The visible part of the interface in the DPIV image was used to determine the vertical offset for the imported surface profiles;(c), The DPIV image after setting the bright pixels above the interface equal to the background gray-scale value.....42

Figure 2.9: (a), The DPIV image corresponding to the profile image shown in figure 2.5. The air-water interface is not visible in this image due to the reflection of the tracer particles. The surface profile from figure 2.5 is imported to locate the interface and is plotted as a white line; (b), The DPIV image after preprocessing.....43

Figure 2.10: The two-dimensional instantaneous velocity field obtained by processing the DPIV image pair from figure 2.9. This velocity field is obtained after correcting the

spurious vectors. The nearest velocity was measured on average, within 0.4 mm from the water surface.....44

Figure 2.11: A two-dimensional velocity field with incorrect velocity vectors in the crest region due to the high velocity gradient at a wind speed of 8.1 m s^{-1}.....45

Figure 3.1: Frequency spectra of the surface profile; (a), at 6.3 m s^{-1} wind speed; (b), at 8.1 m s^{-1} wind speed; solid line, clean surface; dash-dotted line, contaminated surface...71

Figure 3.2: Vertical profiles of the streamwise and vertical components of the mean velocity (a) linear scale, (b) semi logarithmic scale: ○, = clean surface at 6.3 m s^{-1} wind speed; ◊, = contaminated surface at 6.3 m s^{-1} wind speed; Δ, = clean surface at 8.1 m s^{-1} wind speed; □, = contaminated surface at 8.1 m s^{-1} wind speed.....72

Figure 3.3: Vertical profiles of the RMS wave velocity components; (a), the streamwise component; (b), the vertical component; ○, = clean surface at 6.3 m s^{-1} wind speed; ◊, = contaminated surface at 6.3 m s^{-1} wind speed; Δ, = clean surface at 8.1 m s^{-1} wind speed; □, = contaminated surface at 8.1 m s^{-1} wind speed.....73

Figure 3.4: Comparison between the total waterside stress at a depth of 0.4 mm and the wind stress, at different wind speeds; (a), the clean surface; (b), the contaminated surface; Δ, = total waterside stress; ○, = wind stress.....74

Figure 3.5: The mean streamwise velocity plotted in the form of a velocity defect law in wall coordinates; $u^+ = (U_s - U) / u_*$ and $y^+ = yu_* / \nu$. ○, = clean surface at 6.3 m s^{-1} wind speed; ◊, = contaminated surface at 6.3 m s^{-1} wind speed; Δ, = clean surface at 8.1 m s^{-1} wind speed; □, = contaminated surface at 8.1 m s^{-1} wind speed.....75

Figure 3.6: Wave number spectra of the streamwise instantaneous velocity $\Phi u(k)$ at 6.3 m s^{-1} wind speed;(a), clean surface; (b), contaminated surface; ○, = 0.4 mm depth; Δ, = 4.4 mm depth; □, = 9.2 mm depth.....76

Figure 3.7: Wave number spectra of the streamwise instantaneous velocity $\Phi u(k)$ at 8.1 m s^{-1}wind speed; (a), clean surface; (b), contaminated surface; ○, = 0.4 mm depth; Δ, = 4.4 mm depth; □, = 9.2 mm depth.....77

Figure 3.8: The vertical profiles of the rate of energy dissipation, ε. ○, = clean surface at 6.3 m s^{-1} wind speed; ◊, = contaminated surface at 6.3 m s^{-1} wind speed; Δ, = clean surface at 8.1 m s^{-1} wind speed; □, = contaminated surface at 8.1 m s^{-1} wind speed.....78

Figure 3.9: Plot of the rate of energy dissipation, ε, versus the depth, ζ, normalized in wall coordinates. ○, = clean surface at 6.3 m s^{-1} wind speed; ◊, = contaminated surface at 6.3 m s^{-1} wind speed; Δ, = clean surface at 8.1 m s^{-1} wind speed; □, = contaminated surface at 8.1 m s^{-1} wind speed.....79

Figure 4.1: Vorticity field of a gravity wave at 8.1 m s^{-1} wind speed beneath clean surface. Capillary waves on the forward face of the gravity waves are clearly visible in the plot.....98

Figure 4.2: Wave number spectrum of surface displacement at a wind speed 8.1 m s^{-1} for the clean surface. The peaks in the spectrum in the range $2000 < k < 10000$ correspond to the capillary waves.....99

Figure 4.3: Wavelength of capillary waves on the forward face of gravity waves versus wind speed;(a), clean surface; (b), contaminated surface; ○, = from the wave number spectra of the surface profile; Δ, = from the visual inspection.....100

Figure 4.4: Probability density function of the capillary wave amplitude;(a), at 6.3 m s^{-1} wind speed; (b), at 8.1 m s^{-1} wind speed; solid line, clean surface; dash-dotted line, contaminated surface.....101

Figure 4.5: Probability density function of the capillary wavelength;(a), at 6.3 m s^{-1} wind speed; (b), at 8.1 m s^{-1} wind speed; solid line, clean surface; dash-dotted line, contaminated surface.....102

Figure 4.6: Probability density function of N_{c-g}, number of capillary waves per gravity wave; (a), at 6.3 m s^{-1} wind speed; (b), at 8.1 m s^{-1} wind speed; solid line, clean surface; dash-dotted line, contaminated surface.....103

Figure 4.7: (a), An IR image of the water surface temperature at 8.1 m s^{-1} wind speed. The vertical line is the location of DPIV field of view in the IR images; (b), the segmented IR image after applying the temperature threshold; dash-dotted line, the crest position; dashed line, the region of interest (ROI); solid line, the location of the DPIV camera.....104

Figure 4.8: The comparison of the time series of parasitic capillary waves and microscale breaking waves at a wind speed of 8.1 m s^{-1} for clean surface; *, time series for parasitic capillary waves; solid line, time series for microscale breaking wave crests.....105

Figure 4.9: A Sequence of DPIV vorticity fields at a wind speed of 8.1 m s^{-1} beneath clean surface.....106

Figure 4.10: A sequence of DPIV vorticity fields at a wind speed of 8.1 m s^{-1} beneath contaminated surface.....107

List of Tables

Table 2.1 Summary of the environmental parameters for different experimental runs. U_{∞}, wind speed; T_{air}, the average air temperature; RH, the average relative humidity of the air; T_{water}, the average water temperature.....34

Table 2.2: The percentages of bad frames detected by the velocity gradient scheme.....34

Table 3.1: U_{∞}, wind speed; f_d, the dominant wave frequency; λ_d, the dominant wavelength; H_{rms}, the RMS wave height; H_s, the significant wave height.....66

Table 3.2: U_{∞}, wind speed; U_s, the surface velocity; u_*, the waterside friction velocity; u_{*a}, the airside friction velocity; τ_{wind}, the wind stress; $(u_*)_{\text{visc}}$, waterside friction velocity computed from the viscous stress.....66

Table 3.3: The values of the waterside stresses for the clean surface at 6.3 m s^{-1} wind speed; τ_{total}, the magnitude of total shear stress; τ_{wave} , the magnitude of wave stress; τ_{visc}, the magnitude of viscous stress.....67

Table 3.4: The values of the waterside stresses for the contaminated surface at 6.3 m s^{-1} wind speed; τ_{total}, the magnitude of total shear stress; τ_{wave} , the magnitude of wave stress; τ_{visc}, the magnitude of viscous stress.....68

Table 3.5: The values of the waterside stresses for clean surface at 8.1 m s^{-1} wind speed; τ_{total}, the magnitude of total shear stress; τ_{wave} , the magnitude of wave stress; τ_{visc}, the magnitude of viscous stress.....69

Table 3.6: The values of the waterside stresses for contaminated surface at 8.1 m s^{-1} wind speed; τ_{total}, the magnitude of total shear stress; τ_{wave} , the magnitude of wave stress; τ_{visc}, the magnitude of viscous stress.....70

Table 4.1: Table 4.1: U_∞, wind speed; λ, wavelength of capillary waves; a, amplitude of capillary waves; ω, absolute vortices beneath capillary waves; N_{GC}, number of gravity waves with capillary waves; N_C, number of capillary waves; $Nc\text{-}g$, average number of capillary waves on the crest of a gravity wave.....96

Table 4.2: F_t; threshold for the fraction of the ROI occupied by the wake; N_{DPIV}, number of breaking waves detected from DPIV vorticity fields; N_{IR}, number of breaking waves detected from IR images; N_{CM}, number of breaking waves detected commonly by both methods; C_{bw}, percentage of commonly detected breaking waves.....97

Table 4.3: U_∞, the wind speed; P_{bw}, percentage of microscale breaking waves.....97

Table 4.4: U_∞, wind speed; $\overline{\omega}$, average of vorticity.....97

Nomenclature

Lower case

a	amplitude
f_d	dominate frequency
g	gravity acceleration
k	wave number
u_{*a}	airside friction velocity
u_*	friction velocity
u_i	instantaneous streamwise velocity
$\tilde{u}$	wave streamwise velocity
u'	turbulent streamwise velocity
w_i	instantaneous vertical velocity
$\tilde{w}$	wave vertical velocity
w'	turbulent vertical velocity
z	vertical distance from water surface
z_{oa}	airside roughness length
z_o	roughness length

Upper case

D	average digital gray scale
E^2	variance of error associated with velocity
E_u	errors associated with the streamwise velocity
E_w	errors associated with the vertical velocity
E_v	errors associated with the resultant velocity
F_t	threshold for the fraction of the ROI occupied by the wake
F_w	fraction of the ROI occupied by the wake
H_{rms}	root mean square wave height
H_s	significant wave height
N_C	number of capillary waves
N_{CM}	number of breaking waves detected commonly by IR and DPIV
$N_{c\text{-}g}$	number of capillary waves per gravity wave
N_{DPIV}	number of breaking waves detected from DPIV vorticity fields
N_{IR}	number of breaking waves detected from IR images
N_{GC}	number of gravity waves with capillary waves
RH	relative humidity
P_{bw}	percentage of microscale breaking waves
T	temperature
T_{air}	average air temperature
T_{water}	average water temperature
U	mean streamwise velocity
U_a	average wind velocity
U_s	surface velocity

U_∞	wind velocity
V	resultant velocity
W	in-plane vertical displacement

Lower case Greek

ε	energy dissipation
κ	von karman constant
λ_d	dominant wave length
μ	water dynamic viscosity
ν	water kinematic viscosity
ζ	vertical position from water surface
ρ_a	air density
ρ	water density
σ_T	standard deviation of the image temperature
σ_w	standard deviation of the vertical displacement
τ_a	wind stress
τ_{total}	total shear stress
τ_{visc}	viscous stress
τ_{wave}	wave stress
ω	angular frequency
$\overline{\omega}$	average of vorticity

Upper case Greek

Φ_u	wavenumber spectrum of streamwise velocity

CHAPTER 1

Introduction

As the wind blows over the ocean surface, it generates surface waves of different wavelengths and amplitudes (from a few mm's to 100's of meters). At moderate wind speeds (i.e. 4 to 11 m s^{-1}), the occurrence of short gravity wind waves (wavelength less than 1 m) is wide spread. It has been speculated that many of these short gravity waves are microscale breaking waves; these are short gravity waves that break without entraining air. Researchers have suggested that because of their wide spread occurrence, microscale breaking waves could play a significant role in the air-sea gas and heat transfer (Banner and Peregrine 1993; Melville 1996). Therefore, improved understanding of the flow characteristics beneath breaking waves will lead to better understanding of air-sea heat and gas exchange. Due to the complexity of the turbulent flow in this region and limitations of measurement techniques, the investigation of the near surface flow beneath wind waves in general and microscale breaking waves in particular, is very challenging.

Most of the laboratory studies beneath short gravity wind waves and microscale breaking waves have been conducted for clean water surfaces (e.g. Wu 1975, Cheung and Street 1988; Thais and Magnaudet 1996; Siddiqui et al. 2001; Peirson and Banner 2003). In natural water bodies like oceans and lakes, however, biological organisms and other chemical species may affect the surface tension at the air-water interface. This alters of the air-sea boundary conditions and thus, the air-water gas and heat transfer rates. Zappa

et al. (2001, 2004) investigated the influence of microscale breaking waves on air-water gas and heat transfer rates for clean and contaminated surfaces using infrared imagery. They found that gas and heat transfer velocities were reduced beneath surfactant-contaminated surfaces.

Siddiqui et al. (2001) conducted a laboratory investigation of the near-surface region beneath microscale breaking waves. They observed strong near-surface vortices or coherent structures generated beneath breaking waves and a strong correlation between the near-surface vorticity and air-water heat transfer velocity. They argued that the strong coherent structures generated by microscale breaking waves are responsible for the enhancement of air-water heat transfer velocity. Siddiqui et al. (2004) investigated the influence of near surface coherent structures on the air-water gas transfer rate and found that these structures enhance the air-water gas transfer rate by a factor of more than two. However, these experiments included only clean surface. Detailed characteristics of the flow beneath surfactant-contaminated surfaces in the presence of wind waves are not well reported. As a result, the impact of surface contamination on the hydrodynamics of wind waves in general and in particular beneath microscale breaking waves is poorly understood.

Zappa (1999) observed parasitic capillary waves on the forward face of short gravity waves just prior to breaking. In addition, he observed that these capillary waves disappeared during the breaking process. Duncan (2001) also observed capillary waves on the forward face of mechanically generated gently spilling breaking waves. However, these studies did not include any detailed analysis of these capillary waves. In addition,

the relationship between the occurrence of parasitic capillary waves and the initiation of the breaking process is not well established.

The research presented in this thesis was motivated by the fact that in order to understand the impact of microscale breaking waves in natural water bodies, the influence of surface contamination on the near-surface flow must be explored. The research is also motivated by the fact that knowledge about the relationship between parasitic capillary waves and microscale breaking waves is very important in order to understand the wave breaking process.

1.1 Parasitic Capillary Waves

Water waves are typically classified as capillary waves, capillary-gravity waves and gravity waves. Capillary waves are very small waves whose wavelength is typically less than 5 mm (Kundu and Cohen 2002). These are waves in which the effect of surface tension is important, and gravity does not play any significant role. The capillary-gravity waves are waves for which both the surface tension and gravity are important. Their typical wavelength ranges from 10 mm to 7 cm. As its name implies, gravity effects are important for gravity waves and the effect of surface tension is negligible. These are the waves whose wavelength is greater than 7 cm.

On the downwind face of short gravity waves (wavelengths 7-50 cm) a train of short capillary waves is often observed (Longuet Higgins 1963). These capillary are called " parasitic capillaries", see figure 1.1. Scott Russell (1844) reported the first observations of capillary waves, and the first experimental study of these waves was

conducted by Cox (1958). The dynamical theory of the generation of parasitic capillaries has been developed by Longuet Higgins (1963), Crapper (1970), Philips (1981).

Longuet Higgins (1963) argued that when a progressive gravity wave approaches its maximum steepness (i.e. incipient breaking), a sharp crest is formed with localized surface tension, not distributed over the whole wave. This localized surface tension produces a train of capillary waves ahead of crest. After formation, these capillaries waves extract energy from the gravity wave and at the same time lose their energy via viscous effects. He argued that the energy transfer from the gravity wave to these capillaries causes a significant damping of the gravity wave, which may exceed the damping of the gravity wave by the viscous effects alone.

Philips (1981) predicted that parasitic capillary waves are relatively prominent on the downwind faces of the dominant wave crests, as a consequence of long and short wave interactions. He explained the phenomena in a frame of reference moving with the phase velocity of the long wave. In this frame of reference, due to the relatively small phase velocity, the downwind train of capillary waves propagates towards the long wave. When the capillary wave train reaches a long wave crest, it gets blocked and cannot pass the long wave crest. As a result, this train of capillary waves can only be observed on the downwind faces of gravity wave crests.

Okuda (1982) and Ebuci, Kawamura & Toba (1987) observed a region of strong vorticity, or roller, at the crest of gravity waves in the presence of parasitic capillary waves, as highlighted in (figure 1.1, top). They argued that the high vorticity region beneath the crest is related to the large tangential wind stress on the windward face of the crest. Longut Higgins (1992) theoretically showed that the parasitic capillary waves are

the source of strong vorticity in the crest of the gravity waves. He argued that in a steady flow, any curved free surface, rotational or irrotational, is a source of vorticity. Because of the high radian frequency of the capillary wave, the vorticity they generate is much larger in magnitude than that generated by the gravity wave itself. Thus, he concluded that the capillary waves are a strong source of vorticity, capable of producing a 'roller', or closed circulation in the crest of short gravity waves.

Duncan et al. (1999) investigated the surface profile histories of gently spilling mechanically generated breakers. They also observed capillary waves upstream of the leading edge of the high vorticity region. They found that the toe or the leading edge is at first fairly stationary, but during the breaking process, it moves down the forward face of the wave and then ripples are generated between the toe and the crest, which eventually are left behind the wave crest.

1.2 Microscale Breaking Waves

Wave breaking occurs when the velocity of water particles near a wave crest exceeds the phase speed and the water overtakes the waveform. As a result, a portion of the fluid near the wave crest becomes turbulent and leaves behind a decaying turbulent wake (Banner and Peregine, 1993). Breaking waves enhance the gas and heat transfer at the air-sea interface, dissipate wave energy and generate ocean current by momentum transfer from the wave field (Melville 1996). Breaking waves occur over a wide range of length scales and intensities. Large-scale breaking waves are the most intense and visible type because they entrain a large amount of air and produce white caps. Banner and Phillips (1974) introduced a term "micro breaking", also called microscale breaking,

which describes the breaking of very short gravity waves in which surface tension is strong enough to prevent air entrainment. Microscale wave breaking occurs at low to moderate wind speeds (i.e. 4 to 12 ms^{-1}). They are a few centimeters in amplitude and *O* (0.1-1) m in length with a bore-like crest directly preceded by parasitic capillary waves riding along forward face (Jessup et al. 1997a), as shown in figure 1.1.

A wave-breaking event is comprised of many complex processes like non-linear deformation of the laminar flow, generation of vorticity at the water surface, and rapid production of turbulence (Duncan 2001). The physical mechanism(s) that cause microscale wave breaking are not well understood. Duncan (1994) made high-speed observations of mechanically generated spilling breakers that showed the breaking was initiated when a bulge formed (see figure 1.2), on the forward face of a wave, which was in accordance with a theoretical prediction by Longuet Higgins et al (1994). Zappa (1999) observed capillary waves on the steep forward face of wind waves before the beginning of microscale breaking process. This is consistent with Duncan's (1994, 1999) observation of surface profile histories of mechanically generated spilling breaking waves. Duncan (2001) argued that for long wavelengths, the spilling process begins with a small jet that produces a small turbulent patch above the mean water level; however, for short waves, the jet is influenced by the surface tension and replaced by a surface tension dominated bulge with capillary waves upstream of its leading edge (toe), see figure 1.2.

Due the absence of air entrainment, microscale breaking waves are difficult to identify using conventional methods. Jessup et al (1997 a) presented a method to detect and quantify microscale breaking waves sensing infrared imagery. This technique is based on the fact that under most circumstances there is a cool skin layer at the water

surface (due to evaporation), where the temperature is a few tenths of a degree Celsius lower than the bulk water temperature immediately below. Breaking waves disrupt this cool skin layer and bring the warmer water to the surface, creating a warm thermal wake. As the wake dissipates, the cool skin layer reestablishes (Jessup et al 1997b). The conceptual model of this process is presented in figure 1.3. The thickness of the skin layer is the order of 10^{-3} m (Wu 1971). An IR imager measures the temperature variations only in the skin layer because the optical depth of the infrared radiation detected by the imager is about 10^{-5} m. Therefore, the IR imager can record the temperature variations at the water surface due to the disruption and recovery of the skin layer. An infrared image of the water surface at a wind speed of 8.1 m s^{-1} is shown in figure 1.4. The warm patch in the image is the thermal wake created due to the disruption of the cool skin layer by a microscale breaking wave. The cool temperature in the surrounding region shows the undisturbed skin layer. Thus, by detecting these thermal wakes, microscale breaking waves can be identified and quantified. Jessup et al. (1997a) used the fraction of the total surface area occupied by the thermal wakes (A_B) to quantify the influence of microscale breaking waves.

Zappa (1999) and Zappa et al (2001, 2004) investigated the influence of microscale breaking waves on air-water gas and heat transfer rates using simultaneous infrared and wave-slope imagery. They also used the controlled flux technique to estimate the local air-water heat transfer velocity. They found that A_B was correlated with the heat and gas transfer velocities across the air-water interface, and argued that microscale breaking waves enhanced the air-water transport. Zappa (1999) found that the disruption of the skin layer occurred coincidentally with waves that had a steep forward

face and dimpled bore like crest. He also observed trains of parasitic capillary waves on the forward faces of the wind waves prior to the breaking, which disappeared as the wave broke.

Siddiqui et al (2001) conducted a laboratory investigation of the flow beneath microscale breaking waves using simultaneous infrared imagery and particle image velocimetry (PIV). They showed that the thermal wakes in the IR images are typically produced by a series of strong vortices or coherent structures that are formed behind the leading edge of the microscale breaker. These vortices are first very strong and coherent, but as the time passes they move from the crest region to the back face of the wave and become weaker and less coherent. They also found a strong correlation between the air-water heat transfer velocity and the near surface vorticity, and argued that the strong near-surface vortices are responsible for the enhancement of the air-water heat flux.

In order to investigate the influence of the near-surface coherent structures, Siddiqui et al. (2004) computed the properties of these structures and developed a new parameterization of the air-water gas transfer velocity that utilized the coherent structure properties. They found that these coherent structures enhance the air-water gas transfer velocity by a factor of 2.8 and are responsible for the transport of 60% of the total air-water gas flux. Their results also showed that in the regions occupied by coherent structures, the rate of turbulent kinetic energy was enhanced by a factor of 2.5.

Siddiqui and Loewen (2004) reported a technique for detecting microscale based on the variance of vorticity in the crest region. Their results show that the percentage of microscale breaking waves increased with wind speed from 11% at 4.5 m s^{-1} to 90% at 11 m s^{-1}. They compared the geometric and flow properties of microscale breaking and non-

breaking waves and found that microscale breaking waves are on average, steeper, larger in amplitude and have higher rate of turbulent kinetic energy dissipation. They also observed a significant overlap between the probability distribution functions of wave slope and amplitude for breaking and non-breaking waves, and argued that a microscale breaking wave detection scheme base on the wave slope and amplitude would be unreliable.

Peirson and Banner (2003) investigated the flow under the microscale breaking waves using the digital particle image (DPIV) measurement. They detected the microscale breaking waves using a scheme based on the local wave slope threshold on the leeward face of the wave. They observed high values of vorticity and surface convergence at the leading edge (or toe) of the breaking wave and argued that it is the subduction of the flow at the toe that is responsible for the majority of the gas transfer.

1.3 Turbulent Flow Beneath Wind Waves

When wind blows over the water surface, surface waves, mean shear, and turbulence are generated in the water. The precise mechanism of momentum and energy transferring from air to water, and the complicated interactions among the mean, wave, and turbulent velocity fields in the waterside are not fully understood. Many researchers have attempted to decompose the instantaneous velocity field beneath wind waves in order to understand their interactions.

Benilov and Filyushkin (1970) proposed that when simultaneous measurements of the surface displacement and velocity are available, the wave motion can be isolated in the frequency domain by using a linear filter assuming that the wave-induced motions are

linearly related to the water surface elevation and are not correlated with turbulent velocities. Lumley and Terray (1983) analyzed field measurements of the velocity beneath wind waves using this technique. They observed a peak at the dominant wave frequency spectra by filtering the wave motions from the total velocity signals. Their frequency spectra of the turbulent velocity had an $f^{-5/3}$ dependence in a region far from the dominant frequency.

Wu (1975) made systematic measurements of the current below wind waves at different wind speeds. He measured the drift current immediate below the water surface by timing floats as they passed two stations 1.5 m upwind and downwind from the test section, and using a pitot-static tube for velocity measurement in the subsurface current. The velocity of floats was interpreted as the drift current. He found that the current close to the surface varies linearly with depth, and estimated the surface drift current by extrapolating the linear velocity curve to the surface. He computed the waterside friction velocities from logarithmic profiles of the current, and airside friction velocities from logarithmic profiles of the wind velocity. He observed that the airside and waterside friction velocities increased with wind velocity.

Cheung and Street (1988) made velocity measurements at a fetch of 13 m and wind speeds ranging from 1.5 to 13.1 m s^{-1} using a two-component Laser-Doppler-Anemometer (LDA). However, their measurements were restricted to the regions below the wave troughs. They separated the wave and turbulent velocities using a linear filtration technique. They observed logarithmic mean streamwise velocity profiles. Their analysis of the wave and turbulent velocities indicated that energy is transferred from the wave to the mean flow and turbulence. They also observed that the mean wave induced

shear stress was not zero, which indicates that the flow was not irrotational. Moreover, they observed logarithmic mean streamwise velocity profiles. They computed the waterside friction velocity by extrapolating the turbulent shear stress (measured below the wave troughs) to the interface using a linear fit.

Jiang et al (1990) applied a nonlinear stream function to the data of Cheung and street (1988) and separated the wave and turbulent energy velocity components. They assumed an incompressible flow with irrotational and periodic wave motion in order to separate the wave and turbulence velocities. They observed peaks at high and low frequencies in the coherence spectra between the wave and turbulent velocities and concluded that this was an indication of wave-turbulence interactions. They argued that the peak at low frequencies indicated the interaction between relatively long-slow turbulent fluctuations and wave motions; however, the other peak at high frequencies may arise from the interaction between short-rapid turbulent fluctuations and wave motions. Time-averaged correlations between the wave and turbulent velocity components increased with wind speed and decreased with depth. They also found low coherence values between the stream wise and vertical components of the turbulent velocity beneath the wave troughs and argued that the wave and turbulent components were separated correctly. However, at the same depth, the frequency spectra of the streamwise and vertical turbulence velocity components had a prominent peak at the dominant wave frequency, which indicates leakage of the wave velocity into the turbulent velocity component.

Thais and Magnaudet (1996) conducted velocity measurements with a two-component Laser-Doppler-Velocimetery (LDV) for wind speeds ranging from 4.5 to

7.8 m s^{-1} at a fetch of 26 m. They separated the wave induced and turbulent velocities using a nonlinear triple decomposition technique. In contrast with the observations of Cheung and Street (1988), they observed positive wave induced shear stresses that showed that the waves extract energy from the mean flow field. They observed a slope of –3 in the frequency spectra of the turbulent velocity at frequencies greater than the dominant wave frequency and concluded that this was an indication of wave-turbulence interaction. They found that the turbulent kinetic energy balance was dominated by energy dissipation and turbulent transport below the troughs, and suggested that the majority of energy production takes place above the wave troughs. They computed the airside friction velocity from the measured wind velocity profile and estimated the waterside friction velocity by assuming that the entire momentum flux from the wind goes into the wind drift layer in the water (i.e. $\rho_w u_{*w}^2 = \rho_a u_{*a}^2$).

Banner and Peirson (1998) made a detailed investigation of wind driven aqueous viscous sublayer (i.e. within 1 mm from the interface) using Particle Image Velocimetry (PIV). They found that before the development of waves, the entire wind stress is transferred to the tangential stress, but as soon as a wave field is developed, the major portion of the wind stress is transferred to the waveform drag, which was estimated as the difference between the observed wind stress and the mean waterside tangential stress.

Siddiqui and Loewen (2004) investigated the structure of flow in the wind drift layer at different wind speeds using Digital Particle Image Velocimetry. Their results show that in the wind drift layer, the mean streamwise velocity profiles were logarithmic. They also estimated the rate of turbulent kinetic energy dissipation in this layer, and found that at a depth of 1 mm from the surface, the rate of turbulent kinetic energy

dissipation was approximately a factor of four larger than the values at depths greater than 15 mm. They also decomposed the wave and turbulent velocity fields by using a spatial filter and found that due to the large difference in the magnitudes of wave and turbulent velocities, leakage of a very small fraction of the wave velocity into the turbulent component could significantly alter the magnitude of the turbulent kinetic energy.

1.4 Surfactant

Surfactants or surface-active agents are described as molecular species that are liked to locate at the surface of a liquid (Jones and Toba 2001). They are comprised of hydrophobic (water-fearing) part and a hydrophilic (water-loving) part, so they seek an equilibrium state at an interface between aqueous and non-aqueous phases (e.g., the air-sea interface), as shown in figure 1.5.

The surface tension, or free surface energy can be described by the molecular attraction forces in a liquid. In the bulk fluid, each individual molecule is surrounded by the neighboring molecules of the same kind, and the molecule experiences uniform attractive forces in all directions. However, the molecules at the interface tend to be pulled inward because there are no liquid molecules above the interface that can balance the attraction forces exerted by the molecules underneath. Consequently, the area of the surface decreases and the fluid contracts until the smallest possible surface area for the given fluid volume is reached. Therefore, a finite amount of work proportional to the surface area is required to bring the molecules from the bulk to the surface against this

inward attraction. This work is denoted as the surface tension (σ) and expressed in terms of the energy per unit area or force per unit length (Mc Kennna 2000).

When a surface-active film is present at the free surface, it will tend to lower the surface free energy, thus lowering the surface tension. Spatial variations in concentration of surfactant produce surface tension gradients, which can drive surface flows as well as the near surface bulk flow underneath. Marangoni in1871 first discovered this effect, and those forces are named Marangoni forces. Marangoni forces affect the free-surface tangential boundary condition, which is crucial for capillary wave dynamics. At a smooth surface without surface tension gradients and ignoring the airside effects, the tangential stress boundary condition is given as:

$$\mu \frac{\partial u}{\partial y} = 0$$

That is, the fluid surface is stress-free. However, in the presence of surface tension gradient due to spatial variations in the surfactant concentration, the boundary condition changes to:

$$\mu \frac{\partial u}{\partial y} = \frac{\partial \sigma}{\partial x}$$

That is, the viscous stress at the interface is equal to the surface tension gradient. The presence of a non-zero viscous stress at the interface causes a dissipative viscous boundary layer resulting in the flow damping (Mc Kennna 2000).

The waves are damped by viscous effects below the surface. Lucassen-Renders et al (1969) showed that for single wavelength capillary waves, the damping is brought about by changes in the tangential stress boundary condition at the surface, which is balanced by any surface tension gradient that they evoke. They argued that in the absence

of a surfactant, no such gradients could be produced and therefore the water surface is allowed to expand at the rear of the wave and to be compressed at its front, which enables the liquid below the surface to conform to a so called potential flow in which very little energy is dissipated by viscous friction. However, the surface compression and expansion, which accompanies a wave, will change the spatial concentration of the surface-active material at the surface. Consequently, the liquid below the surface is forced into a flow pattern in which the velocity gradient or viscous friction is increased, and as a result the wave damping is enhanced.

Lucassen (1982) calculated that the damping coefficient of gravity waves can be considerably increased in the presence of surface-active material. He concluded that the potential effect of the surface-active material on the wave damping should increase with an increase in the wavelength. Cini and Lombardini (1981) conducted experiment to investigate the wave damping in the intermediate regime between capillary and gravity waves for a Triton X-100 solution. Their experimental results were in agreement with the theoretical predictions of Lucassen (1982).

Mitsuyasu and Honda (1982) observed that the wind profile and air friction velocity changed drastically in the presence of surfactant, especially for wind speeds higher than 7 m s^{-1}. They argued that this trend is due to the changes in the water surface roughness because of wave suppression by the surfactant. Mitsuyasu and Honda (1986) conducted a laboratory wind-wave experiment at a wind speed of 7.5 m s^{-1} and at a fetch of 6 m. They found that the spectral energy of the wind waves changes significantly with the change in the surfactant concentration.

Bock et al. (1999) conducted laboratory studies in circular wind wave flume to investigate the relationship between air-sea gas transfer velocities over clean and surfactant contaminated water surfaces. Detailed surface wave measurements were made using a scanning laser slope gauge. They found that the wind friction velocity and the air-water gas transfer velocity both decreased as much as 60% in the presence of surface films. They also observed that in the present of a surfactant, the short waves (above 200-300 rad/s) were completely eliminated, and concluded that the short wind waves play an important role in air-sea gas exchange.

Zappa (1999) conducted simultaneous and collocated measurements of laboratory wind waves using IR and wave slope imagery, to investigate the effect of microscale breaking waves on air-water gas transfer for clean and surfactant contaminated water surfaces. He found that the gas transfer velocity was lower in the presence of a surfactant at a given wind speed, and that capillary waves were damped by the surfactant. He also observed that the fractional area covered by the thermal wakes of microscale breaking waves (A_B) was correlated with the gas transfer velocity, and that correlation was insensitive to the presence of a surfactant. He argued that microscale wave breaking controls the rate of air-water gas transfer and that the capillary waves facilitate the microscale breaking process and contribute significantly to the wave slope.

Ceniceros (2003) numerically investigated the effects of surfactant on the formation and evolution of small capillary ripples on the forward face of short waves. He used a hybrid numerical methodology to couple the full two-fluid Navier-Stokes equations with free boundary motion and with the surfactant dynamics. He found that the

capillaries were dramatically affected by the surfactant, and the size of the wave roller, amplitude and the wavelength decreased as the surface tension gradient increased.

1.5 Objectives

As the preceding literature review demonstrates, surfactants have a significant impact on the hydrodynamics of near-surface flows. However, the impact of surfactants on the flow structure beneath wind-driven air-water interfaces is still not well understood. Moreover, the characteristics of parasitic capillary waves riding along the forward face of a gravity wave and their relation to the wave breaking process has not been explored in detail.

The main objectives of this study are,

- To investigate the impact of surface contamination on the characteristics of the flow in the near surface region beneath short gravity wind waves at moderate wind speeds.
- To investigate the characteristics of parasitic capillary waves beneath clean and contaminated surfaces.
- To investigate the relationship between capillary waves and microscale breaking waves in order to improve our understanding about the microscale wave breaking process.

In order to accomplish these tasks, a series of experiments were conducted in a wind-wave flume at the Harris Hydraulics Laboratory (University of Washington, Seattle). These experiments were conducted by Professor Loewen's research group that included Dr. M.H.K. Siddiqui, M. Atmane, and M. Elkamash. Non-invasive

measurements were made at wind speeds of 6.3 and 8.1 m/s, and at a fetch of 5.5 m. Measurements were gathered beneath clean and surfactant contaminated water surfaces. The skin-layer or water surface temperature was measured using an infrared (IR) imager and digital particle image velocimetry (DPIV) was used to obtain simultaneously sampled high-resolution measurements of the two-dimensional velocities immediately below the water surface. My contribution to this research is the processing and analysis of these experimental datasets.

A complete description of the experimental setup and the data processing techniques is presented in Chapter 2. In Chapter 3, the flow characteristics within the wind drift layer beneath short gravity waves are presented and discussed. In chapter 4, the detailed characteristics of parasitic capillary waves are presented and a scheme to detect microscale breaking is described. The relation between the occurrence of parasitic capillary waves and microscale breaking waves are also discussed in this chapter. Finally, in Chapter 5 the main result are summarized and some suggestions are presented for the future work in this field.

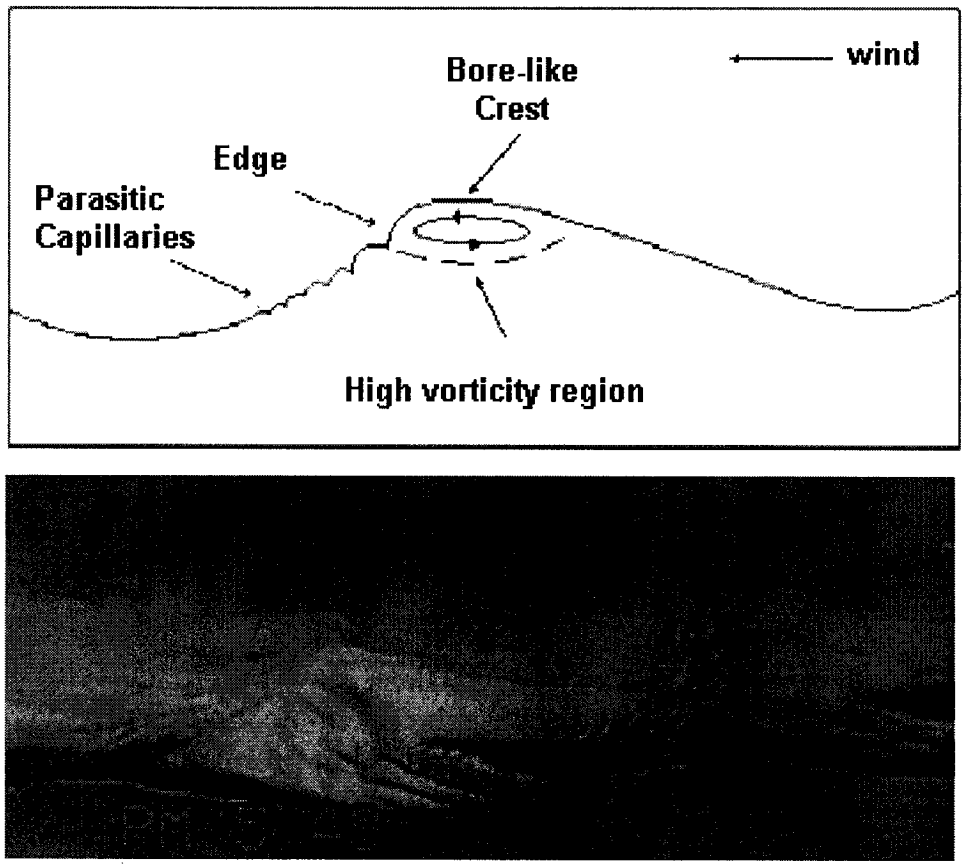

Figure 1.1: (Top) A conceptual sketch of a microscale breaking wave. The characteristic feature of a microscale breaking wave is a bore-like crest preceded by capillary waves riding along the forward face. (Below) A digital video image of a microscale breaking wave with a wavelength of approximately 10 cm (Jessup 1997a).

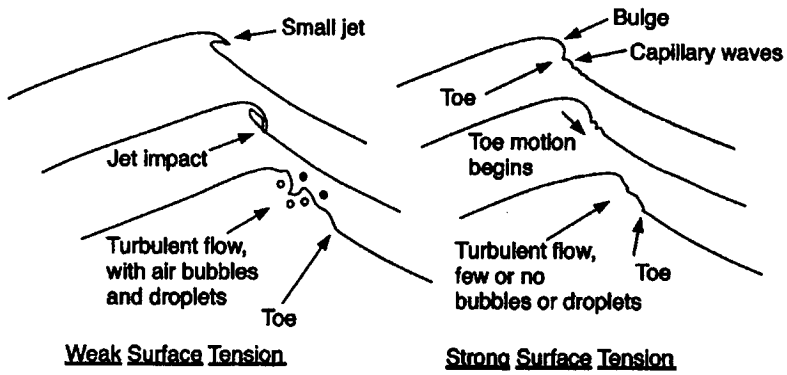

Figure 1.2: A schematic showing the three phases of gentle mechanically generated breaking waves for weak and strong surface tension effects (Duncan 2001).

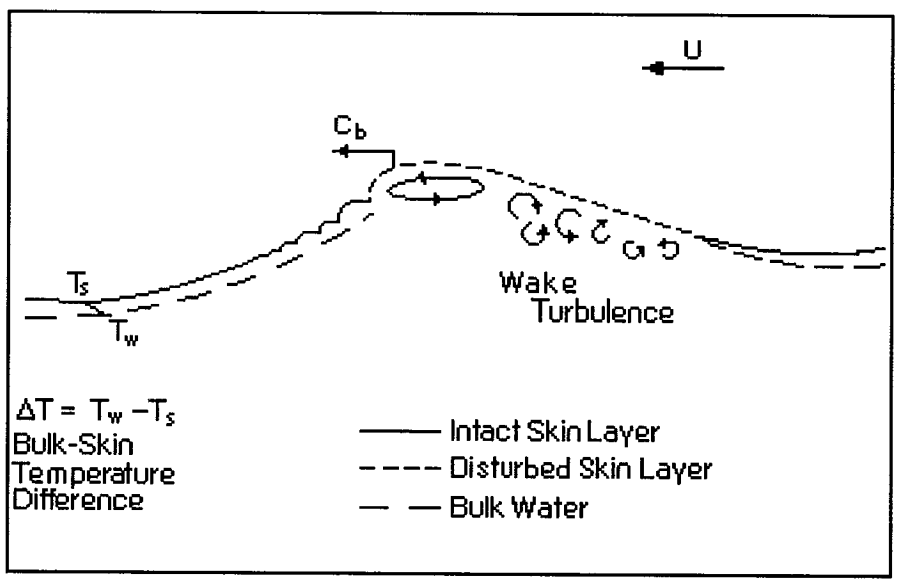

Figure 1.3: Disruption and recovery of the skin layer due to wave breaking (Jessup 1997a).

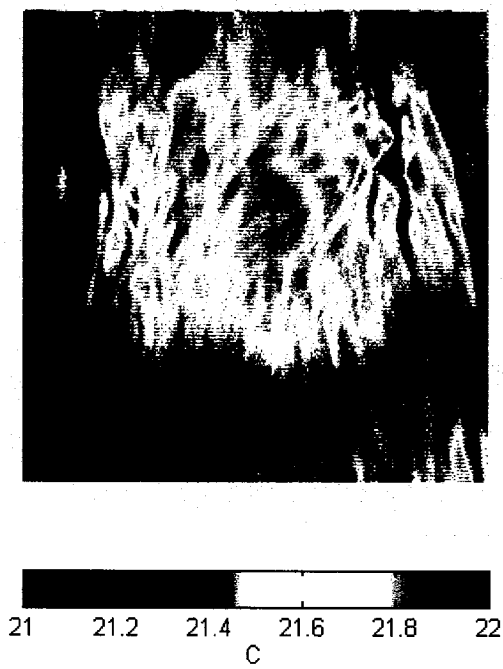

Figure 1.4: A thermal wake created due to the disruption of the cool skin layer by a microscale breaking wave in an IR image at 8.1 m s^{-1} wind speed. The image is 14.1 by 14.1 cm in size.

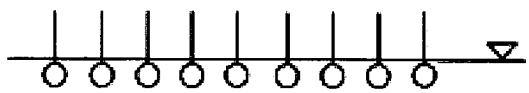

Figure 1.5: A typical surfactant film orientation at the air-water interface; O, the hydrophilic head; _____, the hydrophobic head.

CHAPTER 2

Experimental Setup and Methods

2.1 Experimental Setup and Instrumentation

The experiments were conducted in a wind-wave flume at Harris Hydraulics laboratory, University of Washington, Seattle. The flume is 9.2 m long and 1.18 m wide and a water depth of 87 cm. A centrifugal fan located upstream of the flume was used to blow the air over the water surface. At the down-wind end of the flume, a horsehair beach was used to absorb the wave energy. A schematic of the experimental setup is shown in figure 2.1. Measurements were conducted at a fetch of 5.5 m at wind speeds of 6.3 and 8.1 m s^{-1}. At each wind speed, the experiments were conducted for clean and surfactant-contaminated water surfaces. For the surfactant-contaminated runs, 1 p.p.m. of Triton X-100 was added to the tank. The experiments were conducted under neutral conditions, i.e. approximately the same bulk air and water temperatures were maintained during the experimental runs to minimize the sensible heat transfer across the air-water interface. The detailed environmental conditions during the experiments are presented in table 2.1.

Two-dimensional velocity fields beneath the wind waves, in a plane parallel to the wind and bisecting the water surface were measured using Digital Particle Image Velocimetry (DPIV). Silver-coated glass spheres with a mean diameter of 15 μm and specific gravity of 1.65 (potters Industries, Paoli, PA) were used as the tracer particles.

For flow measurements in water, if the specific gravity of the tracer particle is not equal to unity then the particles are not exactly neutrally buoyant. The accuracy with which they follow the flow depends on the response time of the particle. Siddiqui (2002) has shown that the response time of these particles is significantly smaller than the Kolomogorov timescale under similar conditions, and concluded that these particles follow the flow accurately. A 25 mJ Nd:YAG laser (Minilite-II, Continuum Electro-Optics, Santa Clara, CA) was used as the light source to generate a lightsheet. The laser optics were arranged beneath the tank to generate a 3 mm thick lightsheet and to obtain a lightsheet width of 10 cm at the water surface (see figure 2.1). A delay generator (BNC 500A, Berkeley Nucleonics, San Rafael, CA) was used to control the timing of the laser pulses. The first pulse was generated close to the end of the first camera frame and the second pulse was generated right after the beginning of the second camera frame. The separation time between the two pulses was set equal to 4.4 ms and 2.7 ms for the experimental runs at 6.3 and 8.1 m s^{-1} wind speeds, respectively.

A progressive-scanning full frame shutter 10-bit CCD camera (1040E Pulnix, Sunnyvale, CA) with a resolution of 1008 × 1008 pixels was used to image the flow field. The field of view of the camera was set equal to 3.5 cm × 3.5 cm. This camera, which is here after referred to as the DPIV camera, imaged the flow field from outside the tank, at an angle of 8^{o} from the horizontal (see figure 2.1). The camera was connected to a personal computer equipped with a frame grabber (Road Runner, Bitflow, Woburn MA). The camera acquired 8-bit images at a rate of 30 Hz, for each experimental run of 5 minutes duration (i.e. 9000 images at each run). At each wind speed, two experimental runs were conducted for each of the clean and surfactant-contaminated cases.

An infrared (IR) imager (Radiance HS Raytheon TI systems, Dallas, TX) with a resolution of 256 × 256 pixels was used to measure the water surface temperature. The imager was sensitive to thermal radiations in the 3-5 μm wavelength band and has 12-bit pixel depth. The IR imager was located on the top of the tank looking down at an angle of 22^{o} with respect to vertical, with the field of view of 14.1 cm × 14.1 cm (see figure 2.1). The imager was connected to a PC equipped with a frame grabber (Road Runner, Bitflow, Woburn, MA). For each experimental run, 12-bit IR images were acquired at a rate of 120 Hz.

The water surface was within the field of view of the DPIV camera. Since the water surface was fluctuating continuously due to the wave motion, it often acted like a mirror for the DPIV camera, which was imaging the flow from underneath. Thus, in many DPIV images, the reflection of tracer particles appeared above the water surface, making it very difficult to accurately locate the position of the air-water interface. Accurate detection of the water surface is required in order to obtain accurate estimates of the near-surface velocities. Siddiqui *et al.* (2001) developed a technique to accurately locate the fluctuating water surface in the DPIV images and to obtain accurate estimates of the near-surface velocities. They used another camera to image the water surface exactly above the DPIV field of view. Looking from above, it is the location where the laser lightsheet intersects the water surface. They used the surface profile obtained from these images to locate the water surface in the DPIV images. Following to their technique, in this research another CCD camera (TM-9701, Pulnix, Sunnyvale, CA) with a resolution of 768 × 484 pixels was used to image the water surface where it was intersected by the laser lightsheet. This camera, which is referred to as the profile

camera, was mounted above the DPIV camera, looking down at an angle of 18° from the horizontal (see figure 2.1). This camera was connected to a PC equipped with a frame grabber (Road Runner), and acquired profile images with a pixel depth of 8-bit, at a rate of 30 Hz.

2.2 Synchronization and Collocation of the DPIV, Profile and IR Cameras

For the simultaneous sampling of images, the DPIV, profile and IR cameras were synchronized. The composite analog video signal from the profile camera was used as the master signal. The vertical sync signal was stripped from the composite analog video signal of the profile camera was used to synchronize the DPIV and the IR cameras, and the laser. The flow diagram of the synchronization network is shown in figure 2.2. Sync stripper *A* was used to strip the 30 Hz vertical sync signal from the composite video signal of the profile camera. One output of this signal was supplied to the DPIV camera to synchronize it with the profile camera. This same 30 Hz sync signal was supplied to a function generator and then a pulse generator to obtain a vertical sync signal at 120 Hz. This 120 Hz signal was provided to the IR image. The synchronization of the cameras was tested before the start of the experimental runs.

Two lasers are used in the DPIV technique to generate the laser pulse alternately. Each laser requires a sync signal at 15 Hz. The composite video signal of the DPIV camera was used to synchronize both lasers. The vertical sync signal from this composite video signal was generated using sync stripper *B*. This 15 Hz signal was then provided to a pulse generator, which generated four output signals T_1, T_2, T_3, and T_4. The signals T_1

and T_2 are for the first laser and signals T_3 and T_4 are for the second laser. The time separation between the two DPIV images is equal to $T_4 - T_2$. An external signal was used to start the image acquisition by the IR, DPIV and profile cameras, and the acquisition of the environmental data. This triggering sequence is shown in figure 2.3.

A small rigid block with vertical shafts and a ruler mounted on it (as shown in figure 2.4) was used to collocate the fields of view of the DPIV, profile, and IR cameras. The block was placed in the fields of view of all three cameras, and the images of this block were then acquired by all cameras. The collocation images acquired by the three cameras are shown in figure 2.4 (b,c and d). The images of the block were then used to convert the cell dimensions of each camera into actual distance and for the collocation of the fields of view of all cameras. The uncertainty in placing the fields of view of the DPIV and profile cameras in the IR images is within ± 1.5 mm.

2.3 Environmental Measurements

Wind speed, bulk air and water temperature, and relative humidity were measured during each experimental run. The air and water temperature data were sampled at a rate of 100 Hz per channel using an eight channels A/D board. Wind speed was measured using an air velocity transducer (OMEGA FMA-905-V) that was placed 23 cm above the mean water level. The average values of the bulk air relative humidity, the bulk air and water temperatures, and the wind speed are presented in table 2.1.

2.4 Surface Temperature Measurements

Surface temperature values were obtained by converting the digital gray-scale values of the IR images into degree Celsius. For this purpose, the IR imager was

calibrated using a black body (Model 2004S, Santa Barbara Infrared, Santa Barbara, CA) accurate to 0.01 °C with a stability of ±0.003 °C. For the calibration, the IR imager was placed 2 mm away from the black body. The black body was set at 22 and 27°C, and at each temperature a sequence of 30 images was captured. The average gray-scale value of each sequence was computed and plotted against the respective temperature of the black body. The calibration equation was obtained from a linear fit to the data points and is given below,

$$T = 22 + \frac{(27-22)\times(D-910)}{2913-910} \tag{2.1}$$

where T is the temperature in °C and D is the average digital gray-scale value of the image sequence. Using the above equation, the digital gray-scale values of the IR images were converted into the temperature units.

2.5 Wave Profile Measurements

The surface wave profile was computed in each profile image. Due to the presence of the tracer particles on the waterside, the reflectivity of the light sheet on the waterside was higher than the airside. As a result, in the profile images, the gray-scale values on the waterside were much higher than the gray-scale values on the airside (see figure 2.5 a). This difference in gray-scale values was used to detect the water surface.

An algorithm was developed to detect water surface in the profile images. In this algorithm, the first step was to segment the gray-scale profile images. The threshold for the image segmentation was based on the histogram of the profile images. As mentioned

above, due to the difference in the gray-scale values, the pixels in the air and water regions of a profile image, appeared as two distinct peaks. The threshold was set equal to the gray-scale value at the depression in the middle of the two peaks. A sequence of morphological operations were performed on the segmented images to minimize the noise in the images and to remove small water droplets that appear above the water surface and corrupt the computed surface profile (Siddiqui 2002). The segmented image is shown in figure 2.5 (b). Finally, the surface profile is computed by detecting the edge at the air-water interface. The computed surface profile is plotted on top of the corresponding profile image in figure 2.5 (c). The figure shows that the algorithm accurately detected the air-water interface. The uncertainty in computing the surface profile in the profile images is within ± 0.3mm.

2.6 DPIV Technique

The DPIV technique measures velocity vectors in a flow field simultaneously at many (e.g. thousand) points in a plane. A typical DPIV system consists of a laser (that is used as a light source), optics to generate a light sheet, CCD camera, pulse generator to control timing of the laser pulses, and a PC equipped with a frame grabber for image acquisition. The flow under investigation is first seeded with the tracer particles, which follow the flow field. Then, a pulse of laser light illuminates a plane in the flow and the tracer particles within the light sheet reflect the light. The CCD camera records the position of these particles in an image. A short time later, the second pulse illuminates the same plane, and the camera captures the second image of particles, the bulk of which are now shifted in the direction of flow. These two images are considered as an image pair.

In this way, a series of the DPIV image pairs are obtained. To measure high flow velocities, the first laser pulse is set close the end of the first camera frame and the second laser pulse is set right after the beginning of the second frame, see figure 2.6.

Each of the image pairs obtained from the DPIV camera is then process to obtain the corresponding velocity field. The first and second images of an image pair are divided into small regions typically 32×32 pixels. These small areas are called interrogation and search areas in the first and second images, respectively (see figure 2.7a). The maximum cross correlation between the corresponding interrogation and search areas (see figure 2.7b) gives the average particle displacement within the interrogation region (see figure 2.7c). Then, the average velocity in this region is obtained by dividing the average displacement by the time interval between the two laser pulses. The interrogation region is typically set small enough, such that the velocity field is approximately uniform in this region. This process is repeated for all the interrogation areas to obtain velocities over the entire image.

In the interrogation windows where the interface appears, the reflected particles biased the magnitude as well as the direction of the velocity vectors. Thus, it is important that these false particles must be removed prior to the computation of the velocity field. Therefore, in the present study, a pre-processing step has been performed to minimize the uncertainty in the computation of the near surface velocities due to the reflection of particles above the air-water interface. We used a technique similar to one reported by Dabiri and Garib (1997). In this technique, the computed surface profile is first imported into the corresponding DPIV image to locate the air-water interface. As both the DPIV and profile cameras have different resolutions, the profile data was resized to match the

field of view of the DPIV camera. To correctly locate the interface in the DPIV images, the vertical offset between the fields of view of the two cameras must be considered. In many DPIV images, some part of the interface was clearly visible (see figure 2.8a). So, the vertical offset was determined when the surface profile from the profile images coincides with the visible part of the interface in the corresponding DPIV images. For each experimental run, 300 DPIV images with partially visible interface were selected. The surface profiles were then plotted over the corresponding DPIV images to obtain the optimum value of the vertical offset (see figure 2.8b). The total error in locating the water surface into the DPIV images was estimated to be within $\pm$ 0.6mm. Once the air-water interface is accurately locate in the DPIV images, the gray-scale values of all bright regions above the interface were set equal to the median gray-scale value of the image (i.e. the background value). Thus, the bright reflected particles above the interface were removed, as shown in figure 2.8 (c).

Once all DPIV images are preprocessed, the next step is to process these images to obtain the velocity field. In the processing step, the raw velocity fields were computed using a standard cross-correlation DPIV algorithm written by Marxen (1998). The size of the interrogation window in the first image was set equal to 48 $\times$ 48 pixels and the search window in the second image was set equal to 96 $\times$ 96 pixels. A 50% window overlap was used in order to increase the nominal resolution of the velocity field to 24 $\times$ 24 pixels, which gave a nominal spatial resolution of 0.8 mm $\times$ 0.8 mm. Once the velocity vectors were computed, the corresponding water surface profile data were used again to discard all velocity vectors located above the interface. A local median test developed by Siddiqui *et al.* (2001) was used to detect the spurious vectors and to replace them with the

median of the neighboring velocity vectors. Typically, less than 1% of the velocity vectors were spurious. The corrected velocity vectors were then interpolated onto a regular grid using an Adaptive Gaussian Window (AGW) interpolator (Agüí and Jiménez 1987).

It was noticed that in some velocity fields, the velocity vectors in the crest region were incorrect due to the high velocity gradients in this region, (see figure 2.11). These bad vectors were not detected and corrected by the median test. Therefore, another scheme was developed to detect these bad frames by applying a threshold based on the streamwise velocity gradients in the vertical direction (i.e. $\partial u/\partial y$). The magnitude of $\partial u/\partial y$ associated with these bad vectors was used to set the gradient threshold. In this technique, the velocity gradient threshold was applied to the instantaneous $\partial u/\partial y$ in the vertical direction at each horizontal location. If $\partial u/\partial y$ exceeds the threshold at more than n grid points in the vertical direction at any horizontal location, then the entire velocity field is discarded. The values of the gradient threshold and n were validated by visually inspecting 2000 velocity fields at each experimental run. The gradient threshold was set equal to 5 and 6 for low and high wind speeds, respectively, and the value of n was 3 for all runs. The percentage of bad frames detected by this scheme is tabulated in table 2.2. .

It was observed that the most of these bad frames were active wave crests that have high velocity gradients as well as large magnitude velocities. Therefore, by discarding these velocity fields from further analysis, the results are slightly biased. The Vorticity was computed using a central difference scheme. The uncertainty in the velocity and vorticity measurements was estimated to be $\pm$ 0.42 cm s^{-1} and $\pm$ 1.5 s^{-1}, respectively. Details of the error estimation for the velocity and vorticity are presented in Appendix A.

2.7 Computation of the Instantaneous Velocity Field

The complete procedure from the computation of the surface profile to the computation of the instantaneous velocity field is summarized below.

1. The surface wave profiles were computed from the profile images.
2. The surface profiles computed from the profile images were imported into the corresponding DPIV images to locate the air-water interface.
3. Once the interface is located in the DPIV image, all the pixels above the interface were set equal to the background gray-scale value to remove the reflected bright regions.
4. The velocity vectors were computed from the preprocessed DPIV images by using the cross-correlation algorithm.
5. The velocity vectors above the air-water interface were discarded as these were the false vectors.
6. The spurious velocity vectors were detected and corrected by using the local median test.
7. The bad velocity fields were detected by using a gradient velocity threshold and excluded from further computations.

This procedure is illustrated in figures 2.5, 2.9, and 2.10. A typical profile image at a wind speed of 8.1 m s^{-1} is displayed in figure 2.5 (a). Figure 2.5 (b) shows the profile image after applying the gray-scale threshold and performing the morphological operations. The profile image with the computed surface wave profile overlaid on it is shown in figure 2.5 (c). This surface wave profile was imported into the corresponding DPIV image, see figure 2.9 (a). The bright regions and reflected particles are visible

above the air-water interface. All the bright pixels above the interface were set to the gray-scale value of the background to avoid false correlation peaks and consequently incorrect velocity measurement. The preprocessed DPIV image is shown in figure 2.9(b). The instantaneous velocity field obtained from the corresponding DPIV image pair is shown plotted in figure 2.10.

U_∞ (m s^{-1})	6.3		8.1	
Run type	Clean	Contaminated	Clean	Contaminated
T_{air} (°C)	24.3	25.7	24.8	25.2
RH	57.5	56.5	57.6	56.7
T_{water} (°C)	25.4	24.7	24.7	25.0

Table 2.1: Summary of the environmental parameters for different experimental runs. U_∞, wind speed; T_{air}, the average air temperature; RH, the average relative humidity of the air; T_{water}, the average water temperature.

U_∞ (m s^{-1})	6.3		8.1	
Run type	Clean	Contaminated	Clean	Contaminated
Percentage	8.95	8.18	5.75	1.28

Table 2.2: The percentages of bad frames detected by the velocity gradient scheme.

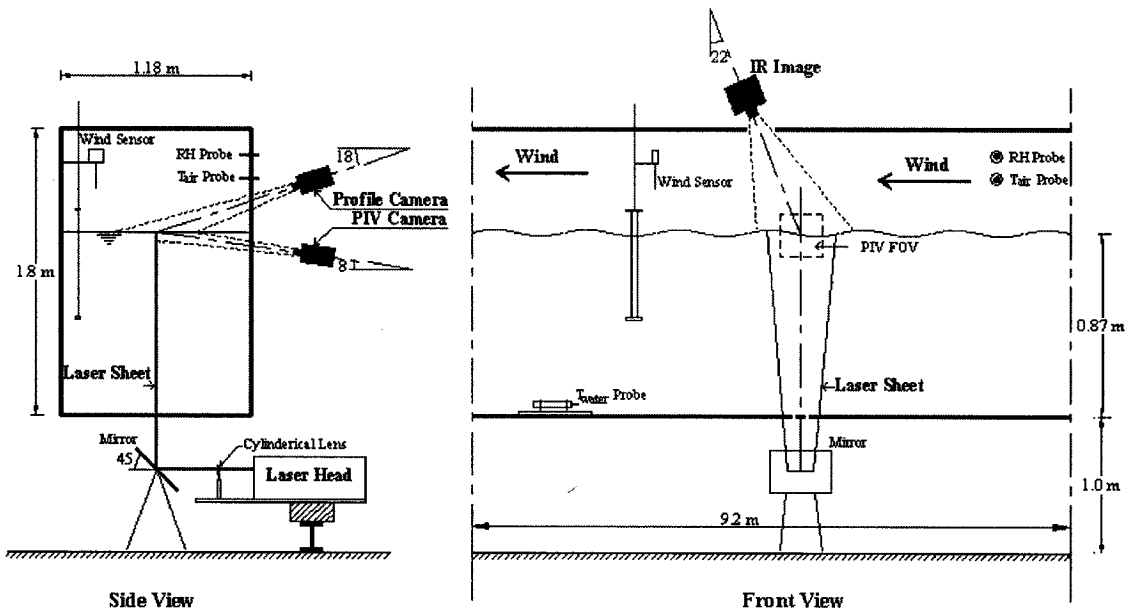

Figure 2.1: A schematic of the experimental setup and instrumentation in the wind-wave flume (no to scale)

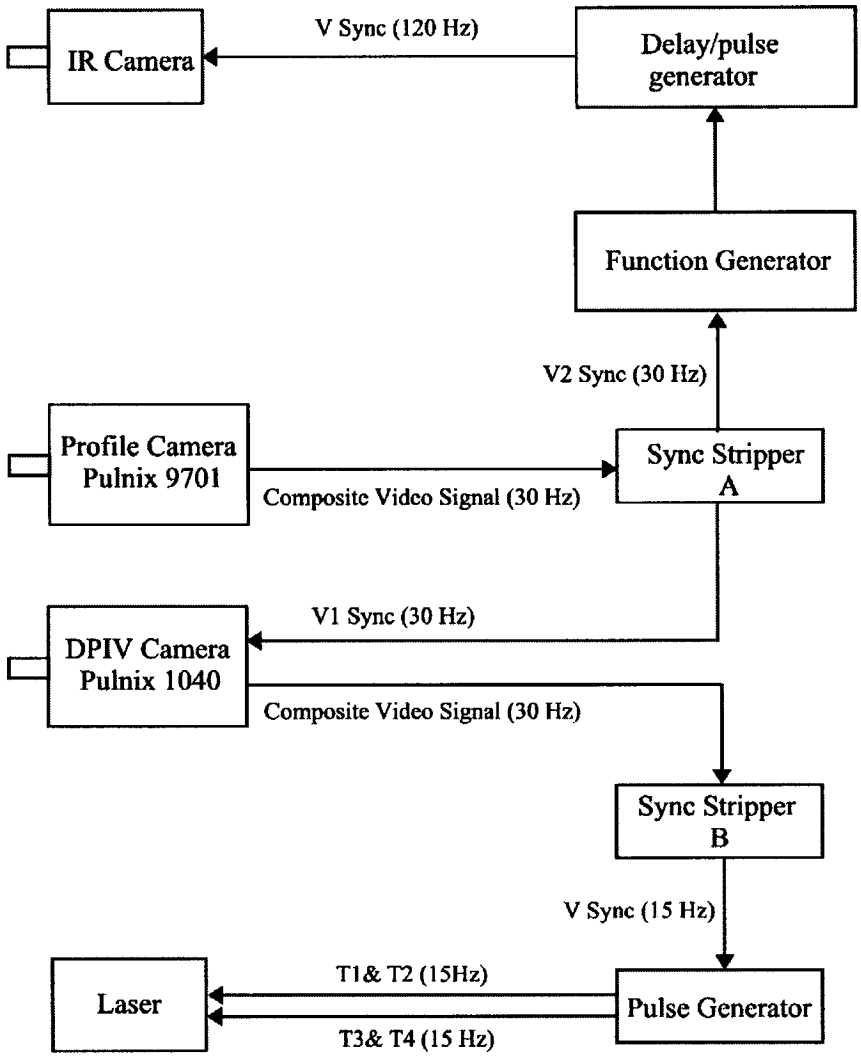

Figure 2.2: A flow chart showing the synchronization of the DPIV, profile, and IR cameras, and the laser. The vertical sync signal from the profile camera was used to synchronize the IR and DPIV cameras. The vertical sync signal from the DPIV camera was used to synchronize the laser.

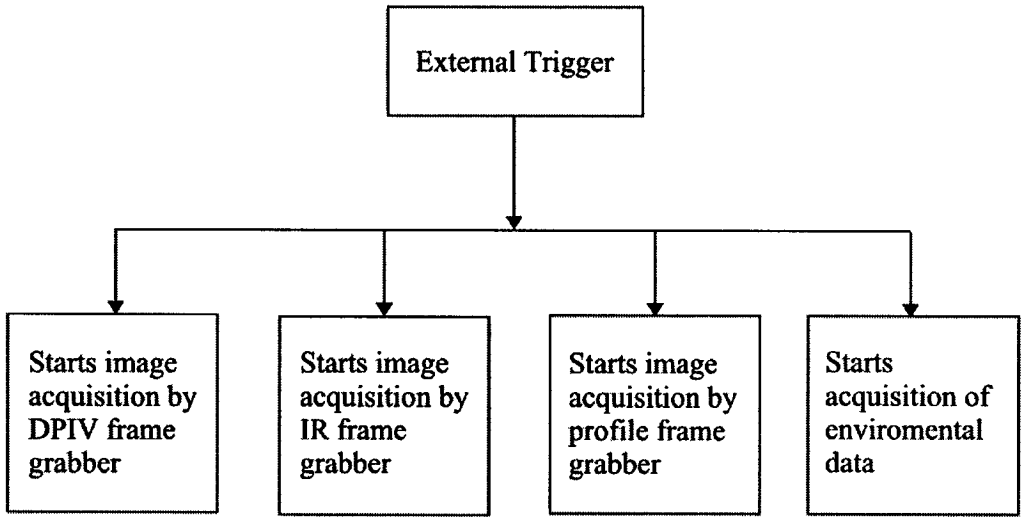

Figure 2.3: Flow chart showing the trigging sequence for the data acquisition.

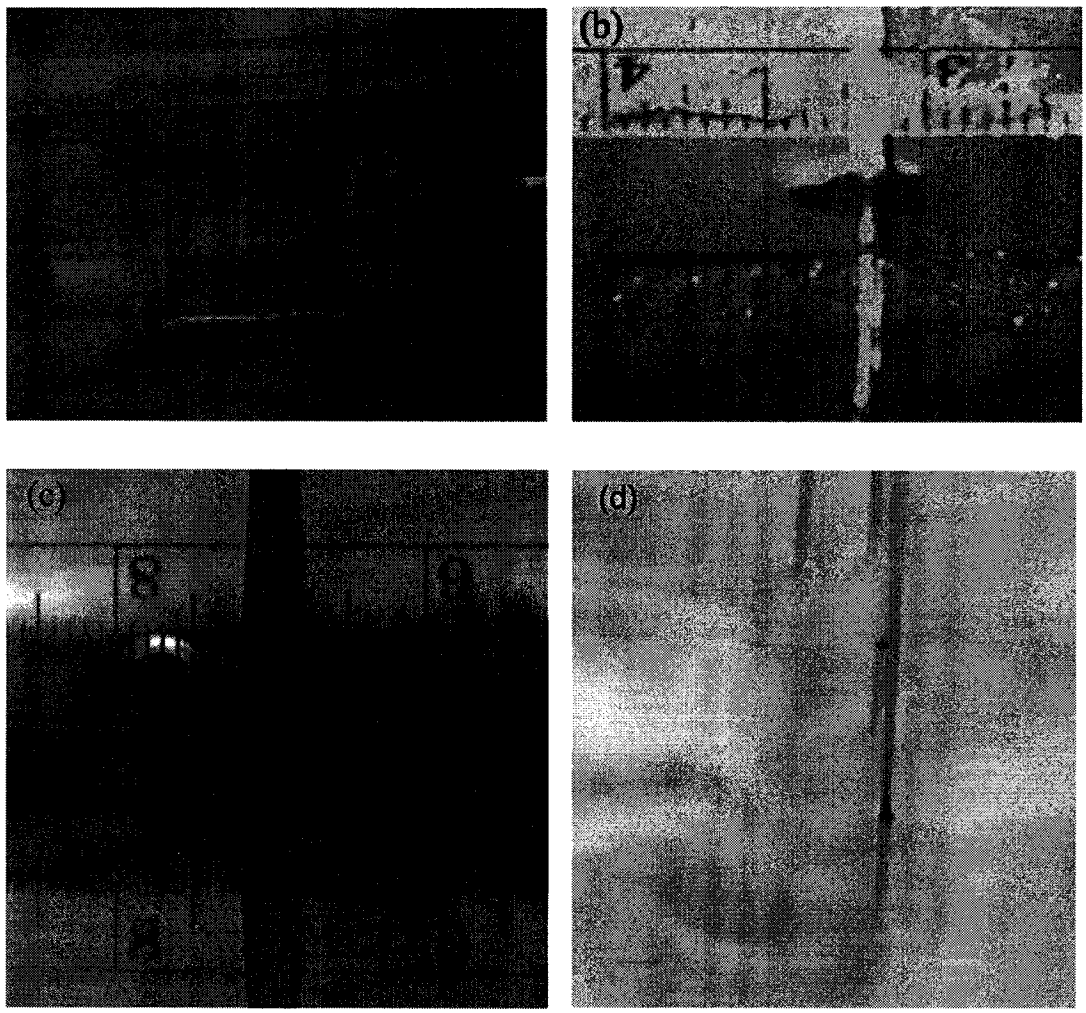

Figure 2.4: (a) The rigid block with vertical shafts and a ruler. The collocation images from (b) profile camera, (c) DPIV camera, (d) IR imager.

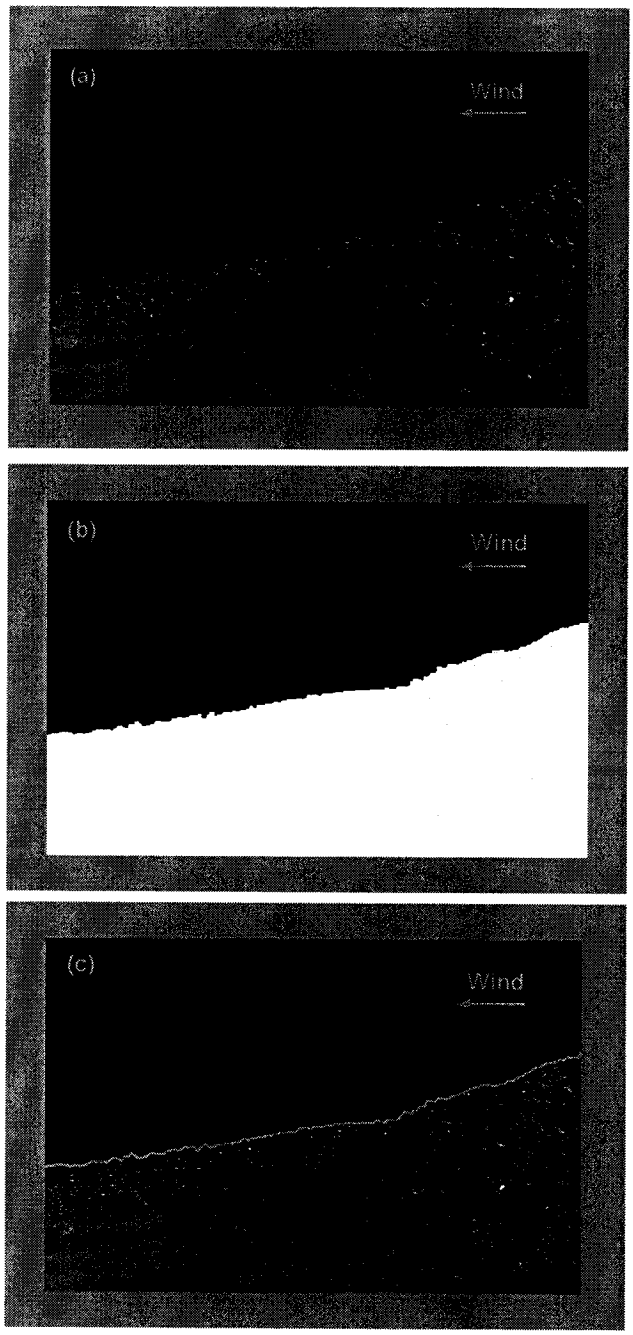

Figure 2.5: (a), A digital video image from the profile camera taken at a wind speed of 8.1 m s^{-1}. The difference in the gray scale values on the airside and waterside is visible in the image; (b), The image after applying the gray-scale threshold and morphological operations; (c), The computed air-water interface (white line) over laid on the profile image.

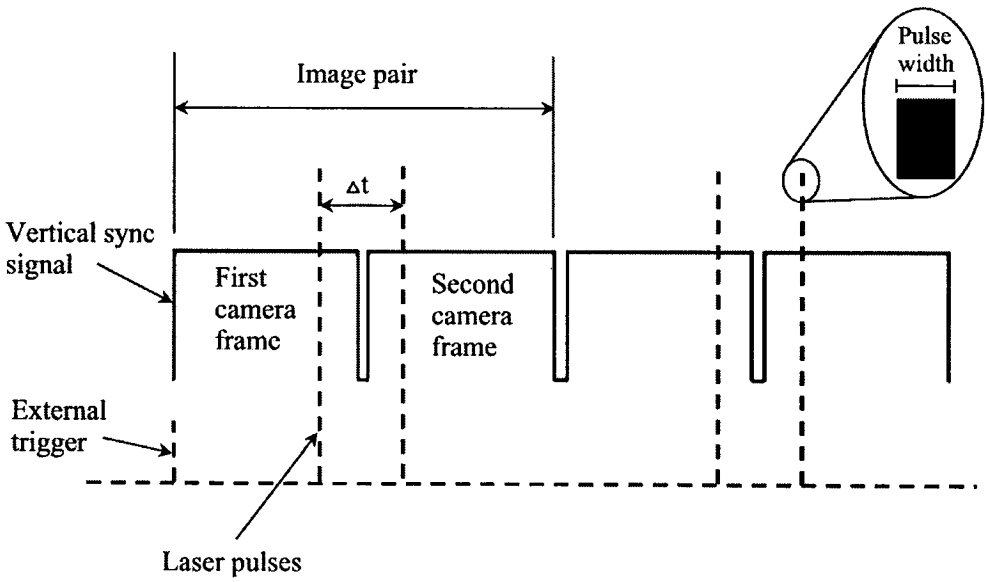

Figure2.6: The diagram showing the timing of the laser pulses in an image pair. A pulse generator controls the timing and duration of each laser pulse (Siddiqui 2002).

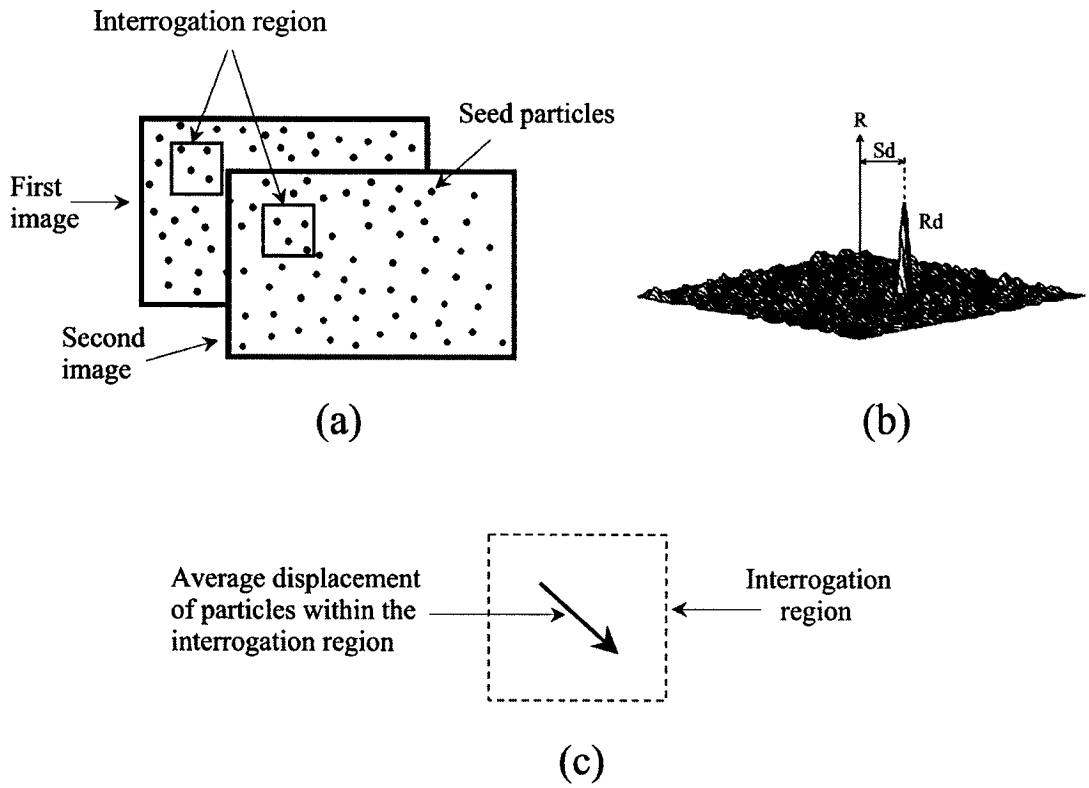

Figure2.7: (a), A PIV image pair. Each image pair is divided into small interrogation regions; (b), Correlation plane, obtained by cross-correlating the interrogation region in the first image with the corresponding search region in the second image; (c), The peak in the correlation plane gives the average displacement of the particles within the interrogation region (figure not to scale) (Siddiqui 2002).

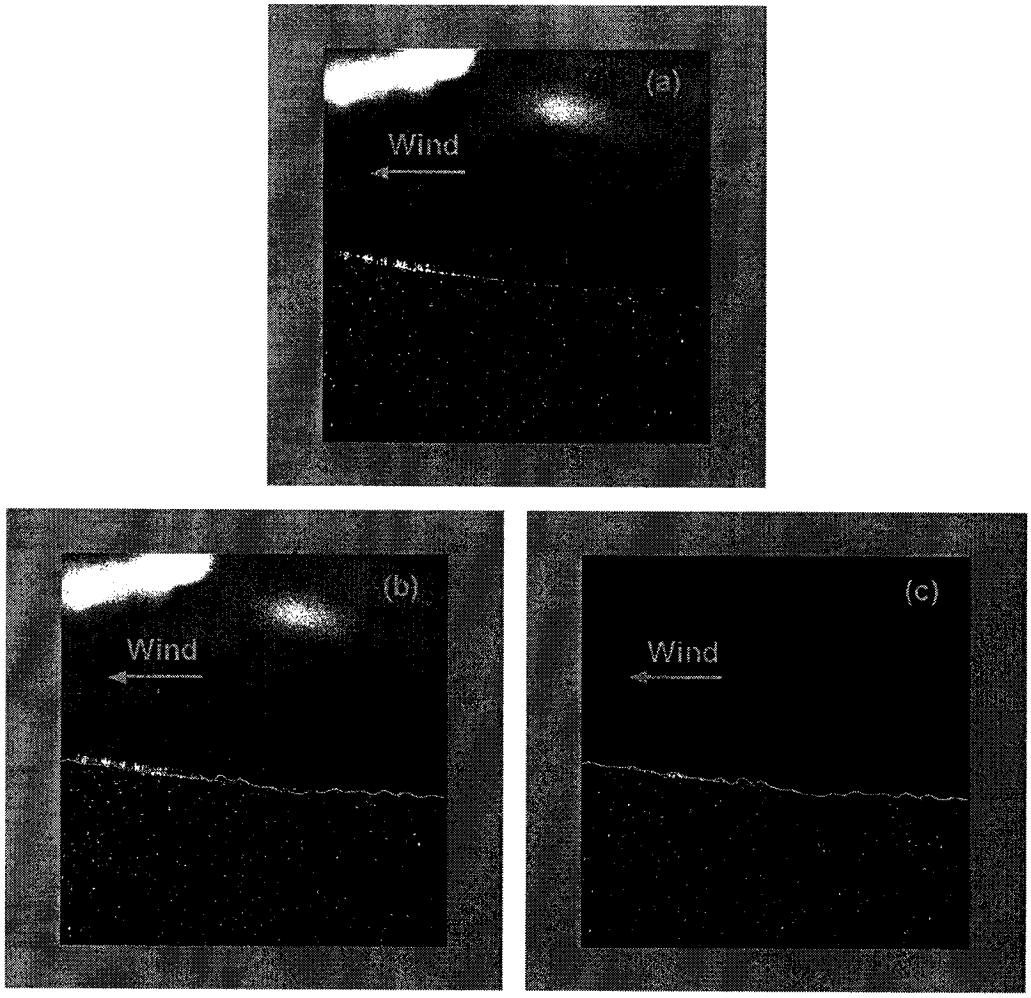

Figure 2.8: (a), A raw image from the DPIV camera. The air-water interface is clearly visible in the down wind region of the image;(b), The imported surface profile from the corresponding profile image is plotted in the DPIV image. The visible part of the interface in the DPIV image was used to determine the vertical offset for the imported surface profiles;(c), The DPIV image after setting the bright pixels above the interface equal to the background gray-scale value.

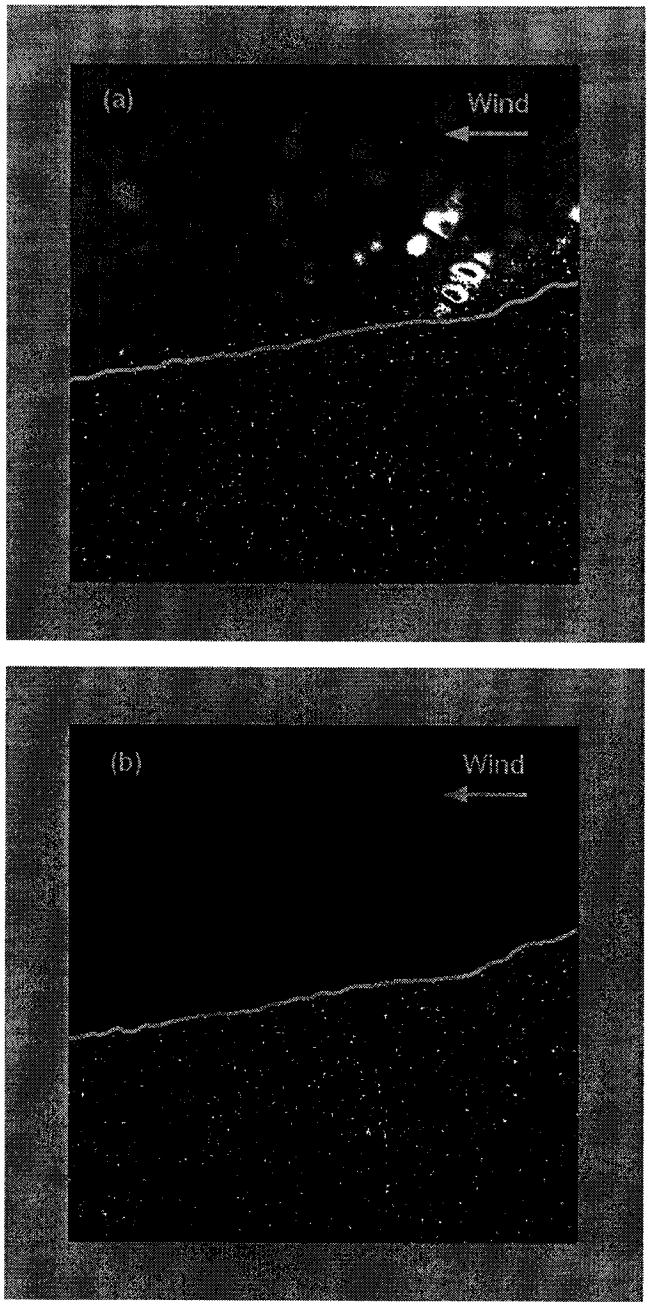

Figure 2.9: (a), The DPIV image corresponding to the profile image shown in figure 2.5. The air-water interface is not visible in this image due to the reflection of the tracer particles. The surface profile from figure 2.5 is imported to locate the interface and is plotted as a white line; (b), The DPIV image after preprocessing.

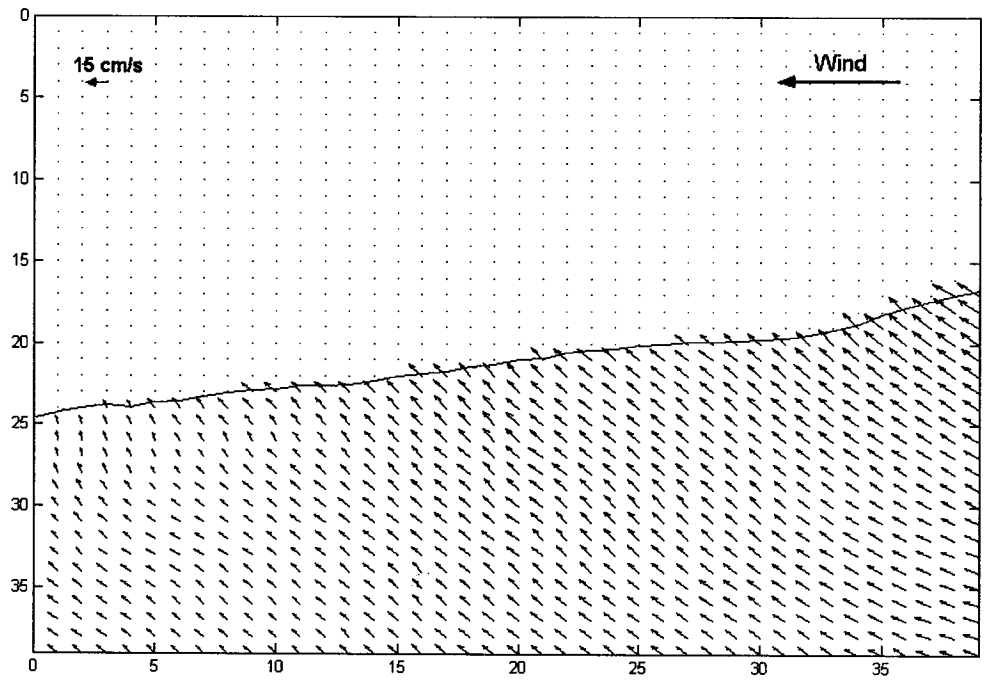

Figure 2.10: The two-dimensional instantaneous velocity field obtained by processing the DPIV image pair from figure 2.9. This velocity field is obtained after correcting the spurious vectors. The nearest velocity was measured on average, within 0.4 mm from the water surface.

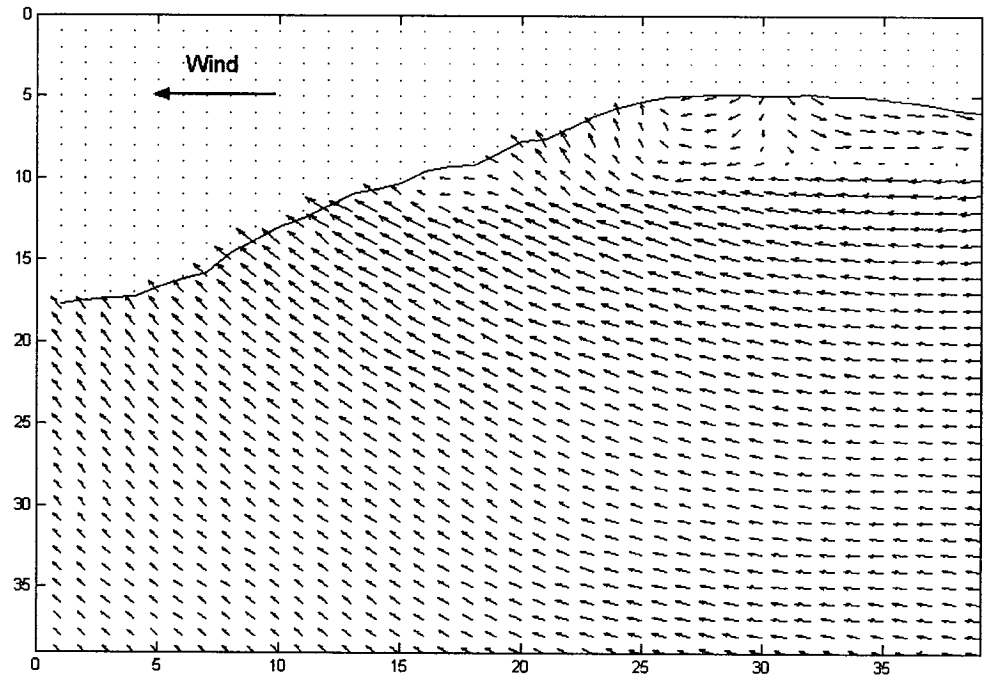

Figure 2.11: A two-dimensional velocity field with incorrect velocity vectors in the crest region due to the high velocity gradient at a wind speed of 8.1 m s^{-1}.

CHAPTER 3

Wind Drift Layer Characteristics

In this chapter we will discuss different flow properties computed beneath wind waves in the near-surface region. This region is also called the wind drift layer.

3.1 Wave Properties

The dominant frequency (f_d), the RMS wave height (H_{rms}), and the significant wave height (H_s) were computed from the surface profile data, and the dominant wavelength (λ_d) was calculated from the deep-water dispersion relationship. The deep-water dispersion relationship is given by,

$$\omega^2 = gk \tag{3.1}$$

where ω is the frequency in rad s^{-1}, k is the wavenumber and g is the acceleration due to gravity (Dean and Dalrymple 1991). The values of these parameters are presented in table 3.1. The results show that there is no significant difference in the frequency and wavelength of the dominant waves for clean and surfactant-contaminated surfaces, however, in the presence of surfactants, the RMS wave height and the significant wave height decreased by 19% and 24% for 6.3 and 8.1 m s^{-1} wind speeds, respectively. The frequency spectrum was computed from the time series of the surface displacement extracted at five different spatial locations in the wave profile. The spatially averaged frequency spectrum is plotted in figure 3.1 for both wind speeds. The plots show that the

wave energy beneath the clean surface is higher than that beneath contaminated surface for both wind speeds. The energy of the dominant wave beneath clean surface is approximately 40% and 60% higher than the dominant wave energy beneath the surfactant contaminated surface at 6.3 and 8.1 m s^{-1}, respectively.

3.2 Velocity Analysis

The DPIV measurements give the instantaneous velocity field in a fixed Eulerian coordinate system. As mentioned earlier, the vertical distance between two grid points is 0.8 mm. This distance was significantly smaller than the RMS wave height for all runs. As a result, the water surface fluctuated above and below any fixed grid point that is located between the crest and trough of a wave. Therefore, the time-averaged quantities (e.g. velocity) at this grid point could not be computed since this point remains in water when a wave crest passed through it and it remains in air when a wave trough passed through. Hsu *et al.* (1981) argued that the time-averaged quantities does not exist in a useful form at a fixed position in the crest-trough region because this fixed position is sometimes in the water and sometimes in the air. They also argued that the velocity field could be represented in a meaningful way if it is referenced to the fluctuating water surface. They transformed the fixed Eulerian coordinate system to the wave-following Eulerian system by transforming the vertical coordinate. Following the method described by Hsu *et al.* (1981), the velocity data was transferred from a fixed Eulerian to a wave following Eulerian system by transforming the vertical coordinate. The origin in the wave-following coordinate system was defined as the air-water interface, that is, the vertical coordinate $\zeta = 0$ at the interface and the negative ζ -axis points downwards. The

velocity grid points are 0.8 mm apart vertically and therefore, the instantaneous free surface was located anywhere from 0 to 0.8 mm above the grid point closest to the interface. As a result, the nearest velocity grid point was located 0.8 mm or less from the interface and therefore, on average, the near-surface velocity was measured within 0.4 mm of the interface. Thus, on average the first grid point below the interface was located at ζ = -0.4 mm. The velocity data at all wind speeds were transformed into the wave-following coordinate system up to a maximum depth of ζ = -9.2 mm (i.e. 12 grid points in vertical). The restriction of the coordinate transformation to a depth of 9.2 mm was due to the fact that beneath the troughs of some waves, depths greater than or equal to 9.2 mm were located below the field of view of the DPIV camera.

3.2.1 Mean Velocity

The mean velocity component was computed by time-averaging the instantaneous velocity at a given grid point in the wave-following coordinate system. Figure 3.2(a) presents the vertical profiles of the mean velocity components. The plot shows that the mean streamwise velocity decreases with depth and increases with wind speeds. At a given wind speed near the surface, the mean streamwise velocity in the presence of surfactants is considerably large as compared to the clean surface. At a depth of 0.4 mm, the mean streamwise velocity beneath the surfactant-contaminated surface is 25-30% larger than the ones beneath clean surface at both wind speeds. The profiles also indicate that the mean streamwise velocity gradient in the top 2 mm layer for the contaminated surface is a factor of 2 to 2.3 larger than that for the clean surface. The plot also shows that the mean streamwise velocity at the top three grid points (i.e. 0.4 mm to 2 mm below

the surface) varies linearly at all wind speeds. This linear velocity profile indicates of the presence of the viscous sublayer in that region (Kundu and Cohen 2002). We were not able to measure the surface velocity, and mentioned earlier, the closest measurement we could get was 0.4 mm from the surface. However, due to the presence of the linear velocity profile in the viscous sublayer, the mean surface velocity was estimated by extrapolating the mean streamwise velocity profile at the top three grid points, to the surface. The values of the mean surface velocity, U_s, are presented in table 3.2. The results indicate that the surface velocity at the contaminated surface is 30% higher than the clean surface at both wind speeds. Figure 3.2(a) also shows that as expected, the mean vertical velocity is close to zero for all runs. When the mean velocity profiles are plotted on a semi-logarithmic scale in figure 3.2(b), the profiles appear to be approximately linear below a depth of 3 mm (i.e. outside the viscous sublayer), indicating that they are logarithmic.

3.2.2 Wave Velocity

The instantaneous velocity field beneath wind waves consists of three components; the mean, wave, and turbulent velocities (Benilov *et al.* 1974). Separation of the mean velocity component is straightforward; however, the separation of the wave and turbulent velocity components is not trivial. The difficulty arises when the objective is to obtain the turbulent velocity field, that is, the separation of the turbulent velocity field from the wave velocity field, especially at the scales where both velocity components overlap. Several methods have been developed for performing this decomposition (for example, Jiang et al. 1990; Thais and Magnaudet 1996). However,

these methods relied on the assumptions that the waves were two-dimensional and that the waves were non-dispersive, which is a questionable assumption for wind waves. Since the magnitude of the wave energy is significantly larger than the turbulent energy, Siddiqui and Loewen (2004) argued that the leakage of even very small percentage of the wave velocity component into the turbulent velocity component could significantly overestimate the magnitude of turbulent energy. However, if the objective is to obtain the wave velocity field, then very small leakage of wave energy (at higher frequencies) into turbulent velocity field does not alter significantly the magnitude of the separated wave energy component.

The frequency spectra in figure 3.1 indicate that the wave velocity field is resolved in time, in the given data. Thus, wave velocity was separated by band-pass filtering the velocity data in time. The cutoff frequencies for band-pass filtering were chosen where the energy decreased to 3% of the maximum energy (i.e. the energy at the peak of the frequency spectrum that corresponds to the dominant wave). A 12^{th} order butterworth filter was used for the filtering.

The vertical profiles of the RMS streamwise and vertical wave velocity components are plotted in figure 3.3 (a) and (b), respectively. The results show that as expected the wave velocity decreases with depth and wind speed. At a given wind speed, the wave energy is higher beneath the clean surface, which is due to the surfactant tends to damp the wave field.

3.3 Shear Stress Analysis

3.3.1 Wind Stress

The velocity in the airside boundary layer was measured using an air velocity transducer (FMA-905-V, Newport Electronics Inc., Santa Ana, CA). Velocity measurements were made from a distance 5 cm above the mean water level to a distance 23 cm above the mean water level, at increments of 2 cm (i.e. the air velocity measurements were obtained at 10 vertical locations). The logarithmic mean velocity relation for the airside boundary layer is given as,

$$\frac{U_a}{u_{*a}} = \frac{1}{\kappa}\ln\left(\frac{z}{z_{oa}}\right) \tag{3.2}$$

where, U_a is the average wind velocity, κ is the Von Karman constant, z is the distance from the water surface and z_{oa} is the airside roughness length (Schlichting 1979). The airside friction velocity u_{*a} was computed by fitting equation (3.2) to the average wind velocity profiles. The values of u_{*a} are presented in table 3.2.

The wind stress was computed using the relation,

$$\tau_a = \rho_a u_{*a}^2 \tag{3.3}$$

where ρ_a is the density of air. The values of τ_a are presented in table 3.2. The results show that τ_a is approximately the same for the clean and surfactant cases at the lower wind speed. Whereas, at the higher wind speed, the wind stress for the clean surface is 15% higher than that of the contaminated surface. That is, more wind shear is transferred to the water column when the surface is clean.

3.3.2 Total Waterside Stress

The total shear stress in the water at any particular depth can be computed using the relation,

$$\tau_{total} = \rho \overline{u_i w_i} \tag{3.4}$$

where, u_i and w_i are the instantaneous streamwise and vertical velocities, respectively, at a particular depth. The values of the total waterside stress computed at depths from 0.4 mm to 9.2 mm from the surface are presented in tables 3.3 to 3.6 for clean and surfactant cases at both wind speeds. The results indicate that the total stress decreases significantly within the viscous sublayer. It decreased by 60% in the viscous sublayer at the lower wind speed for both cases. Whereas, at the higher wind speed, the total stress decreased by 43% and 54% for the clean and surfactant cases, respectively. Below the viscous sublayer, the total stress increased with depth. It increased between 7% and 15% from a depth of 2.8 mm to 9.2 mm for all cases except for the surfactant case at 8.1 m s^{-1}, where it increased by 38%.

Due to the continuity of the stress across the air-water interface, the total stress transferred to the water should be the same as the wind stress. The values of the total waterside stress computed at a depth of 0.4 mm, and the wind stress are plotted in figure 3.4. The results show that except for the clean case at 6.3 m s^{-1} wind speed, the values of the total stress and the wind stress are with in 10%. For the clean surface at 6.3 m s^{-1}, the wind stress is approximately 24% larger than the total stress. With the uncertainty in the air velocity measurements and the total waterside stress computation, these values from two independent sets of measurements are considered to be in a good agreement. This means that the total waterside stress computed at a depth of 0.4 mm represents the total

stress transferred to the water from the wind. The total shear stress on the waterside is comprised of viscous stress, wave stress, turbulent or Reynolds stress, and the stresses due to the mean-wave-turbulent interactions (Jiang et al. 1990). As mentioned earlier, in the present study, it was not possible to decompose the turbulent velocity field. Therefore, the only stress components possible to compute were the viscous and wave stresses.

3.3.2.1 Viscous Stress

The viscous stress, τ_{visc}, was estimated by,

$$\tau_{visc} = \mu \frac{dU}{dy} \tag{3.5}$$

where, dU/dy is the mean streamwise velocity gradient. The viscous stress was computed from the velocity gradient between the mean surface velocity and the mean streamwise velocity at a depth of 0.4 mm. The values of the viscous stress are also presented in tables 3.3 to 3.6. The results show that for a given surface condition, the viscous stress increases with wind speed. At a given wind speed, the viscous stress in the presence of surfactant is a factor of 2 to 2.3 larger than the clean surface. This is also evident in the mean velocity profiles in figure 3.2 where large velocity gradients are observed in the presence of surfactant.

3.3.2.2 Wave Stress

The wave stress, τ_{wave}, was computed by,

$$\tau_{wave} = \overline{\rho \tilde{u} \tilde{w}} \tag{3.6}$$

where $\tilde{u}$ and $\tilde{w}$ are the streamwise and vertical components of the wave velocity, respectively. The values of τ_{wave} are tabulated in tables 3.3 to 3.6. The results indicate that as expected the wave stress decreases with depth. At a depth equal to the significant wave height, the wave stress is reduced to approximately 10% of the maximum wave stress for both conditions and wind speeds. The results also show that for the surfactant case, the maximum wave stress is approximately 60% of the total stress. Whereas, for the clean case, the maximum wave stress is 50-55% of the total stress.

3.3.3 Friction Velocity

The mean streamwise velocity distribution in a neutral aqueous boundary layer is given by,

$$\frac{U_s - U(\zeta)}{u_*} = \frac{1}{\kappa}\ln\left(\frac{\zeta}{z_o}\right) + C \tag{3.7}$$

where, U_s is the surface velocity, U is the mean streamwise velocity, u_* is the friction velocity on the waterside, z_o is the roughness length, κ is the Von Karman constant and its typical value is 0.4 and the constant C which has value of 5.5 and 8.5 for a smooth and rough flow; respectively (Schlichting 1979). In figure 3.2(b), it was demonstrated that the mean streamwise velocity profiles were approximately logarithmic at depths greater than 3.5 mm. The $U(\zeta)$ and U_s were measured as described in section 3.2.1. The values of the friction velocity u_* were obtained by fitting the above equation to the mean streamwise velocity profiles shown in figure 3.2(a) for depths greater than 3.5 mm. The values of the waterside friction velocity are presented in table 3.2. The results show that

in the presence of a surfactant, the friction velocity increased by 32% and 50% for the lower and higher wind speeds, respectively, compared to the clean water surface.

3.3.4 Mean Velocity in Wall Coordinates

The mean streamwise velocity profiles are plotted in the form of a velocity defect law in wall coordinates in figure 3.5. The non-dimensional velocity defect is defined as,

$$u^+ = (U_s - U)/u_* \tag{3.8}$$

where U_s is the surface velocity, U is the mean streamwise velocity and u_* is the waterside friction velocity. The non-dimensional wall coordinate is defined as,

$$y^+ = \zeta u_* / \nu \tag{3.9}$$

where ν is the kinematic viscosity of water and ζ is the distance measured from the water surface (Schlichting 1979). The plot shows that for both surface conditions at the higher and lower wind speeds, flow is in the inner region i.e. y^+ less than 30. The viscous sublayer is also manifested in the plot for $y^+ < 10$. The figure shows that the viscous sublayer is more prominent in the presence of surfactant. The plot also shows that the mean velocity profiles for both surface conditions at both wind speeds collapsed into a narrow band. The results indicate that u_* is an appropriate scaling parameter for both surface conditions. The mean velocity profiles beneath the surfactant-contaminated surface lie above the mean velocity profiles beneath the clean surface. This indicates that the surface roughness is lower in the presence of surfactant. This is an expected behavior because surfactant damps the small-scale waves resulting in a decrease in the surface roughness.

3.4 Spectral Analysis

The one dimensional wavenumber spectra of the streamwise velocity are presented in figures 3.6 and 3.7 for both surface conditions at 6.3 m s^{-1} and 8.1 m s^{-1} wind speeds, respectively. The figures show spectra at 0.4, 4.4 and 9.2 mm depths. The spectra were computed in the wave-following coordinate system. The plots show that for all cases, the wave number spectra have an inertial subrange, that is, a range of wave number for which the slope of the spectrum is approximately –5/3. Note that the kinetic energy within this range is solely due to turbulence, and is not significantly affected by wave orbital motion (Terray et al. 1996). At a particular depth, the energy of the wave number spectra increased with wind speed. Loewen and Siddiqui (2004) found a similar trend for k>200 in the wind speed range 6.1-11 m s^{-1}. The magnitudes of the spectral energy in the wave number spectra for clean surface condition at the depth of 0.4mm are comparable with their results at a depth of 1 mm for the wavenumber range $300 < k < 1000$ rad m^{-1}. The plots also show that the spectral energy decreases in the presence of surfactant; however, the percentage decrease in the energy is not significant. At a depth of 0.4 mm, the inertial subrange is prominent in the wave number range $700 < k < 3000$ rad m^{-1}. However, at greater depths, the inertial subrange is restricted to a smaller range of higher wavenumbers. The manifestation of the inertial subrange in the wavenumber spectra at a depth of 0.4 mm indicates that the turbulence is not zero within the viscous sublayer.

3.5 Energy Dissipation

The rate of turbulent kinetic energy dissipation, ε, is a measure of the turbulence and the availability of energy for the heat and mass transport. Different methods have

been used to estimate the rate of energy dissipation. Doron et al. (2001) compared five different methods for the estimation of the energy dissipation and showed that the method based on the turbulent velocity gradients obtained from the DPIV measurements, was the most accurate. This method could not been used in the present study, since the turbulent velocity was not separated. Therefore, the energy dissipation was estimated by fitting a line to the wave number spectrum of the streamwise instantaneous velocity within the inertial subrange. The rate of energy dissipation within the inertial subrange is given by,

$$\Phi_u(k) = \frac{18}{55}\left(\frac{8}{9\alpha}\right)\varepsilon^{2/3}k^{-5/3} \tag{3.10}$$

where, Φ_u is the wavenumber spectrum of the streamwise velocity, k is the wavenumber within the inertial subrange and α is a constant equal to 0.4 (Hinze 1975; Veron & Melville 1999). The ε was estimated at each depth by fitting the line given by equation (3.10) to the wavenumber spectrum at that depth. Figure 3.8 presents the vertical profiles of ε at two wind speeds for the clean and surfactant-contaminated surfaces. The plot shows that ε increases with wind speed. Near the surface, it increased by a factor of approximately three as the wind speed increased from 6.3 to 8.1 m s^{-1}. The plot also shows that ε increases significantly towards the surface at both wind speeds and both surface conditions. The profiles in figure 3.8 indicate that the value of ε decreases significantly within the viscous sublayer. Within the viscous sublayer, the decrease in ε is approximately linear. Below the viscous sublayer, ε decreases less rapidly up to a depth approximately equal to the RMS wave height. Below this depth, ε becomes approximately constant at all conditions and wind speeds. This indicates that within the wave field, the dissipation is significantly enhanced. Siddiqui and Loewen (2004) have

also observed a similar trend in the vertical profiles of ε. Comparison of the rate of energy dissipation beneath clean and contaminated surfaces shows that at the lower wind speed, the values of ε are approximately the same for both surface conditions. However, at the higher wind speed, near the surface at a depth of 0.4 mm, the rate of energy dissipation is higher beneath the surfactant-contaminated surface compared to the clean surface. But within the viscous sublayer, the value of ε decreases more rapidly beneath the contaminated surface. Within the viscous sublayer at the higher wind speed, the value of ε decreased by a factor of three beneath the clean surface and by a factor of four beneath the contaminated surface. At the lower wind speed, ε is decreased by a factor of more than three within the viscous sublayer at both surface conditions. Below the viscous sublayer at the higher wind speed, the value of ε remains approximately a factor of two higher beneath the clean surface as compared to the contaminated surface. The higher dissipation within the viscous sublayer could be the reason for the significant decrease in the total and wave stresses within the viscous sublayer.

The rate of energy dissipation beneath wind waves is usually expressed in a normalized form using wall layer parameters, which are the friction velocity, depth and the acceleration due to gravity (Soloviev et al. 1988). For a wall layer or constant stress layer, the normalized dissipation would be unity at all depths (Agrawal et al. 1992). The normalized rate of energy dissipation is plotted in figure 3.9 for both wind speeds and both surface conditions. The plot shows that the normalized dissipation does not follow the constant stress layer profile. The plot also indicates that for the clean surface, the normalized dissipation is higher than that for the contaminated surface. This could be

because the friction velocity, which is a normalizing parameter, is higher beneath contaminated surfaces and then reduces the magnitude of the normalized dissipation.

3.6 Discussions and Conclusion

The results in table 3.1 show that the RMS wave height was reduced by 19% to 24% in the presence of surfactant. Consequently, the energy of the waves was reduced by approximately 40% to 60% as it is correlated with the amplitude square of the wave. Mitsuyasau and Honda (1986) investigated the impact of a surfactant on wind waves by varying the surfactant concentration. They observed that the spectral energy in the frequency spectrum of surface displacement decreased with an increase in the surfactant concentration, which is consistent with our results. They argued that the damping of small waves by the surfactant changes the water surface roughness and that results in a change in the energy flux from the wind to the waves. Mitsuyasu et al (1982) found that the wind velocity profiles were changed due the suppression of waves by the surfactant. They observed that the wind velocity profile had larger slope and higher surface velocity in the presence of surfactant and this trend increased with wind speed. They found an increase in the surface velocity by 25-30% in the presence of surfactant. Their results also indicate that there is no significant difference in the airside friction velocity beneath clean and surfactant-contaminated surfaces at wind speeds lower than 7 m s^{-1}. They argued that the surfactant reduces the drag coefficient at this wind speed range and that the wind waves generated at a lower wind speed do not contribute to the water surface roughness and hence, at wind speeds lower than 7 m s^{-1}, the friction velocity is not affected significantly by the surfactant. We observed the same trend for the air friction

velocity. At 6.3 m s^{-1} wind speed, the friction velocity was reduced by only 3% in the presence of surfactant. However, at 8.1 m s^{-1} wind speed, the surfactant caused a reduction in the airside friction velocity by 8%. Moreover, the increase in the surface velocity for the surfactant-contaminated surfaces observed in this study, which is about 30% for both wind speeds, is consisted with their observation.

In the presence of a surfactant, surface tension gradients are generated, which contribute to the viscous stress (Lucassen et al.1969). The results in table 3.2 show that the viscous stress increased in the presence of surfactant. The viscous stress is proportional to the mean velocity gradient at the surface. Thus, at a given wind speed, the higher mean velocity gradients observed beneath the surfactant-contaminated surface was likely due to the surface tension gradients. Thus, the impact of the surfactant on the wind-wave coupling can be described as follows. The surfactant damps the small waves, which result in a reduction of the surface roughness on the airside. This smoother surface causes a reduction in the drag and hence the wind stress. The decrease in the wind stress results in a decrease in the airside friction velocity. On the waterside, the surfactant induces surface tension gradients, which increase the magnitude of the viscous stress. This results in an increase in the waterside friction velocity.

The wavenumber spectra of the streamwise velocity at both wind speeds and both surface conditions show a prominent inertial subrange at a depth of 0.4 mm from the surface i.e., within the viscous sublayer. The presence of the inertial subrange is proof that the turbulence exists within the viscous sublayer, since the energy transfer in the inertial subrange is purely due to turbulence (Hinze 1975). The spectral energy in the inertial subrange provides an estimate of ε, the rate of turbulent kinetic energy

dissipation. However, it could not be used to estimate the total turbulent kinetic energy because the wavenumbers corresponding to the inertial subrange are significantly higher than those of the energy containing eddies (Hinze 1975). Furthermore, as discussed earlier, it was not possible to compute Reynolds stresses in this study; therefore, the turbulent energy production could not be computed. Nevertheless, evidence of the existence of turbulence within the viscous sublayer adjacent to the wind-driven air-water interface is an important discovery that could help in improving the knowledge of the near-surface dynamics.

The friction velocity within the near-surface region can also be computed by,

$$u_* = \sqrt{\nu \frac{dU}{dy} - \overline{u'w'}} \tag{3.11}$$

where, ν is the kinematic viscosity, dU/dy is the mean velocity gradient and $\overline{u'w'}$ is the Reynolds stress. The first term on the right-hand side represents the viscous stress and the second term represents the turbulent or Reynolds stress (Donelan 1990). If it is assumed that the Reynolds stress is negligible as compared to the viscous stress, the friction velocity can be computed directly from the viscous stress as,

$$(u_*)_{visc} = \sqrt{\nu \frac{dU}{dy}} \tag{3.12}$$

where, $(u_*)_{visc}$ represents the friction velocity computed from the viscous stress. The equation (3.12) is equivalent to the relationship $u^+ = y^+$ that holds within the viscous sublayer (Schlichting 1979). At greater depths, the mean velocity gradients become smaller and the magnitude of the viscous stress decreases and the magnitude of the turbulent stress increases. Thus, at greater depths, the turbulent stress becomes the main

contributor to the friction velocity. The values of $(u_*)_{visc}$ obtained from equation (3.12) are tabulated in table 3.2. The result shows that at both wind speeds and for both surface conditions, the value of the friction velocity computed from the viscous stress is lower than that computed from the fit to the mean logarithmic velocity profile within the buffer layer (i.e. beneath the viscous sublayer). Wu (1975) also observed a difference in the friction velocity computed from the viscous stress and the logarithmic fit. He found that the difference increased with wind speed. He considered the uncertainty in the velocity measurements within the viscous sublayer as the reason for this trend.

There are two possible explanations for the higher value of the friction velocity obtained from the velocity data in the buffer layer. Firstly, the computation of the friction velocity in the viscous sublayer only from the viscous stress could underestimate the friction velocity value since the presence of turbulence within the viscous sublayer is evident. Therefore, one explanation for this behavior is that the magnitude of turbulent stress in the viscous sublayer is not negligible. As mentioned earlier, it was not possible to compute the magnitude of the turbulent stress; therefore, no quantitative comparison of the viscous and turbulent stresses within the viscous sublayer can be made. However, it has been argued that within the viscous sublayer at the air-water interface, the turbulence is suppressed and the magnitude of the turbulent stress is negligible as compared to the viscous stress (Donelan 1990). If this is the case, then the reason for the increase in the value of the friction velocity with depth could be different.

The other explanation for this trend is based on the assumption of a constant stress layer. The wall layer scaling in the form of the law of the wall or the velocity defect law are based on the assumption that the shear stress remains constant within the wall layer

i.e., the friction velocity is expected to be constant in this layer (Kundu and Cohen 2002). According to this assumption, within the wall layer, there is a balance between the viscous and turbulent stresses, such that the total stress remains constant. This implies that the friction velocity computed from equations (3.7) and (3.12) should be the same. The results indicate that the total shear stress increased with depth. If it is assumed that the magnitude of the turbulent stress is insignificant within the viscous sublayer beneath the air-water interface (Donelan 1990), than the higher shear stress implies that the turbulent stress beneath the viscous sublayer is larger in magnitude than that predicted for the constant stress layer. The theory of the constant stress layer was developed for the flow over a solid wall. It is not necessary that it should hold for the flow beneath the wind-shear driven air-water interface. The existence of a logarithmic velocity profile near a solid wall or near an air-water interface can be established with dimensional arguments (Kundu and Cohen 2002) and it does not necessarily imply that the two flow regimes are completely analogous.

One fundamental difference is the energy input mechanism for these two flow regimes. For flow over a solid wall, there is a flux of energy towards the wall from the outer region, originated from the mean flow. This energy is converted into turbulence in the wall layer. A part of this energy is dissipated within the wall layer and the remaining part is diffused back by turbulence to the outer region (Hinze 1975). Whereas, for the flow beneath the wind-shear driven air-water interface, the energy influx is from the surface towards the outer region (i.e. the deeper water). The distribution of this energy into different components is not well understood. However, a part of this energy is utilized in generating the waves and a part of this energy is contributing to the mean flow.

In this flow regime, the turbulence may be extracting its energy from two sources. The first source is the mean flow, which is a conventional source of turbulence. The second source is the wave motion from which the turbulence may be extracting its energy in the so-called wave-turbulence interactions (Jiang et al. 1990). The results in tables 3.3 to 3.6 show that at a depth of 0.4 mm, the wave stress constitutes 50-60% of the total stress. At greater depths, the wave fraction of the total stress decreases. The results in figure 3.3 also indicate a decrease in the wave velocity with depth. The mechanism of energy exchange between the wave and turbulence is very complex and not well understood. Kitaigorodskii and Lumley (1983) have argued that the primary effect of the wave-turbulence interaction is the downward transport of the wave kinetic energy, which due to the transformation of wave energy into turbulence, acts as a turbulent energy source. Thus, it is expected that the turbulent energy will increase with depth up to a certain level, where the wave-turbulence interactions become insignificant. Therefore, it can be argued that the near-surface layer beneath a wind-driven air-water interface is not a constant stress layer and that the turbulent shear stress and hence the friction velocity is expected to increase with depth. Thus, the value of the friction velocity obtained in a particular set of experiments depends on the flow region considered for the friction velocity measurements.

The results in figure 3.9 further strengthen the argument that the assumption of the constant stress layer does not hold for the flow beneath wind-shear driven air-water interfaces. In this plot, the rate of kinetic energy dissipation normalized by the wall coordinates, is plotted. In the presence of a constant stress layer, the data should collapse in a vertical line at $\varepsilon\kappa\zeta / u_*^3 = 1$ (Agrawal et al. 1992). The results in figure 3.9

show that for most of the data, the dissipation is enhanced with respect to the constant stress layer. In laboratory experiments, Siddiqui and Loewen (2004) and Thais and Magnaudet (1996) observed that the energy dissipation beneath the wind-generated waves does not scale with the constant stress layer. In the field, Agrawal et al. (1992) observed enhanced dissipation with respect to the constant stress layer.

The rate of energy dissipation is a characteristic property of turbulence. If the assumption of a constant stress layer is not valid for this property beneath wind-shear generated interfaces, then it is arguable that for other turbulent properties, this assumption is not valid either. From the given dataset, the change in the friction velocity was observed at the higher wind speed only. It should be noted that the region-of-interest in this study was restricted to the top 1 cm layer beneath the water surface, where it is possible that the variation in the turbulent shear stress is not very large. In a recent set of experiments, where the velocity fields were computed up to greater depths, different friction velocity values were estimated by fitting the logarithmic velocity profiles at different depths, indicating that the constant stress assumption is not valid in this flow regime (Elkamash and Loewen 2004).

In the present study, the flow field within the top 9 mm layer of water wave measured. This region lies within the active wave field, as the significant wave height is comparable to the depth of this region (see table 3.1). Figure 3.3 shows that at a depth of 9 mm, the magnitude of RMS streamwise and vertical wave velocity components is 60-70% of that at 0.4 mm depth. Thus, within the field of view of the present study, most of the wave energy is not transformed into the turbulent energy. Therefore, the friction velocity values computed in this study are lower than the ones obtained at greater depths.

U_∞ (ms^{-1})	6.3		8.1	
Run type	Clean	Contaminated	Clean	Contaminated
f_d (HZ)	4.70	4.60	3.70	3.80
λ_d (cm)	7.07	7.40	11.45	10.75
H_{rms} (cm)	0.47	0.38	0.75	0.57
H_s (cm)	0.69	0.56	1.11	0.85

Table 3.1 : U_∞, wind speed; f_d, the dominant wave frequency; λ_d, the dominant wavelength; H_{rms}, the RMS wave height; H_s, the significant wave height.

U_∞ (m s^{-1})	6.3		8.1	
Run type	Clean	Contaminated	Clean	Contaminated
U_s (cm s^{-1})	7.15	9.27	10	12.77
u_* (cm s^{-1})	0.25	0.32	0.33	0.48
u_{*a} (cm s^{-1})	39.8	39.2	63.7	59.2
τ_{wind} (kg/ms^2)	0.190	0.184	0.487	0.421
$(u_*)_{visc}$ (cm s^{-1})	0.21	0.30	0.26	0.39

Table 3.2: U_∞, wind speed; U_s, the surface velocity; u_*, the waterside friction velocity; u_{*a}, the airside friction velocity; τ_{wind}, the wind stress; $(u_*)_{visc}$, waterside friction velocity computed from the viscous stress.

ζ (mm)	τ_{total} (kg/ms^2)	τ_{wave} (kg/ms^2)	τ_{visc} (kg/ms^2)
-0.4	0.153	0.087	0.0044
-1.2	0.092	0.068	0.0044
-2.0	0.060	0.044	0.0044
-2.8	0.051	0.029	
-3.6	0.055	0.022	
-4.4	0.057	0.017	
-5.2	0.059	0.014	
-6.0	0.059	0.011	
-6.8	0.059	0.009	
-7.6	0.059	0.007	
-8.4	0.059	0.007	
-9.2	0.059	0.005	

Table 3.3: The values of the waterside stresses for the clean surface at 6.3 m s^{-1} wind speed; τ_{total}, the magnitude of total shear stress; τ_{wave} , the magnitude of wave stress; τ_{visc}, the magnitude of viscous stress.

ζ (mm)	τ_{total} (kg/ms^2)	τ_{wave} (kg/ms^2)	τ_{visc} (kg/ms^2)
-0.4	0.198	0.128	0.0089
-1.2	0.135	0.100	0.0089
-2.0	0.095	0.061	0.0089
-2.8	0.083	0.039	
-3.6	0.080	0.029	
-4.4	0.080	0.022	
-5.2	0.082	0.018	
-6.0	0.084	0.015	
-6.8	0.086	0.013	
-7.6	0.087	0.011	
-8.4	0.088	0.009	
-9.2	0.089	0.008	

Table 3.4: The values of the waterside stresses for the contaminated surface at 6.3 m s^{-1} wind speed; τ_{total}, the magnitude of total shear stress; τ_{wave} , the magnitude of wave stress; τ_{visc}, the magnitude of viscous stress.

ζ (mm)	τ_{total} (kg/ms^2)	τ_{wave} (kg/ms^2)	τ_{visc} (kg/ms^2)
-0.4	0.441	0.212	0.0065
-1.2	0.286	0.166	0.0065
-2.0	0.253	0.135	0.0065
-2.8	0.261	0.104	
-3.6	0.268	0.078	
-4.4	0.269	0.058	
-5.2	0.273	0.047	
-6.0	0.276	0.040	
-6.8	0.279	0.038	
-7.6	0.277	0.034	
-8.4	0.278	0.030	
-9.2	0.281	0.029	

Table 3.5: The values of the waterside stresses for clean surface at 8.1 m s^{-1} wind speed; τ_{total}, the magnitude of total shear stress; τ_{wave} , the magnitude of wave stress; τ_{visc}, the magnitude of viscous stress.

ζ (mm)	τ_{total} (kg/ms^2)	τ_{wave} (kg/ms^2)	τ_{visc} (kg/ms^2)
-0.4	0.403	0.251	0.015
-1.2	0.260	0.199	0.015
-2.0	0.185	0.110	0.015
-2.8	0.169	0.071	
-3.6	0.169	0.047	
-4.4	0.179	0.032	
-5.2	0.189	0.023	
-6.0	0.198	0.018	
-6.8	0.209	0.015	
-7.6	0.218	0.013	
-8.4	0.226	0.012	
-9.2	0.233	0.012	

Table 3.6: The values of the waterside stresses for contaminated surface at 8.1 m s^{-1} wind speed; τ_{total}, the magnitude of total shear stress; τ_{wave} , the magnitude of wave stress; τ_{visc}, the magnitude of viscous stress.

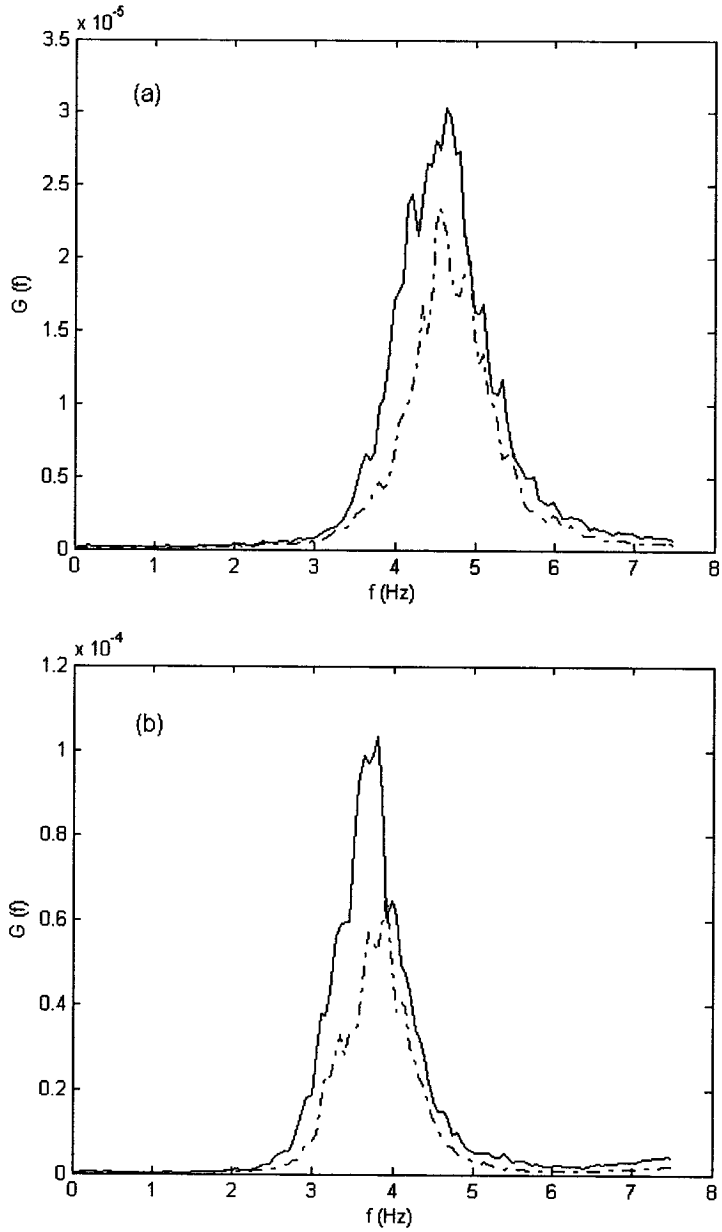

Figure 3.1 : Frequency spectra of the surface profile; (a), at 6.3 m s^{-1} wind speed; (b), at 8.1 m s^{-1} wind speed; solid line, clean surface; dash-dotted line, contaminated surface.

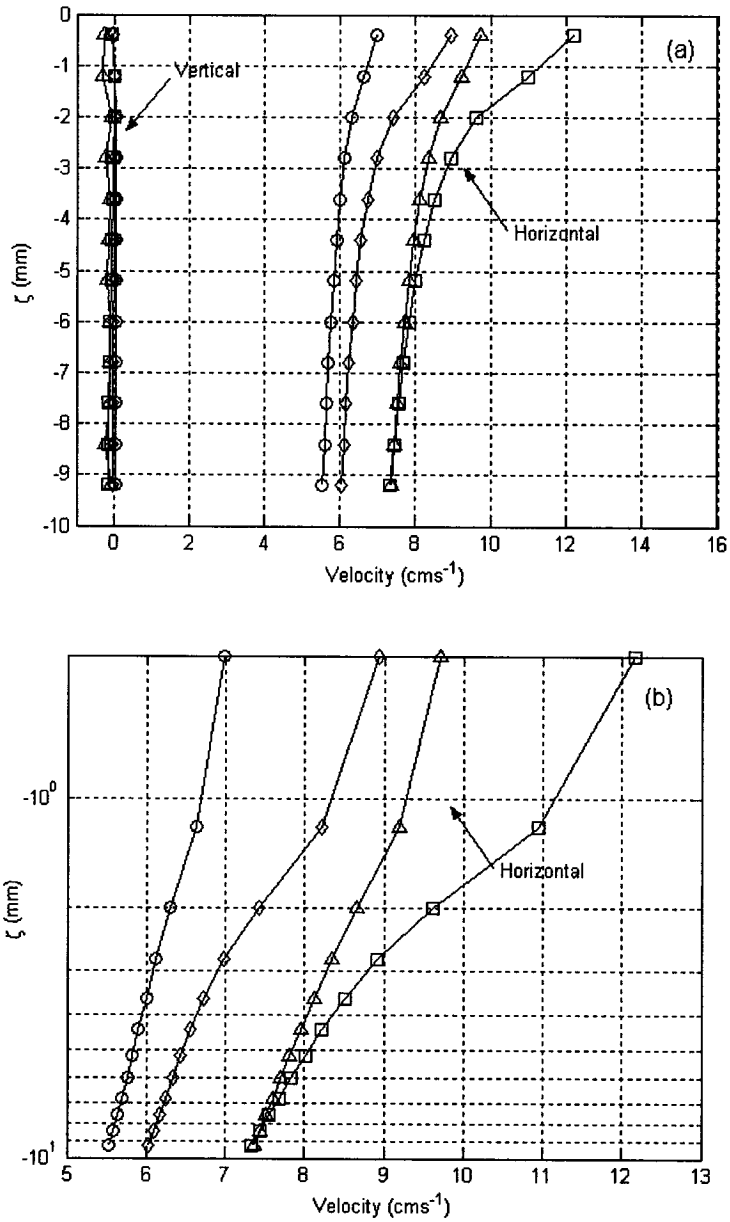

Figure 3.2: Vertical profiles of the streamwise and vertical components of the mean velocity (a) linear scale, (b) semi logarithmic scale: ○, = clean surface at 6.3 m s^{-1} wind speed; ◊, = contaminated surface at 6.3 m s^{-1} wind speed; Δ, = clean surface at 8.1 m s^{-1} wind speed; □, = contaminated surface at 8.1 m s^{-1} wind speed.

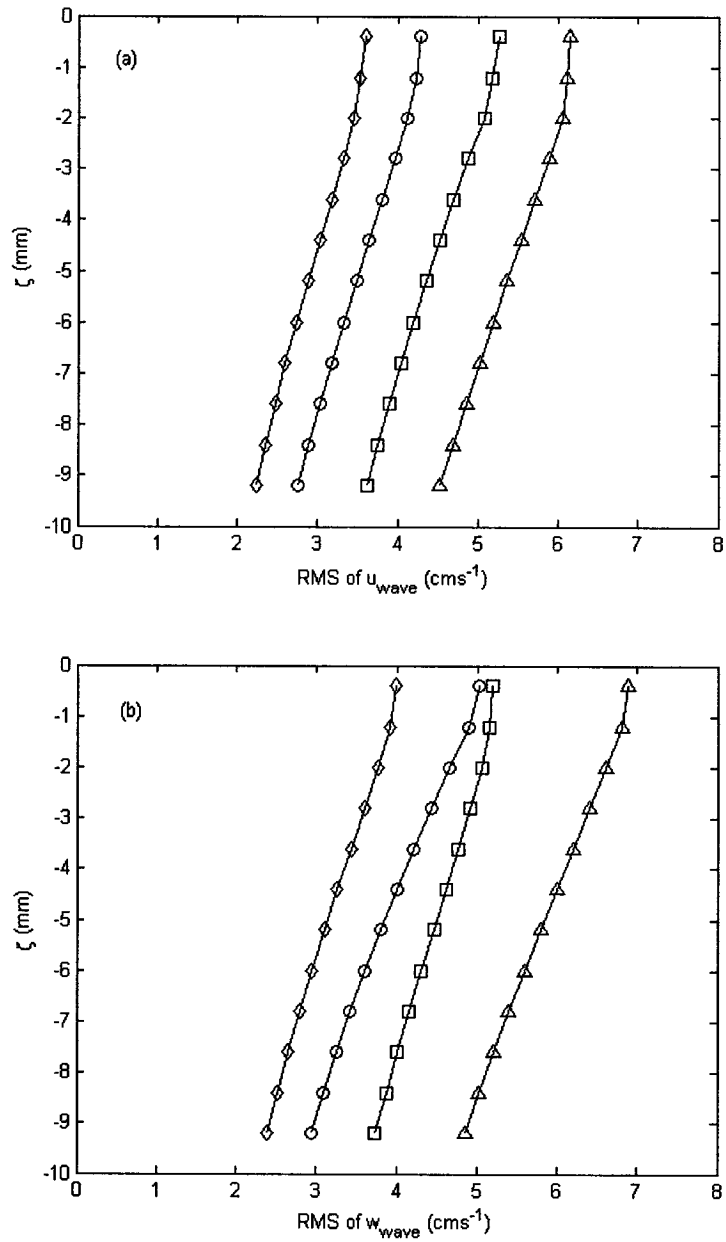

Figure 3.3: Vertical profiles of the RMS wave velocity components; (a), the streamwise component; (b), the vertical component; ○, = clean surface at 6.3 m s^{-1} wind speed; ◊, = contaminated surface at 6.3 m s^{-1} wind speed; Δ, = clean surface at 8.1 m s^{-1} wind speed; □, = contaminated surface at 8.1 m s^{-1} wind speed.

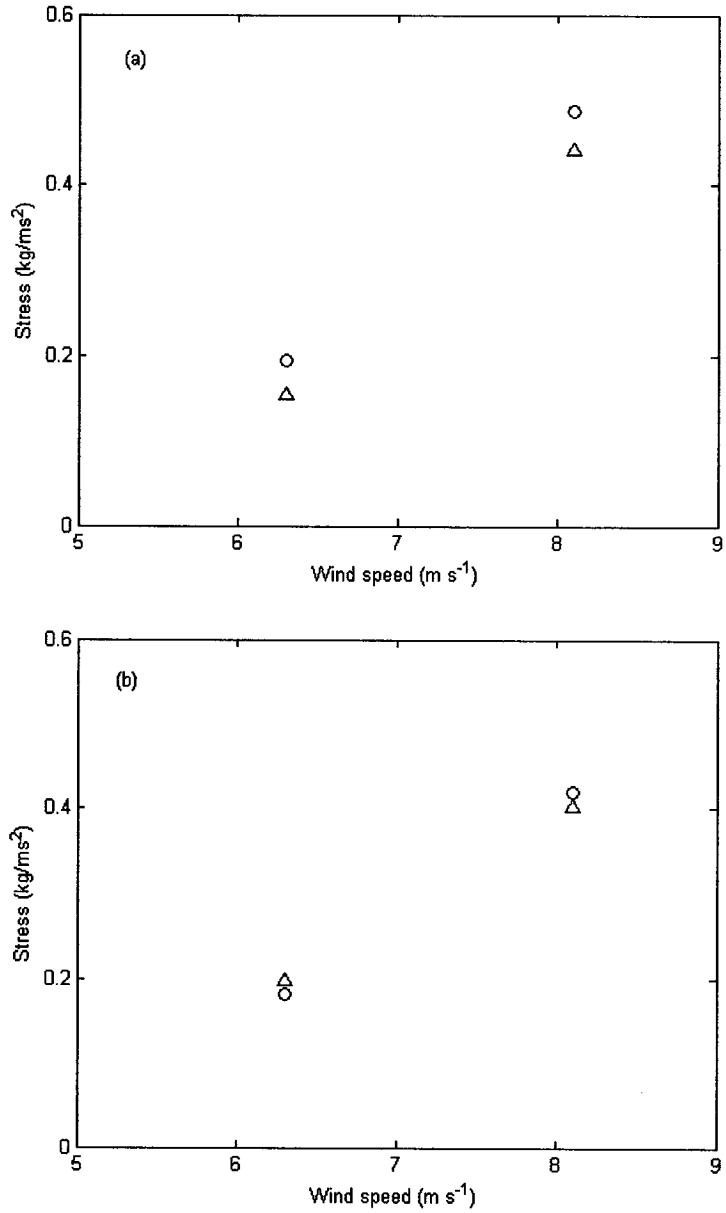

Figure 3.4: Comparison between the total waterside stress at a depth of 0.4 mm and the wind stress, at different wind speeds; (a), the clean surface; (b), the contaminated surface; Δ, = total waterside stress; ○, = wind stress.

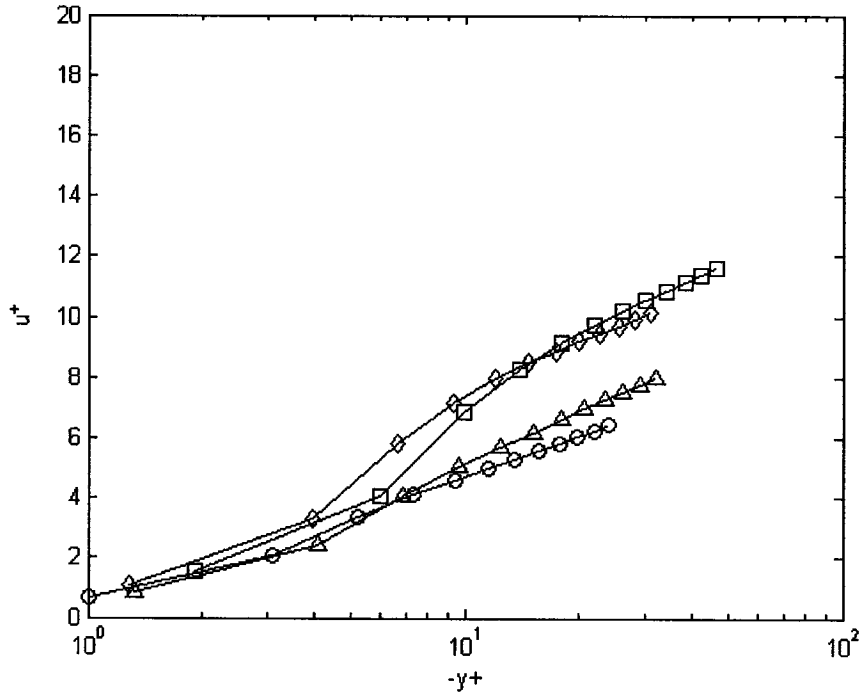

Figure 3.5: The mean streamwise velocity plotted in the form of a velocity defect law in wall coordinates; $u^+ = (U_s - U) / u_*$ and $y^+ = yu_* / \nu$. ○, = clean surface at 6.3 m s^{-1} wind speed; ◊, = contaminated surface at 6.3 m s^{-1} wind speed; Δ, = clean surface at 8.1 m s^{-1} wind speed; □, = contaminated surface at 8.1 m s^{-1} wind speed.

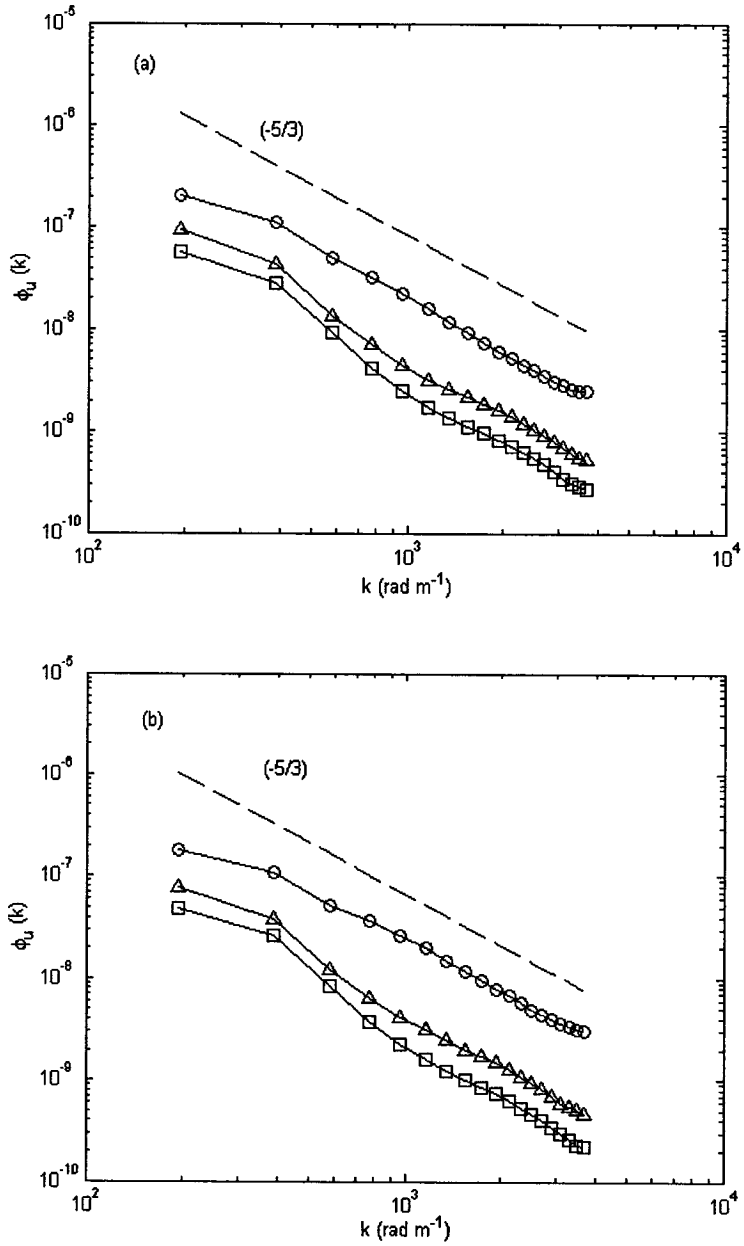

Figure 3.6: Wave number spectra of the streamwise instantaneous velocity *Φu(k)* at 6.3 m s^{-1} wind speed;(a), clean surface; (b), contaminated surface; ○, = 0.4 mm depth; Δ, = 4.4 mm depth; □, = 9.2 mm depth.

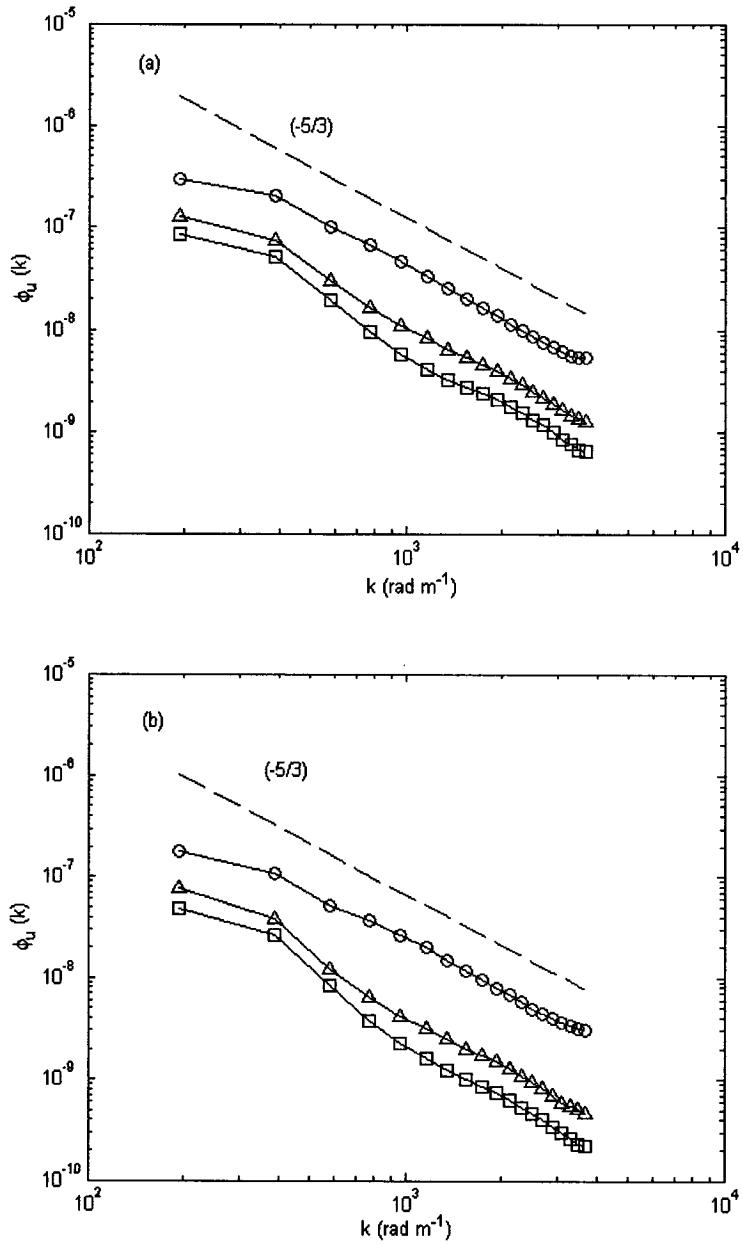

Figure 3.7: Wave number spectra of the streamwise instantaneous velocity *Φu(k)* at 8.1 m s^{-1}wind speed; (a), clean surface; (b), contaminated surface; ○, = 0.4 mm depth; Δ, = 4.4 mm depth; □, = 9.2 mm depth.

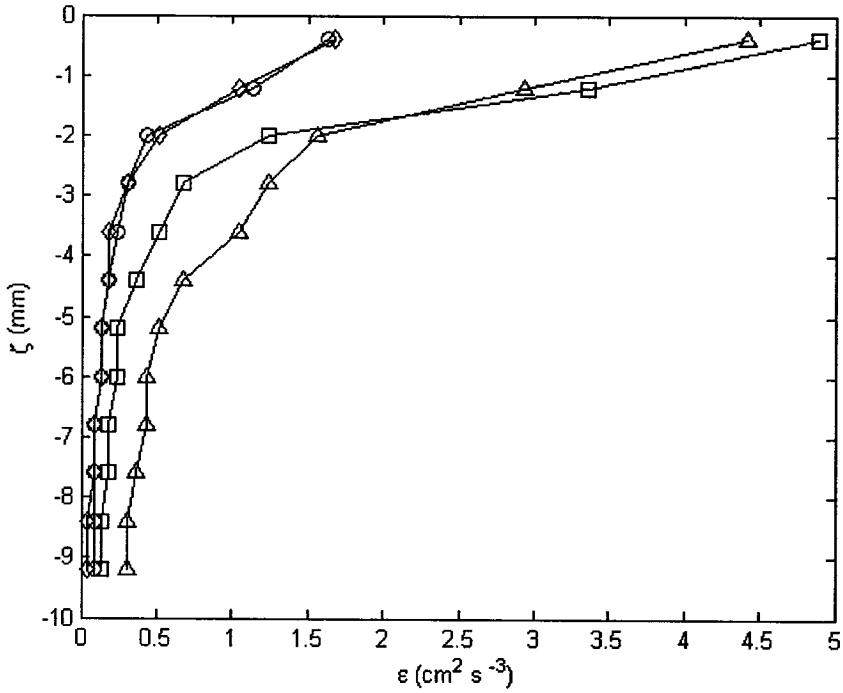

Figure 3.8: The vertical profiles of the rate of energy dissipation, ε. ○, = clean surface at 6.3 m s^{-1} wind speed; ◊, = contaminated surface at 6.3 m s^{-1} wind speed; Δ, = clean surface at 8.1 m s^{-1} wind speed; □, = contaminated surface at 8.1 m s^{-1} wind speed.

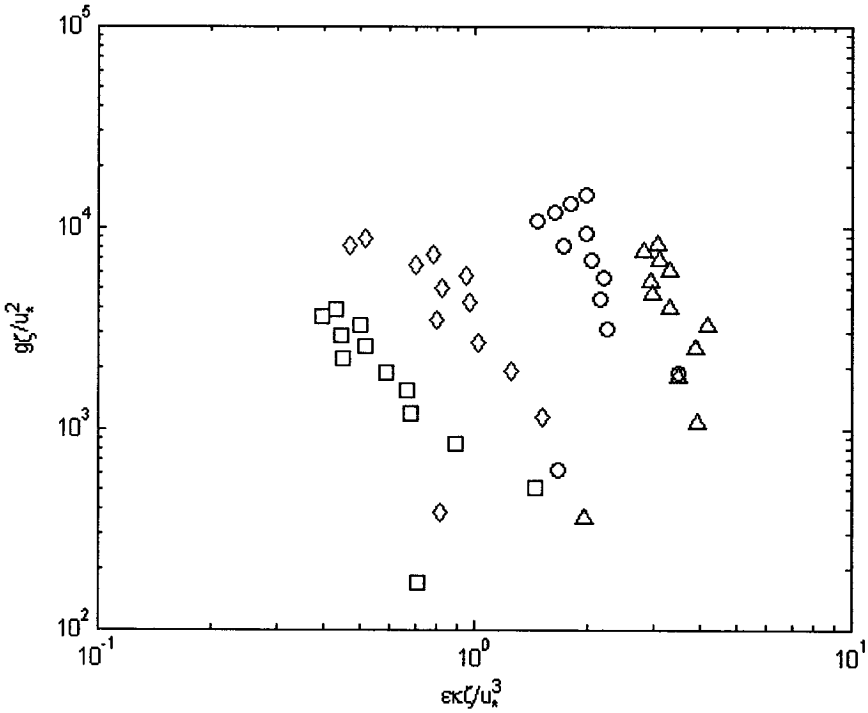

Figure 3.9: Plot of the rate of energy dissipation, ε, versus the depth, ζ, normalized in wall coordinates. ○, = clean surface at 6.3 m s^{-1} wind speed; ◊, = contaminated surface at 6.3 m s^{-1} wind speed; Δ, = clean surface at 8.1 m s^{-1} wind speed; □, = contaminated surface at 8.1 m s^{-1} wind speed.

CHAPTER 4

Parasitic Capillary Waves and Microscale Breaking Waves

4.1 Parasitic Capillary Waves

Parasitic capillary waves were observed along the downwind face of the gravity wave crests in the profile and DPIV datasets. A typical vorticity field beneath the crest of a gravity wave is shown in figure 4.1. Parasitic capillary waves are visible on the forward face of the wave crest. The regions of high vorticity beneath the wave crest are also prominent in the figure. A plausible explanation for the strong vorticity beneath the gravity wave crest is the vorticity shed by the capillary waves, as suggested by Longuet-Higgin (1992). The resolution of the velocity data was not high enough to directly investigate the vortex shedding process.

In order to investigate the characteristics of these parasitic capillary waves, we developed a scheme to detect and quantify capillary waves based on the visual inspection of the DPIV vorticity fields and the surface profiles. In this scheme, the DPIV vorticity field was plotted along with the surface profile (as shown in figure 4.1). The surface profile was used to detect parasitic capillary waves and to compute their wavelength and amplitude. The vorticity data was used to estimate the vorticity magnitude beneath each capillary wave. In any plot, where the parasitic capillary waves were observed, the mouse was used to click at the edges of each capillary wave in the surface profile to

record the coordinates. The linear distance between the edge coordinates of each capillary wave was then computed, which is equal to its wavelength. A similar method was used to compute the amplitude of each capillary wave. That is, the coordinates of the base and the uppermost point of each capillary wave were recorded using the mouse. The linear distance between these coordinates gave the approximate wave amplitude. Colormaps of the vorticity was used to estimate the average vorticity beneath each capillary wave. In addition, each DPIV field in which a gravity wave with parasitic capillary waves was observed, the frame number of that field and the number of parasitic capillary waves observed on the gravity wave were recorded. At each wind speed, 9000 plots were visually inspected (i.e. 4500 at each surface condition). At each wind speed and surface condition, all of the above-mentioned parameters were stored in a database. Thus, in total, 18,000 plots were visually inspected to compute the characteristics of the capillary waves.

To validate the visual-based scheme, the length of the parasitic capillary waves was computed from spectral analysis of the surface profile data. In the validation technique, the wavenumber spectra of the surface profiles were computed. The wavenumber spectra were computed only for those surface profiles in which a gravity wave with parasitic capillary wave was detected by visual inspection. The peaks in the spectra correspond to the capillary waves and their respective wavenumbers give the corresponding wavelengths. Figure 4.2 shows the wavenumber spectrum of a surface profile at a wind speed of 8.1 m s^{-1}. Three distinctive peaks at $2000 < k < 10000$ are visible in the spectrum that represent three parasitic capillary waves, and the corresponding wavenumbers give their wavelengths. Note that the length of the surface

profile was not long enough to resolve the peak of the gravity waves. The average wavelength of the capillary waves computed from the visual inspection and the wavenumber spectra of the surface profiles are plotted in figure 4.3 for all conditions. The plots show that the wavelength computed from both independent methods is within 10%. This indicates that the capillary wave characteristics computed from the visual inspection of the surface profiles is accurate. The vorticity beneath capillary waves was estimated from the colormaps in the DPIV vorticity fields by the visual inspection. It is difficult to quantify the error based on the visual inspection of the vorticity colormaps. As a conservative estimate, the uncertainty in the vorticity magnitudes beneath the capillary waves is up to 50%.

Different characteristics of capillary waves computed from the visual scheme are tabulated in table 4.1 for both wind speeds and both surface condition. The results indicate that the wavelength and amplitude of the parasitic capillary waves do not change significantly as a function of wind speed and surface condition. A slight decrease in the wavelength and a slight increase in the amplitude were observed as the wind speed increased from 6.3 to 8.1 m s^{-1} for both surface conditions. But, no definitive conclusion about these trends could be made. However, a clear trend was observed for the vorticity and number of capillary waves. The results show that for a given surface condition, the vorticity of capillary waves increases with wind speed. As the wind speed increased from 6.3 to 8.1 m s^{-1}, the average vorticity beneath the parasitic capillary waves increased by approximately 50% and 40%, for clean and contaminated surfaces, respectively. At a given wind speed, the average vorticity beneath capillary waves on a contaminated surface was slightly higher than that beneath the clean surface.

The effects of wind speed and surface condition on the number of gravity waves with parasitic capillary wave were also investigated. The number of gravity waves with capillary waves (N_{GC}) at both wind speeds and surface conditions are tabulated in table 4.1. The results show that the number of gravity waves with parasitic capillary waves increases with wind speed for both surface conditions, and at a given wind speed, this number decreases beneath contaminated surfaces. In the presence of a surfactant, the number of gravity waves with parasitic capillary waves decreased by 60% and 30% at the lower and higher wind speed, respectively.

The results in table 4.1 also show that the total number of parasitic capillary waves increases with wind speed for a given surface condition, and at a given wind speed, the number of capillary waves decreases in the presence of surfactant. As the wind speed increased from 6.3 to 8.1 m s^{-1}, the number of parasitic capillary waves increases by approximately 80% and 170% for clean and surfactant-contaminated surfaces, respectively. In the presence of a surfactant, the number of capillary waves reduced by 70% and 50% at 6.3 and 8.1 m s^{-1} wind speeds, respectively. The above result shows that the number of capillary waves is significantly reduced in the presence of surfactant.

The database of capillary wave characteristics was used to analyze the amplitude, length and vorticity variations among the capillary waves. The probability density functions (PDF's) of the amplitude and wavelength of capillary waves for both wind speeds and surface conditions are plotted in figures 4.4 and 4.5 (a & b), respectively. The PDF's of the wave amplitude show that there is a slight reduction in the amplitude of capillary waves due to the surfactant, which is consistent with the findings of Ceniceros

(2003). However, the PDF's of the wavelength show that at the lower wind speed, the lengths of the capillary waves did not change with the surface condition. Whereas, at the higher wind speed, the length of the capillary waves increased slightly in the presence of surfactant. This result is not in agreement with the simulation results of Ceniceros (2003). The probability density function of the number of capillary waves per gravity wave, $N_{c\text{-}g}$, is plotted in figure 4.6 (a & b) for 6.3 and 8.1 m s^{-1} wind speeds, respectively. The plots show that more capillary waves are observed on the crest of a gravity wave for a clean surface as compared to a surfactant-contaminated surface. Furthermore, as the wind speed increases, more parasitic capillary waves are observed on the crest of a gravity wave. As the wind speed increased from 6.3 to 8.1 m s^{-1}, $N_{c\text{-}g}$ on average, increased by approximately 45% and 30% beneath clean and surfactant-contaminated surfaces, respectively. In the presence of surfactant, $N_{c\text{-}g}$ decreased by 15% and 25% at the lower and higher wind speeds, respectively.

Zappa (1999) observed that the capillary waves appear on the forward face of the wave prior to the breaking process and that they disappear once the wave is broken. Duncan (2001) observed the breaking process of mechanically generated spilling breakers. He found a bulge-capillary wave system on the forward face of an incipient breaking wave. As the wave broke, he observed that the bulge moved down on the forward face and the ripples developed in the region between the leading edge of the breaker and the crest. The observations in these studies suggest that the appearance of parasitic capillary waves is important to the breaking process. In order to investigate the relation between parasitic capillary waves and microscale breaking waves, the next step

is to determine which waves are microscale breaking waves. In the next section, we will discuss the microscale breaking wave detection scheme.

4.2 Detection of Microscale Breaking Waves

As discussed in Chapter 1, low visual contrast due to the lack of air entrainment makes microscale breaking waves difficult to identify visually. Jessup et al. (1997) have shown that infrared imagery could be used to detect microscale breaking waves. Siddiqui and Loewen (2004) have developed a microscale breaking wave detection scheme based on the variance of vorticity beneath the wave crest computed from the DPIV velocity fields. They validated their DPIV based detection technique with the infrared imagery and argued that the vorticity-based detection scheme accurately detects microscale breaking waves.

The technique developed by Siddiqui and Loewen (2004) works well to detect microscale breaking waves beneath clean surfaces. However, it was not accurate for the two surfactant cases where the high near-surface mean velocity gradients (see figure 3.2), created a layer of enhanced vorticity, as shown in figure 4.10. The vortices generated by microscale breaking waves were superimposed on the strong background vorticity, i.e. the vorticity due to the mean shear. The magnitude of this background vorticity varied; therefore, a single vorticity threshold to detect microscale breaking waves did not produce accurate results. As a result, a vorticity-based microscale breaking wave detection scheme could not be used to detect microscale breaking wave generated beneath surfactant-contaminated surfaces. Thus, a new detection scheme was developed that would work accurately for both surface conditions.

In the present study, a technique was developed to detect microscale breaking wave crests based on the wake signature in the infrared images. In this technique, only those microscale breaking waves were considered that appeared at the location of the DPIV field of view in the infrared images. An IR image of the water surface temperature at a wind speed of 8.1 m s^{-1} is shown in figure 4.7 (a). A thermal wake generated due to the disruption of cool skin layer by a microscale breaking wave, is visible in the upper half of the image. The location of the DPIV field of view is delineated with a vertical line. A temperature threshold based on the mean and standard deviation of the temperature field within an IR image was used to detect the thermal wakes. That is,

$$T_{threshold} = \overline{T} + \sigma_T \tag{4.1}$$

where, $\overline{T}$ is the average temperature of the IR image and σ_T is the standard deviation of the image temperature. Once the wakes were detected, a series of morphological operations were performed to remove the noise from the segmented image. The thermal wake was detected by applying $T_{threshold}$, to the IR image in figure 4.7(a), and the corresponding segmented image is shown in figure 4.7 (b). Comparison of the images in figure 4.7 (a & b) demonstrates that the thresholding technique accurately detects the thermal wakes in the IR images that are produced by microscale breaking waves.

As mentioned earlier, this detection scheme was applied to detect microscale breaking waves that cross the DPIV field of view in the IR images. The profile data was used to detect a wave crest within the DPIV field of view. A wave crest is defined as any part of the wave that has surface displacement greater than one-quarters of the RMS wave amplitude. When a wave crest was detected in the DPIV field of view, the location of this wave crest was translated into the IR image (see the dash-dotted line in figure 4.7b).

The collocation images of the IR, DPIV and profile cameras were used to accurately translate the crest location in the IR image over the DPIV field of view location. Once the crest was located in the IR image, a region-of-interest (ROI) was defined with reference to the wave crest. Siddiqui et al. (2001) have shown that wakes are typically generated behind the forward face of the wave. In the upwind direction, the wakes typically extended to a length of the order of the wavelength. The length of the ROI in the streamwise direction was set equal to three-fourths of the dominant wavelength. That is, a quarter of the wavelength downwind of the crest and half of the wavelength upwind of the crest. Visual analysis of the simultaneous IR images and DPIV vorticity fields showed that when a wake appears above the DPIV field of view in the IR images, strong vortices are observed in the near-surface region in the DPIV vorticity field. This analysis also indicated that when a wake does not occupy the DPIV field of view in the IR image, but passes very close to it, strong vortices are still observed in the DPIV vorticity field, indicating that it is still an active breaking wave. Thus, in order to consider the wakes that passes close to the DPIV field of view, the width of the ROI (i.e. the dimension in the cross wind direction) was set equal to 50 pixels, that is, 25 pixels on each side of the line representing the DPIV field of view in the IR image. The ROI along with the crest location for a wave that appears within the DPIV field of view in an IR image is also shown in figure 4.7 (b) with the dashed line.

A wave crest that appeared within the DPIV field of view would typically appear in two to four IR images, depending on the wind speed. For each IR image in which a wave crest appeared in the DPIV field of view, the fraction of the ROI occupied by the wake, F_w, was recorded. A threshold, F_t, was set based on the fraction of the ROI

occupied by the wake, to detect microscale breaking waves. For a given wave, if $F_w > F_t$ for any crest that belongs to the same wave, then that wave was identified as a microscale breaking wave, and all the crests corresponding to this wave were considered as breaking wave crests.

In order to set the value of this threshold, microscale breaking waves were identified independently from the DPIV vorticity fields. For this purpose, 700 DPIV vorticity fields at a wind speed of 8.1 m s^{-1}, beneath a clean surface were visually inspected. The wave crests with strong vortices were identified as the crests of microscale breaking waves (Siddiqui et al. 2001). The frame numbers of all the crests that belong to the same breaking wave were recorded. The microscale breaking waves were then detected using the IR-wake method described above, for different values of F_t. The values of F_t varied from 0.2 to 0.5. The frames that were detected as microscale breaking wave crests, from the DPIV vorticity fields, were then compared with the frames that were detected as microscale breaking wave crests from the IR-wake method for different values of F_t. The results are tabulated in table 4.2. The results show that the percentage of breaking waves detected commonly by both methods is the highest for $F_t = 0.2$. This percentage decreases with increasing the threshold. The data shows that although the percentage of commonly detected breaking waves is highest at $F_t = 0.2$, but at this threshold, the IR-wake method detects relatively large number of non-breaking waves as microscale breaking waves. Whereas, at higher values of F_t, the IR-wake method considers a significant number of microscale breaking waves as non-breaking waves. The difference between the number of microscale breaking waves detected from DPIV technique with the number of microscale breaking waves detected by IR method using

$Ft = 0.3$ and 0.4 is approximately the same for both thresholds (16-17), but the percentage of commonly detected microscale breaking wave from two methods is higher at $F_t = 0.3$. Based on these results, the value of F_t was set equal to 0.3. That is, if 30% of the ROI in any IR image was occupied by a wake, then that wave was identified as a microscale breaking wave.

The detection scheme was then applied to both wind speeds and both surface conditions. The percentages of microscale breaking waves are tabulated in table 4.3. The results show that the percentage of breaking waves is significantly reduced in the presence of surfactant. This percentage is reduced by approximately 50% at both wind speeds. The table also shows that for a given surface condition, the percentage of breaking waves does not change significantly as the wind speed increased from 6.3 to 8.1 m s^{-1}. Siddiqui and Loewen (2004) reported the percentage of microscale breaking waves as 47% and 80% at wind speeds of 6.1 and 8.5 m s^{-1} at a fetch of 5.5 m. Banner and Peirson (1998) found that at a fetch of 4.35 m, the percentage of microscale breaking waves was 70% and 89% at 6.3 and 8.1 m s^{-1}.

4.3 Parasitic Capillary Waves and Microscale Breaking Waves

The datasets of the detected parasitic capillary waves and microscale breaking waves enabled us to investigate whether any relation exists between the occurrence of the parasitic capillary waves and microscale breaking waves. Separate time series of the frame numbers were generated for capillary and breaking waves at each wind speed and surface condition. In each time series for the capillary waves, 1's were assigned to the frame numbers that have detected parasitic capillary waves along the gravity wave crests.

For microscale breaking waves, 1's were assigned to the frame numbers that have the breaking wave crests. The frame numbers of the detected microscale breaking waves were then compared with the frame numbers of the detected capillary waves, for both wind speeds and surface conditions. This process is shown graphically in figure 4.8 for a time series of 100 frames at a wind speed of 8.1 m s^{-1} beneath clean surface. The solid line represents the time series of breaking wave crests and the asterisks represent the time series of wave crests with parasitic capillary waves. The plot shows that in most cases, the parasitic capillary waves appeared at the beginning of the breaking process. The analysis of the results for all cases show that for the clean surface, 91% and 95% of the capillary waves appeared on the incipient breaking crests at the lower and higher wind speeds, respectively. In the presence of surfactant, the percentage reduced to 75% at both wind speeds.

The above results show that the parasitic capillary waves that ride on the gravity wave crests are related to the wave breaking process. Philips (1981) argued that in a frame of reference moving with the phase velocity of the long wave, due to the relatively small phase velocity, the downwind train of capillary waves propagates towards the long wave. When the wave train reaches the long wave crest, it gets blocked and cannot pass the long waves crest. Based on this argument, we propose this conceptual model of the incipient breaking process. As a gravity wave approaches a train of capillary waves, the speed of the downwind edge of the wave crest (i.e. the crest toe) reduces due to its interaction with the capillary wave train. As a result, the fluid at the crest accelerates and forward face of the crest becomes steeper, i.e. a bulge is formed. As the forward face becomes steeper, the bulge becomes unstable and slides down the toe, resulting in the

breaking of the wave. As the bulge slides down the toe, it overtakes the capillary waves, which then appear beneath the wave crest. This could be the reason why Zappa (1999) observed the disappearance of capillary waves just after the breaking process. According to this conceptual model, the capillary waves initiate the breaking process.

The above results also indicate that in the presence of surfactant, 25% of the wave crests with capillary waves were unbroken. One plausible explanation is that these waves could be at the near-breaking stage and they broke downwind of the DPIV field of view and therefore, remained undetected. Beneath the clean surface, less than 10% of the wave crests with capillary waves were unbroken in the DPIV field of view. Thus, it can be argued that the initialization of the breaking process by capillary waves is relatively fast beneath the clean surface as compared to the surfactant-contaminated surface.

4.4 Dynamics of Coherent Structures

A coherent structure or vortex is defined as a connected, large-scale turbulent fluid parcel with a phase-correlated vorticity over its spatial extent. It is a characteristic feature of turbulent shear flows and is responsible for the large-scale transport of mass, heat and momentum (Hussain 1983). Previous studies have shown that strong near-surface coherent structures are generated beneath microscale breaking waves and these structures are responsible for the enhancement of air-water gas and heat transfer rates (Siddiqui et al. 2001, 2004). The present dataset provides quantitative information about the near surface vorticity beneath clean and surfactant-contaminated surfaces and also about coherent structure.

Sequences of vorticity fields at a wind speed of 8.1 $m\,s^{-1}$ beneath clean and surfactant-contaminated surfaces are plotted in figure 4.9 and 4.10, respectively. In figure 4.9, a microscale breaking wave propagating on a clean water surface is shown. Strong coherent structures are clearly visible in the crest region of the breaker. In figure 4.9(a), the coherent structures appear immediately upwind of the leading edge of the breaker and they extend upwind to the edge of the image. In figure 4.9(b), the leading edge of the breaker has moved out of the field of view and a large number of coherent structures are still visible beneath the windward face of the breaker. Note that these coherent structures are comprised of vortices with positive or negative vorticity. The appearance of these counter-rotating coherent structures is always associated with microscale wave breaking. The trough of the wave has propagated into the field of view in figure 4.9(c) and the trailing edge of the wake associated with the coherent structures is now visible.

In figure 4.10, the vorticity fields beneath a microscale breaking wave in the presence of surfactant are presented. It is evident that the characteristics of the near-surface vorticity are dramatically different from those observed beneath a clean water surface. In the presence of surfactant, the layer of enhanced vorticity is 1-2 mm thick and is observed immediately below the surface. The figure also shows that this layer is comprised of counterclockwise or positive vorticity only. This thin layer of counterclockwise vorticity coincides with the region where the mean velocity gradients are significantly larger beneath the surfactant-contaminated surface compared to a clean surface (see figure3.2). This layer of high vorticity was observed in most of the vorticity plots beneath surfactant-contaminated surfaces.

The above sequence indicates that in the presence of surfactant, the near-surface vorticity is dominated by the shear associated with the mean velocity gradients. A wave crest appears in figure 4.10(b) and the windward face of the same wave is visible in figure 4.10(c). In the crest region, the magnitude of vorticity is significantly enhanced indicating that this wave is also a microscale breaking wave. Beneath a surfactant-contaminated surface this enhancement of vorticity in the crest region is due to the superposition of strong counterclockwise mean shear and the coherent structures generated by microscale breaking waves.

To quantify the impact of surfactant on the near-surface vorticity, the average values of the instantaneous vorticity computed within the top 3 mm layer of water, are presented in table 4.4. The results show that the average vorticity increases with wind speed. It increased by 50-60% as the wind speed increased from 6.3 to 8.1 m s^{-1}, for both surface conditions. The results also indicate that in the presence of surfactant, the average vorticity increased by a factor of more than two at both wind speeds. The positive values of the average vorticity imply that the counterclockwise vorticity is dominant in all cases. This could be beacuse the vorticity generated by the mean velocity gradients is also in the counterclockwise direction. In the presence of surfactant, the larger magnitude of counterclockwise vorticity is due to larger mean velocity gradients.

4.5 Discussion and Conclusion

The results in table 4.1 indicate that the number of capillary waves reduces significantly in the presence of surfactant. This reduction is due to the fact that the surfactant damps the capillary waves by creating interfacial tension gradient (Lucassen-

Renders et al 1969). Our results are consistent with Zappa (1999) who observed a significant reduction in the number of capillary waves in the presence of a surfactant. However, he did not quantify the statistics of the capillary waves. Bock et al. (1999) also observed a significant reduction in the capillary waves in the presence of surfactant. Based on a numerical investigation, Ceniceros (2003) argued that the surface-active agent diminishes the amplitude, and wavelength of capillary ripples.

The results presented in section 4.3 show that most of the capillary waves appear on the incipient breaking wave crests. According to the conceptual model discussed in section 4.3, if capillary waves trigger the breaking process, then the number of capillary waves should have a direct impact on the number of microscale breaking waves. The results in table 4.3 show that the percentage of breaking waves reduced by approximately 50% in the presence of surfactant. The results in table 4.1 show that in the presence of surfactant, the number of capillary waves also reduced by 50-70%. That is, when fewer numbers of capillary waves are available to initiate the breaking process, the number of breaking waves is reduced. Thus, we can conclude that the reduction in the percentage of microscale breaking waves beneath the surfactant-contaminated surfaces is due to the damping of the capillary waves by the surfactant.

Moreover, previous studies (Banner and Peirson, 1998 & Siddiqui and Loewen, 2004) have shown that the percentage of microscale breaking waves increases with wind speed, which is in agreement with the conceptual model discussed above. This is because the number of capillary waves increases with wind speed at a given surface condition, as a result the number of breaking waves also increase. The percentage of microscale breaking waves detected at 8.1 m s^{-1} wind speed is comparable with the above-mentioned

studies. However, at the lower wind speed, the percentage of detected microscale breaking waves is significantly high as compared to these previous studies. The results in table 4.1 show that there are less number of capillary waves at the lower wind speed; therefore, the percentage of microscale breaking waves is expected to be low. We have spent a significant amount of time to investigate the cause of this overestimation by the detection scheme at the lower wind speed, but the cause is unknown and is still under investigation.

Previous studies have also observed a reduction in the air-water gas transfer velocity in the presence of surfactant. Bock et al. (1999) observed up to 60% reduction in the transfer velocity for wind speeds in the range from 3.5 to 7.5 m s^{-1}. Zappa (1999) also observed a reduction in the gas and heat transfer velocities in the presence of surfactant. Since microscale breaking waves enhance air-water gas and heat transfer rates, one plausible explanation for the reduction of air-water gas transfer velocity could be the significant reduction in the percentage of breaking waves caused by the presence of the surfactant.

U_∞ (m s^{-1})	6.3		8.1	
Run type	Clean	Contaminated	Clean	Contaminated
λ (mm)	3.04	3.18	2.68	3.09
a (cm)	0.35	0.30	0.39	0.34
ω (s^{-1})	11.74	12.88	17.24	18.23
N_{GC}	187	75	230	155
N_C	919	309	1636	823
Nc-g	4.9	4.1	7.1	5.3

Table 4.1: U_∞, wind speed; λ, wavelength of capillary waves; a, amplitude of capillary waves; ω, absolute vortices beneath capillary waves; N_{GC}, number of gravity waves with capillary waves; N_C, number of capillary waves; *Nc-g*, average number of capillary waves per gravity wave.

F_t	0.2	0.3	0.4	0.5
N_{DPIV}	402	402	402	402
N_{IR}	453	418	385	327
N_{CM}	372	348	324	275
$\%C_{bw} = \frac{N_{CM}}{N_{DPIV}}$	93	87	81	68

Table 4.2: F_t; threshold for the fraction of the ROI occupied by the wake; N_{DPIV}, number of breaking waves detected from DPIV vorticity fields; N_{IR}, number of breaking waves detected from IR images; N_{CM}, number of breaking waves detected commonly by both methods; C_{bw}, percentage of commonly detected breaking waves.

U_∞ (m s^{-1})	6.3		8.1	
Run type	Clean	Contaminated	Clean	Contaminated
P_{bw}	87%	45%	86%	48%

Table 4.3: U_∞, the wind speed; P_{bw}, percentage of microscale breaking waves.

U_∞ (m s^{-1})	6.3		8.1	
Run type	Clean	Contaminated	Clean	Contaminated
$\overline{\omega}$ (s^{-1})	3.8	8.4	5.73	13.9

Table 4.4: U_∞, wind speed; $\overline{\omega}$, average of vorticity.

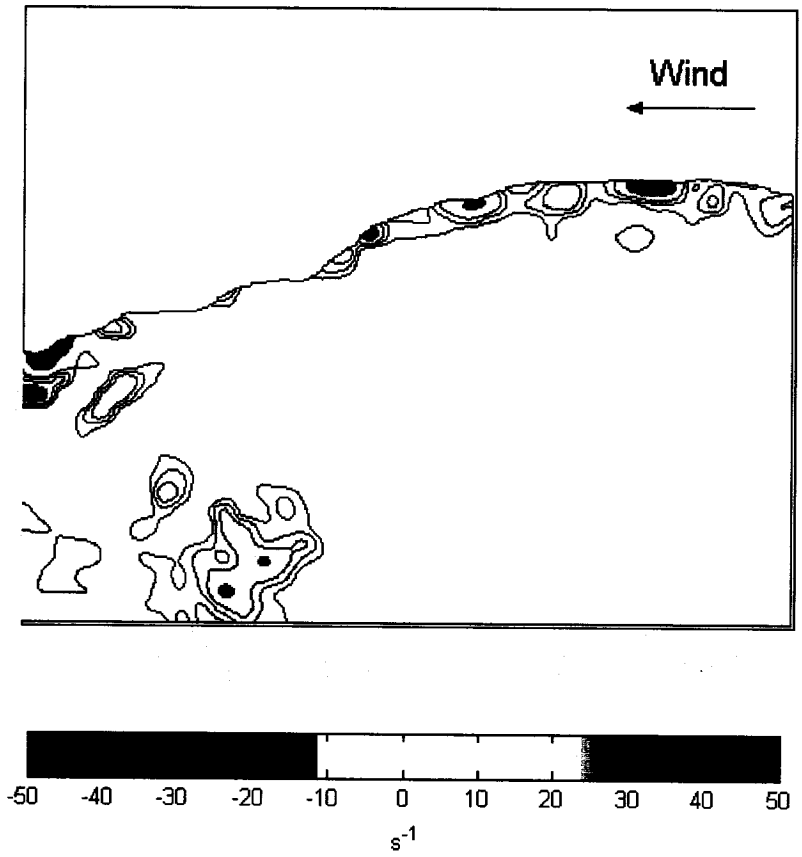

Figure 4.1: Vorticity fields of a gravity wave at a wind speed 8.1 m s^{-1} beneath clean surface. Capillary waves on the forward face of the gravity waves are clearly visible in the plot.

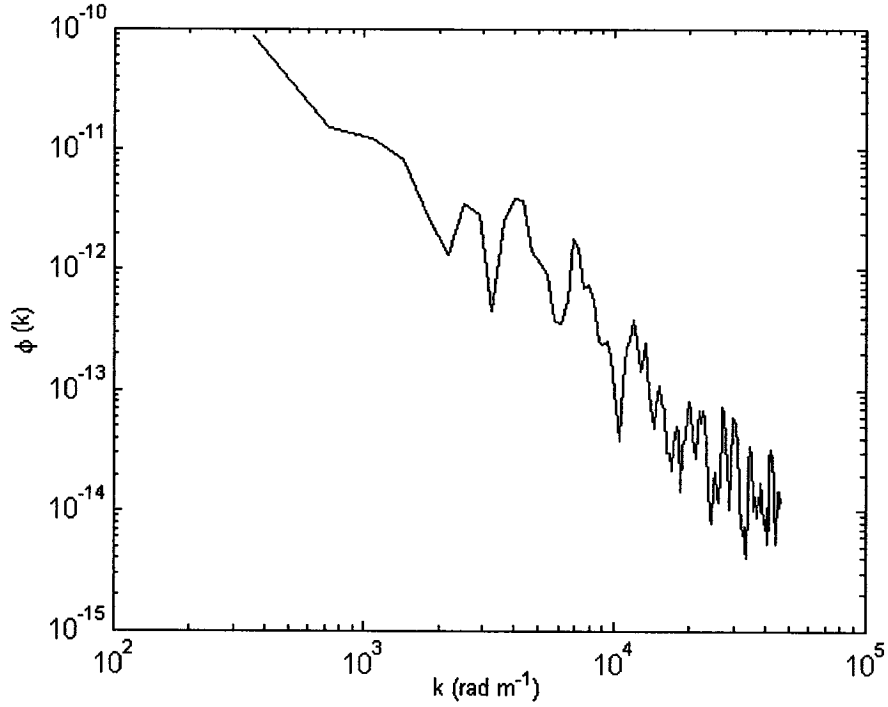

Figure 4.2: Wave number spectrum of surface displacement at a wind speed 8.1 m s^{-1} for the clean surface. The peaks in the spectrum in the range $2000 < k < 10000$ correspond to the capillary waves.

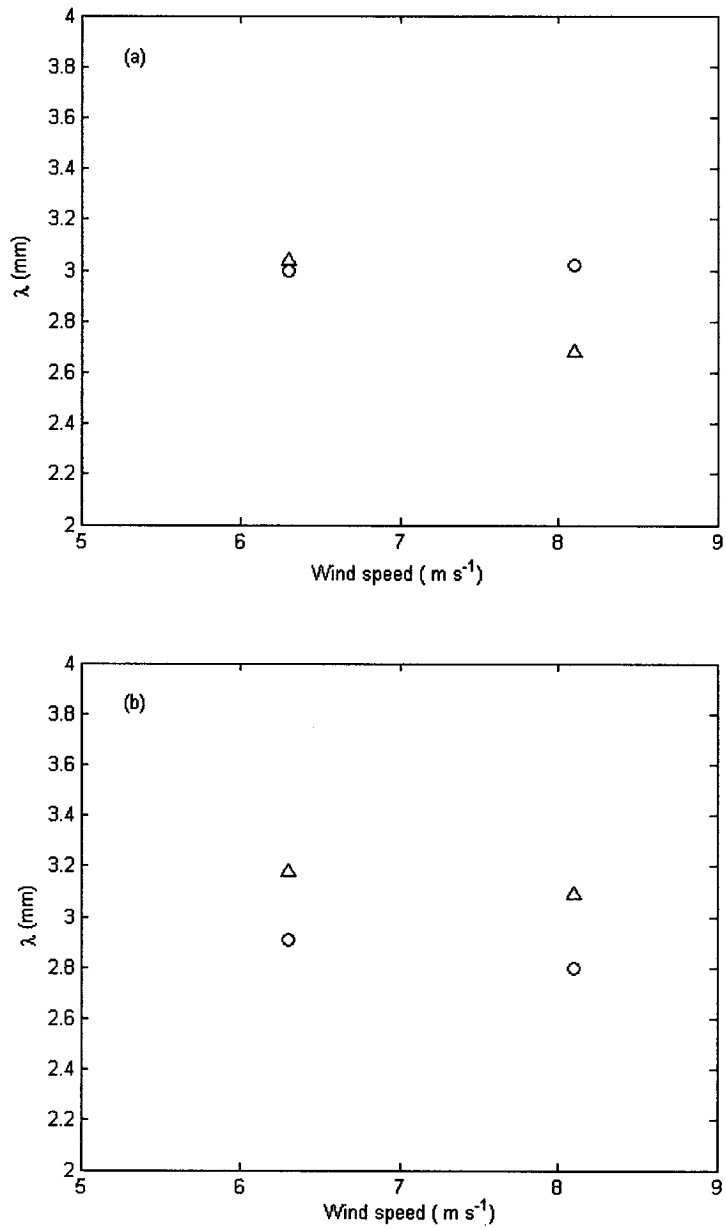

Figure 4.3: Wavelength of capillary waves on the forward face of gravity waves versus wind speed;(a), clean surface; (b), contaminated surface; ○, = from the wave number spectra of the surface profile; Δ, = from the visual inspection.

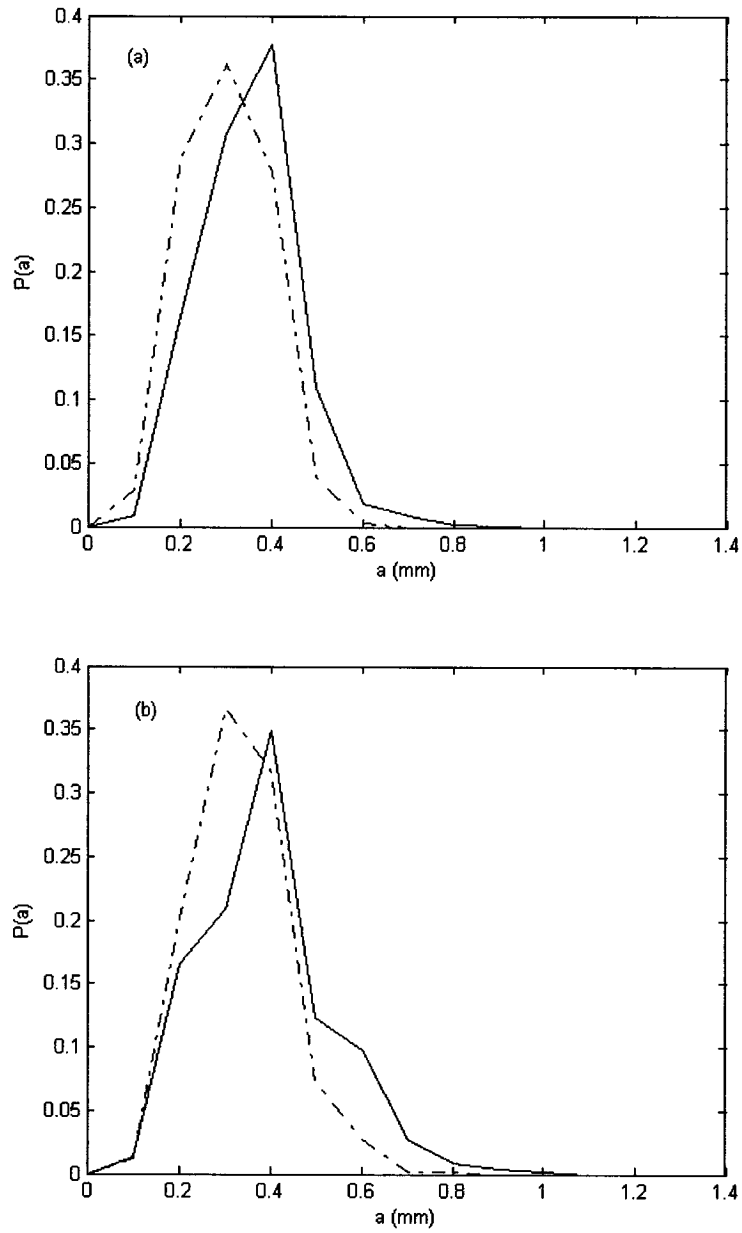

Figure 4.4: Probability density function of the capillary wave amplitude;(a), at 6.3 m s^{-1} wind speed; (b), at 8.1 m s^{-1} wind speed; solid line, clean surface; dash-dotted line, contaminated surface.

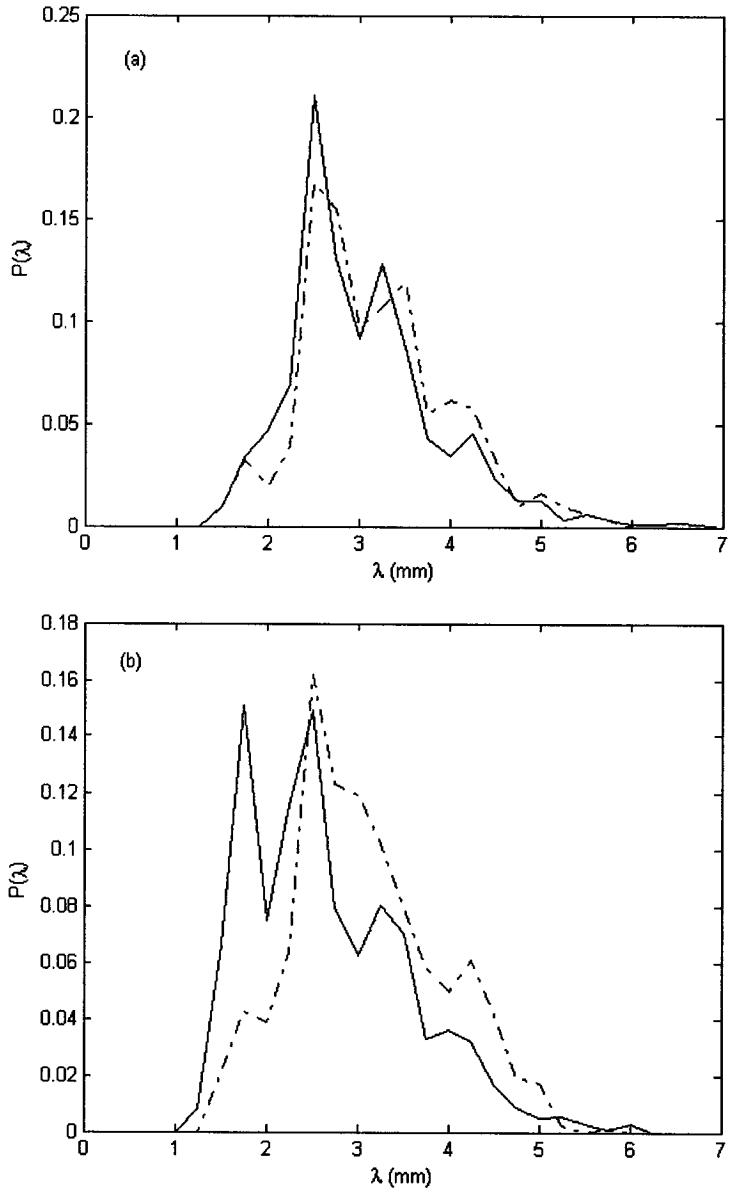

Figure 4.5: Probability density function of the capillary wavelength;(a), at 6.3 m s^{-1} wind speed; (b), at 8.1 m s^{-1} wind speed; solid line, clean surface; dash-dotted line, contaminated surface.

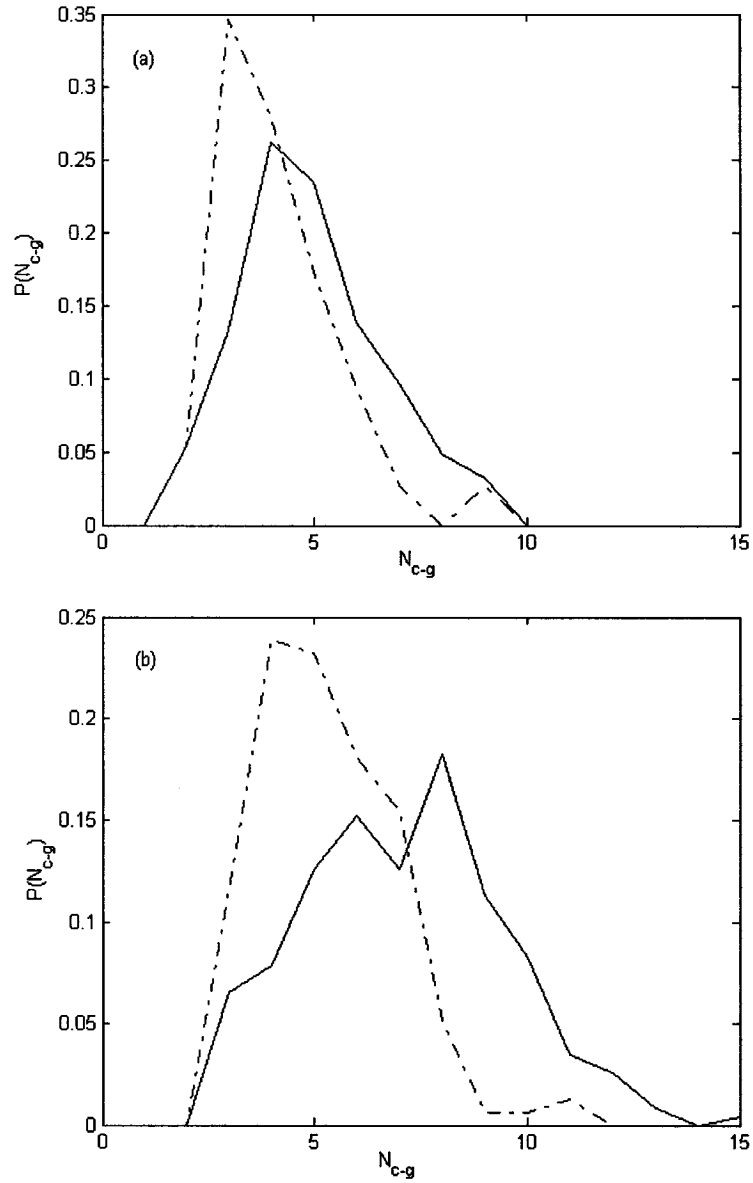

Figure 4.6: Probability density function of N_{c-g}, number of capillary waves per gravity wave; (a), at 6.3 m s^{-1} wind speed; (b), at 8.1 m s^{-1} wind speed; solid line, clean surface; dash-dotted line, contaminated surface.

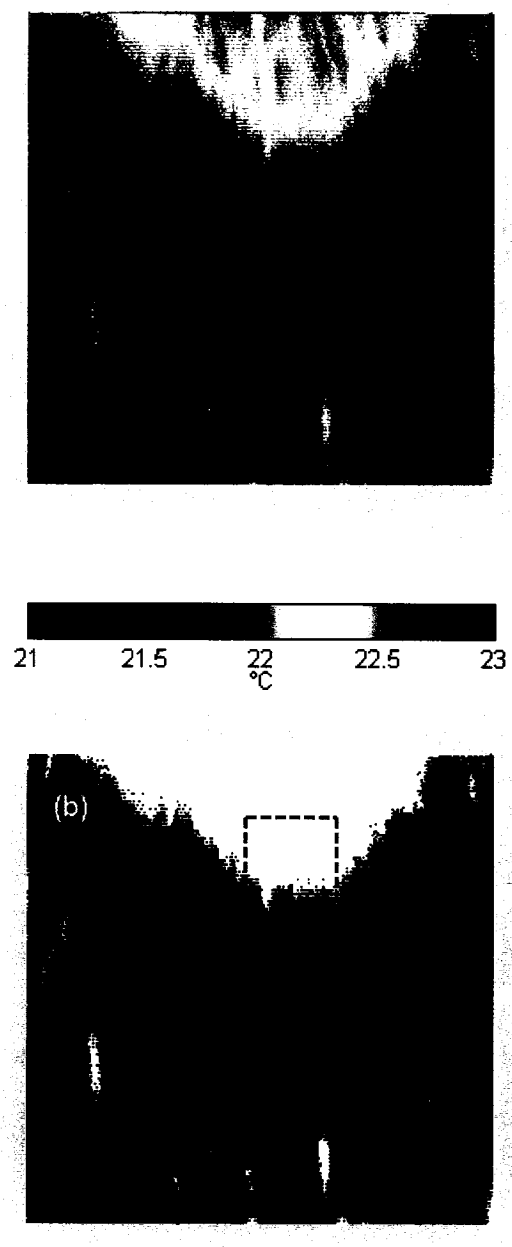

Figure 4.7: (a), An IR image of the water surface temperature at 8.1 m s^{-1} wind speed. The vertical line is the location of DPIV field of view in the IR images; (b), the segmented IR image after applying the temperature threshold; dash-dotted line, the crest position; dashed line, the region of interest (ROI); solid line, the location of the DPIV camera.

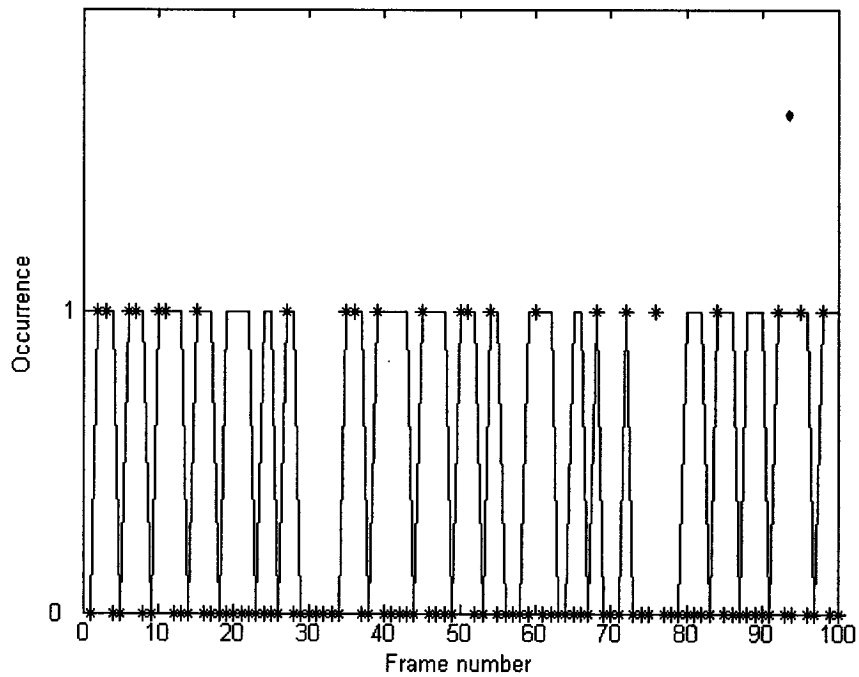

Figure 4.8: The comparison of the time series of parasitic capillary waves and microscale breaking waves at a wind speed of 8.1 m s^{-1} for clean surface; *, time series for parasitic capillary waves; solid line, time series for microscale breaking wave crests.

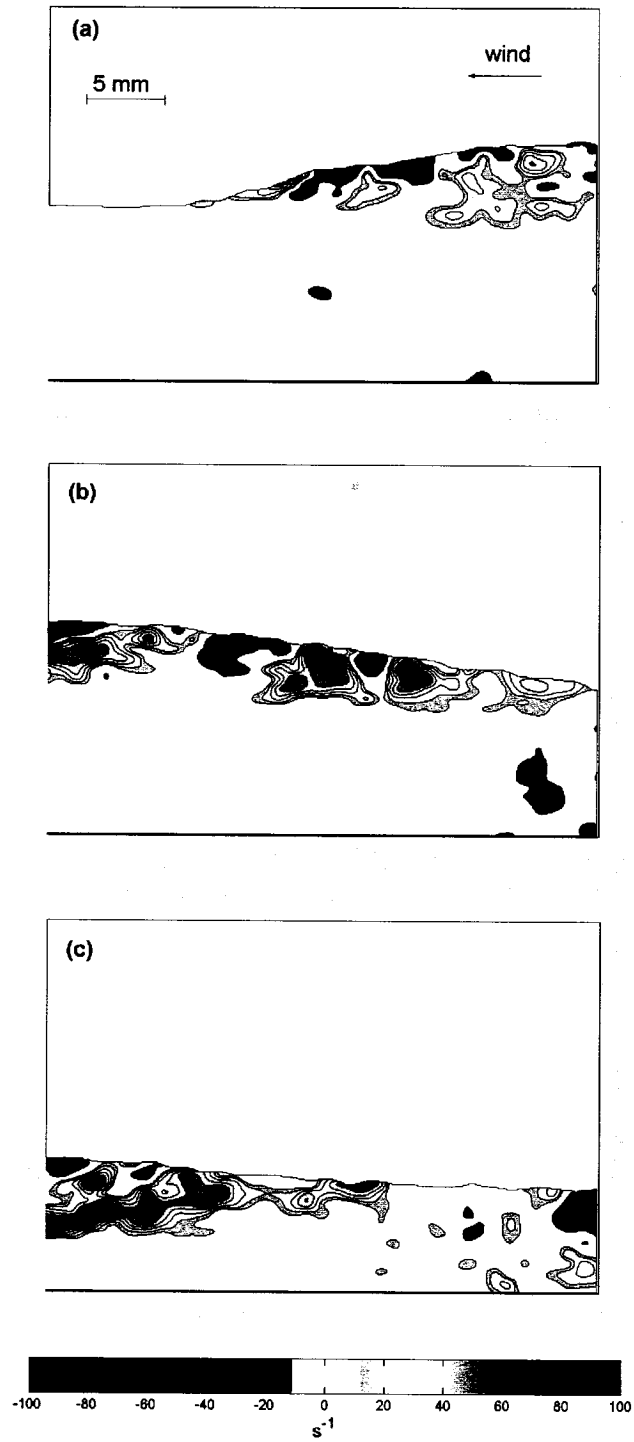

Figure 4.9: A Sequence of DPIV vorticity fields at a wind speed of 8.1 m s^{-1} beneath clean surface.

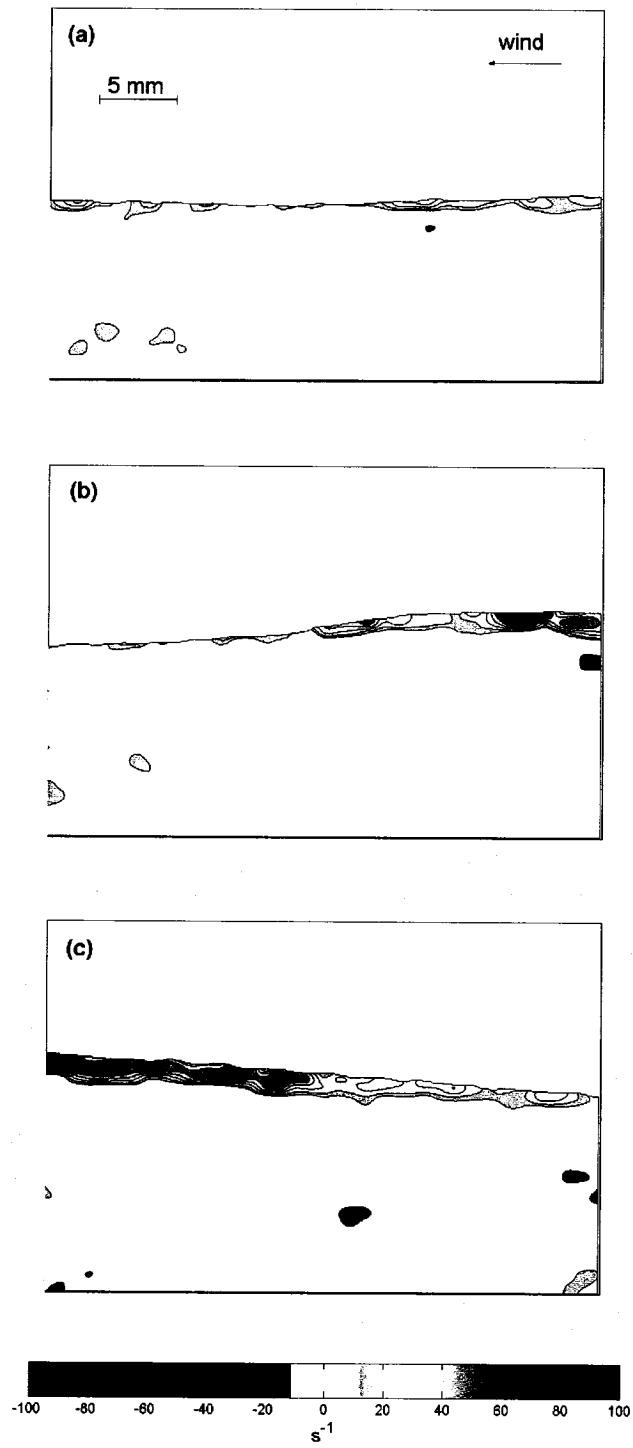

Figure 4.10: A sequence of DPIV vorticity fields at a wind speed of 8.1 m s^{-1} beneath contaminated surface.

CHAPTER 5

Summary and Suggestions for the Future Work

5.1 Summary

Most of the laboratory studies beneath short gravity wind waves and microscale breaking waves have been conducted for the clean water surfaces (e.g. Wu 1975; Cheung and Street 1988; Thais and Magnaudet 1996; Siddiqui et al. 2001; Peirson and Banner 2003). However, in oceans and lakes, biological organisms and other chemical species cover the water surface and alter the air-sea boundary conditions. It has been speculated that most of these short gravity waves are microscale breaking waves, which play a significant role in the air-sea gas and heat transfer. The focus of the presented study is to investigate the influence of surface contamination on the near-surface flow beneath short gravity waves and to explore the characteristics of parasitic capillary waves and their relation with microscale breaking waves

This thesis has reported on a series of laboratory experiments to investigate the near-surface flow field beneath clean and contaminated wind driven water surfaces. Measurements were conducted at a fetch of 5.5 m at wind speeds of 6.3 and 8.1 m s^{-1}. Triton-100 with the concentration of 1 p.p.m., was used as the surfactant. The two-dimensional velocity filed was measured using DPIV, and the surface temperature measurements were made simultaneously, using IR imagery. The results presented in this thesis are unique because they provide the first insight into the structure of the near-surface flow beneath surfactant-contaminated wind-driven surfaces. These data also

provided the first detailed analysis of the parasitic capillary waves for clean and contaminated surfaces. In addition, the relation between the parasitic capillary waves and incipient microscale breaking waves has been investigated.

The experimental setup and the measurement methods were described in Chapter 2. The procedure for the computation of the surface profile and the two-dimensional velocity fields are discussed in detail. The surface wave profiles were also used to compute the properties of the dominant gravity waves and the parasitic capillary waves.

In Chapter 3, different flow properties computed in the near-surface region beneath wind waves are presented and discussed. These properties include, the mean and wave velocity components, the total waterside shear stress, the viscous stress, the wave stress, and the waterside friction velocity. The one-dimensional wavenumber spectra of the streamwise velocity and the magnitudes of the rate of energy dissipation beneath wind waves were also presented and discussed. These results revealed that the RMS wave height was reduced by 19% to 24% in the presence of surfactant. Consequently, the wave energy was reduced by approximately 40% to 60% since it is correlated with the amplitude square of the wave.

The mean streamwise velocity profiles show the existence of the viscous sublayer where the mean velocity varies linearly with depth. The mean streamwise velocity gradients within the viscous sublayer were a factor of 2 to 2.3 larger beneath the surfactant-contaminated surface as compared to the clean surface. These higher mean velocity gradients beneath the contaminated surface are attributed to the change in the

hydrodynamic boundary conditions at the water surface due to surfactant. The mean velocity profiles are logarithmic outside the viscous sublayer.

The manifestation of the inertial subrange in the wavenumber spectra at a depth of 0.4 mm indicates that the turbulence is not zero within the viscous sublayer. The comparison of the total waterside stress computed at a depth of 0.4 mm with the wind stress shows that except for the clean case at 6.3 m s^{-1} wind speed, the values of the total stress and the wind stress are with in 10%. Thus, the total waterside stress computed at a depth of 0.4 mm represents the total stress transferred to the water from the wind.

The vertical profiles of the energy dissipation (ε) show that the ε increased near the surface by a factor of approximately three as the wind speed increased from 6.3 to 8.1 m s^{-1}. The profiles also indicate that the value of ε decreases significantly within the viscous sublayer. Below the viscous sublayer, ε decreases less rapidly up to a depth approximately equal to the RMS wave height. Below this depth, ε becomes approximately constant at all conditions and wind speeds. This indicates that within the wave field, the dissipation is significantly enhanced. The rate of kinetic energy dissipation normalized by the wall coordinates, shows that the dissipation was enhanced with respect to the constant stress layer.

The results also show that in the presence of surfactant, waterside friction velocity increases by 32% and 50% at the lower and higher wind speeds, respectively, as compared to the clean surface. The value of the friction velocity computed from the viscous stress is lower than that computed from the fit to the mean logarithmic velocity profile within the buffer layer (i.e. beneath the viscous sublayer) at both wind speeds and for both surface conditions. It has been argued that the near-surface layer beneath the

wind-shear driven air-water interface is not a constant stress layer and that the turbulent shear stress and hence the friction velocity is expected to increase with depth.

In Chapter 4, the characteristics of the parasitic capillary waves were investigated. A visual scheme based on the DPIV vorticity fields and the surface profiles was developed to detect and quantify parasitic capillary waves. The PDF's of the wave amplitude show that the amplitude of the capillary waves is reduced due to the surfactant. However, the PDF's of the wavelength show that at the lower wind speed, the size of the capillary waves does not change with the surface condition. Whereas, at the higher wind speed, the length of the capillary waves increases slightly in the presence of surfactant. As the wind speed increased from 6.3 to 8.1 m s^{-1}, the average vorticity of the parasitic capillary wave increased by approximately 40-50%. The results show that in the presence of surfactant, the number of capillary waves is reduced by 50-70%. The results also show that the number of gravity waves with parasitic capillary wave increases with wind speed. In the presence of surfactant, the number of gravity waves with parasitic capillary waves decreased by 60% and 30% at the lower and higher wind speed, respectively.

Later in Chapter 4, a scheme was developed to detect microscale breaking waves based on the wake signature in the infrared images. In this technique, only those microscale breaking waves were considered that appeared at the location of the DPIV field of view in the infrared images. The results show that the percentage of microscale breaking waves reduced by approximately 50% at both wind speeds in the presence of surfactant. Also, for a given surface condition, the percentage of breaking waves does not change significantly with wind speed. The investigation of the datasets of the detected parasitic capillary waves and microscale breaking waves revealed that beneath the clean

surface, 91- 95% of the capillary waves appeared on the incipient breaking crests. In the presence of surfactant, this percentage was reduced to 75% at both wind speeds. The results show that the parasitic capillary waves that ride on the gravity wave crests are related to the wave breaking process. A conceptual model was developed to define the impact of capillary waves on the breaking process. It was observed that the number of capillary waves has a direct impact on the number of microscale breaking waves. Thus, it was conclude that the primary reason for the reduction in the percentage of microscale breaking waves beneath the surfactant-contaminated surfaces is the damping of capillary waves by the surfactant.

The investigation of the vorticity fields beneath contaminated surface shows a layer of enhanced vorticity immediately below the surface. This layer is comprised of counterclockwise vorticity. This thin layer of counterclockwise vorticity coincides with the region where the mean velocity gradients are significantly larger beneath the surfactant-contaminated surface as compared to a clean surface. Moreover, in breaking process, the enhancement of vorticity in the crest region of contaminated surface is due to the superposition of strong counterclockwise mean shear and the coherent structures generated by microscale breaking waves.

5.2 Suggestions for Future Work

In this thesis we have presented results that showed the significant impact of surfactant on the flow beneath short gravity waves and the parasitic capillary waves, which influences microscale wave breaking process. However, there are many issues that should be explored in the future to further increase our understanding of this

phenomenon. One of the fundamental issues to be resolved is the investigation of the vortex shedding by the parasitic capillary waves during the breaking process, for both clean and contaminated surfaces. Another important issue to be investigated is the effect of the variation in the surfactant concentration on the near-surface flow, especially on the parasitic capillary waves and microscale breaking waves.

REFERENCES

AGRAWAL, Y. C., TERRAY, E. A., DONELAN, M. A., HWANG, P. A., WILLIAMS III, A. J., DRENNAN, W. M., KAHMA, K. K. & KITAIGORODSKII S. A. 1992 Enhanced dissipation of kinetic energy beneath surface waves. *Nature*. **359**. 219-220.

AGÜÍ, J. C. & JIMÉNEZ, J. 1987 On the performance of particle tracking. *J. Fluid Mech.* **185**, 447-468.

BANNER, M. L. & PEIRSON W. L. 1998 Tangential stresses beneath wind-driven air-water interface. *J. Fluid Mech.*, **364**, 115-145.

BANNER, M. L. & PEREGRINE, D. H. 1993 Wave breaking in deep water. *Ann. Rev. Fluid Mech.* **25**, 373-397.

BANNER, M. L. & PHILLIPS, O. M. 1974 On the incipient breaking of small scale waves. *J. Fluid Mech.*, **65**, 647-656.

BENILOV, A. Yu., KOUZNETSOV O. A. & PANIN G. N. 1974 On the analysis of wind-induced disturbances in the atmospheric turbulent surface layer, *Boundary-Layer Met.* **6**, 269-285.

BENILOV, A. Yu., B. N. Filyushkin, 1970 Application of methods of lineart filteration on the analysis of fluctuaions in the surface layer of the sea, *Izv ,Acad. Sci. USSR, Atmos. OceanicPhys., Engl. Transl., 6, 477-482.*

Bock, E. J. , T. Hara, N. M. Frew, & W. R. McGillis, 1999 Relationship between air-sea gas transfer and short wind waves, *J. Geophys. Res.*, **104** C11, 25,821-25,831.

CENICEROS, H. D. 2003 The effects of surfactants on the formation and evolution of capillary waves *Physics of Fluids*, **15**, 245-256.

CHEUNG, T. K. & STREET, R. L. 1988 The turbulent layer in the water at an air-water interface. *J. Fluid Mech.* **194**, 133-151.

CINI, R. & LOMBARDINI, P. P., 1981 Experimental evidence of a maximum in the frequency domain of the ratio of ripple attenuation in monolayered water to that in pure water *J. Colloid Interface Sci.* **81**,125-131.

COWEN, E. A. & MONISMITH S. G. 1997 A hybrid digital particle tracking velocimetry technique. *Exp. Fluids* **22**, 199-211.

COX, C. S. 1958 Measurement of slopes of high frequency wind waves. *J. Mar. Res.* **16** 199-225.

CRAPPER, G. D. 1970 Non-linear capillary waves generated by steep gravity waves. *J. Fluid Mech.* **40** 149-159.

DABIRI, D. & GHARIB, M. 1997 Experimental investigation of the vorticity generation within a spilling water wave. *J. Fluid Mech.*, **330**, 113-139.

DEAN, R. G. & DALRYMPLE, R. A. 1991 Water Wave Mechanics for Engineers and Scientists. World Scientific.

DONELAN, M. A. 1990 Air-sea interaction. In The Sea: *Ocean Engineering Science*, 239-292. Wiley.

DORON, P., BERTUCCIOLI, L., KATZ, J. & OSBORN T. R. 2001 Turbulence Characteristics and Dissipation Estimates in the Coastal Ocean Bottom Boundary Layer from PIV Data. *J. Phys. Oceanogr.*

DUNCAN, J. H., PHILOMEN, V., BEHRES, M. & KIMMEL J. 1994 The formation of a spilling breaker. *Phys. Fluids* **6(8)**, 2558-2560.

DUNCAN, J. H., QIAO, H., PHILOMEN, V., & Wenz, A. 1999 Gentle spilling breakers: crest profile evolution. *J. Fluid Mech.* **379**, 191-222.

DUNCAN, J. H. 2001 Spilling Breakers. *Ann. Rev. Fluid Mech.* **33**, 519-547.

EBUCHI, N., KAWAMURA, H. & TOBA Y. 1987 Fine structure of laboratory wind-wave surfaces studied using an optical method. *Boundary-Layer Met.* **39**, 133-151.

Elkamash & Loewen, M. 2004 (in preparation).

FINCHAM, A. M. & SPEDDING G. R. 1997 Low cost, high resolution DPIV for measurement of turbulent fluid flow. *Exp. Fluids* **23**, 449-462.

HINZE, J. O. 1975 Turbulence. McGraw Hill.

HSU, C.T., HSU, E. Y. & STREET, R. L. 1981 On the structure of turbulent flow over a progressive water wave: theory and experiment in a transformed, wave-following coordinate system. *J. Fluid Mech.* **105**, 87-117.

HUSSAIN, A. K. M. F. 1983 Coherent structures-reality and myth. *Phys. Fluids.* **26**, 2816-2850.

JESSUP, A. T., ZAPPA, C. J. & YEH, H. 1997a Defining and quantifying microscale wave breaking with infrared imagery. *J. Geophys. Res.*, **102**, 23145-23153.

JESSUP, A. T., ZAPPA, C. J., LOEWEN, M. R. & HESANY, V. 1997b Infrared remote sensing of breaking waves. *Nature*. **385**, 52-55.

JIANG, J. Y., STREET, R. L. & KLOTZ, S. P. 1990 A study of Wave-Turbulence Interaction by Use of a Nonlinear Water Wave Decomposition Technique. *J. Geophys. Res.*, **95**, 16037-16054.

JONES, I. S. F., & TOBA Y. 2001 Wind stress over the ocean. *Cambridge University Press.*

KENNEDY, J. B. & NEVILLE, A. M. 1976 Basic Statistical Methods for Engineers & Scientists. Harper & Row, Publishers, Inc.

KITAIGORDOSKII S. A. & LUMLEY J.L. 1983 Wave-Turbulence Interactions in the Upper Ocean. Part I: The Energy Balance of the Interacting Fields of Surface Wind Waves and Wind-Induced Three-Dimensional Turbulence. *J. of Physic. Ocean.* **13**, 1977-1987.

KUNDU, P. K. & COHEN, I. M. 2002 Fluid Mechanics. Academic Press.

LONGUET-HIGGINS, M. S. 1963 The generation of capillary waves by steep gravity waves. *J. Fluid Mech.* **16**, 138-159.

LONGUET-HIGGINS, M. S. 1992 Capillary rollers and bores. *J. Fluid Mech.* **240**, 659-679.

LONGUET-HIGGINS, M. S., CLEAVER R. P. 1994 Crest instability of gravity waves. Part 1 . The almost- highest wave. *J. Fluid Mech.* **258**, 115-129.

LUCASSEN-REYNDERS, E. H., & LUCASSEN, J. 1969 Properties of capillary waves. *Adv. Colloid Interface Sci.* **2**, 347-395.

LUCASSEN, J. 1982 Effect of surface-active material on damping of gravity waves: A reappraisal. *J. Colloid Interface Sci.* **85**, 52-58.

LUMLEY J. L. & TERRAY E. A. 1983 Kinematics of Turbulence Convected by a Random Wave Field. *J. Phys. Oceanogr.* **13**, 2000-2007.

MARXEN, M. 1998 "*Particle Image Velocimetry in Strömungen mit starken Geschwindigkeitsgradienten,*" (Diplom Thesis, Fakultät für Physik und Astronomie, Ruprecht-Karls-Universität Heidelberg.

Mc KENNA, S. P., 2000 "*Free- surface turbulence and air-water gas exchange,*" (Diplom Thesis, Massachusetts Institute of Technology and Woods Hole Oceanographic

MELVILLE, W. K. 1996 The role of surface-wave breaking in air-sea interaction. *Ann. Rev. Fluid Mech.* **28**, 279-321.

MITSUYASU, H. & T. HONDA 1986 The effects of surfactant on certain air-sea interaction phenomena. In: Wave dynamics and radio probing of the ocean, O. M. Phillips and K. Hasselmann, Eds. Plenum Publishing Company, 95-115

MITSUYASU, H. & T. HONDA 1982 Wind-induced growth of the water waves. *J. Fluid Mech.* **123**, 425-442.

OKUDA, K. 1982 Internal flow structures of short wind waves, I, On the internal vorticity structures. *J. Oceanogr. Soc. Jpn.* **38**, 28-42.

PEIRSON, W. L. & BANNER, M. L. 2003 Aqueous surface layer flows induced by microscale breaking wind waves. *J. Fluid Mech.* **479**, 1-38.

PHILLIPS, O. M. 1981 The dispersion of short wavelets in the presence of a dominant long wave. *J. Fluid Mech.* **107**, 465-485.

PRASAD, A. K., ADRIAN, R. J., LANDRETH, C. C. & OFFUTT, P. W. 1992 Effect of resolution on the speed and accuracy of particle image velocimetry interrogation. *Exp. Fluids* **13**, 105-116.

RUSSELL, J. S. 1844 Report of the committee on waves. *Proc. Brit. Ass. Adv. Sci., 7th Meeting, York, 311-390.*

SCHLICHTING, H. 1979 Boundary-Layer Theory. McGraw-Hill.

SIDDIQUI, M. H. K., LOEWEN, M. R., RICHARDSON, C., ASHER, W. E. & JESSUP, A. T. 2001 Simultaneous particle image velocimetry and infrared imagery of microscale breaking waves. *Phys. Fluids,* **13**, 1891-1903.

SIDDIQUI, M. H. K. 2002 Laboratory measurements of the flow beneath microscale breaking waves, Doctor of Philosophy thesis, Department of Mechanical and Industrial Engineering, University of Toronto.

SIDDIQUI, M. H. K., LOEWEN, M. R., ASHER, W. E. & JESSUP, A. T. 2004 Coherent Structures Beneath Wind Waves and their Influence on Air-Water Gas Transfer. *J. Geophys. Res.* **109**, C03024, 1-14.

SIDDIQUI, M. H. K., LOEWEN 2004 Chracterisitic of the Wind Drift Layer and Microscale Breaking Waves. *J. Fluid Mech.* (in press).

SOLOVIEV, A. V., VERSHINSKY, N. V. & BEZVERCHINII, V. A. 1988 Small-scale turbulence measurements in the thin surface layer of the ocean. *Deep-Sea Res.* **35**, 1859-1874.

TERRAY, E. A., DONELAN M. A., AGRAWAL Y. C., DRENNAN W. M., KAHAMA K. K., WILLIAMS III, A. J., HWANG, P. A. & KITAIGORODSKII, S. A. 1996 Estimates of Kinetic Energy Dissipation under Breaking Waves. *J. Phys. Oceanogr.* **26**, 792-807.

THAIS, L. & MAGNAUDET J. 1996 Turbulent structure beneath surface gravity waves sheared by the wind. *J. FluidMech.* **328**, 313-344.

VERON, F. & MELVILLE, W. K. 1999 Pulse-to-pulse coherent Doppler measurements of waves and turbulence. *J. Atmos. Oceanic. Technol.* **16**, 1580-1597.

WU, J. 1971 An Estimation of Oceanic Thermal-Sublayer Thickness. *J. Phys. Oceanogr.* **1**, 284-286.

WU, J. 1975 Wind-induced drift current. *J. Fluid Mech.* **68**, 49-70.

ZAPPA, C. J. 1999 Microscale wave breaking and its effect on air-water gas transfer using infrared imagery. Ph. D. thesis, Applied Physics Laboratory, Department of Civil and Environmental Engineering, University of Washington.

ZAPPA, C. J., ASHER, W. E. & JESSUP A. T. 2001 Microscale wave breaking and air-water gas transfer. *J. Geophys. Res.*, **106**, 9385-9391.

ZAPPA, C. J., Asher, W. E., Jessup, A. T., Klinke, J. & Long, S. R. 2004 Microbreaking and the Enhancement of Air-Water Gas Transfer Velocities. *J. Geophys. Res.* **109**, No. C8, C08S16, 10-1029/2003JC0018002.

Appendix A

Error Estimate for the DPIV Measurements

The total error in the DPIV measurements is the sum of the errors due to velocity gradients, particle diameter, out-of-plane motion, peak locking and AGW interpolation (Cowen and Monismith 1997). The particle diameter in the present study was 0.43 pixels. Particles smaller than one pixel always occupy one pixel area in an image. Therefore, the true position of the particle within a pixel could not be resolved.

Peak locking is the bias error that occurs when the estimated location of the correlation peak is shifted towards the nearest integer value. Fincham and Spedding (1997) found that peak locking occurs in any type of Image Velocimetry technique where sub-pixel determination of the correlation peak is attempted.

We expect that the largest errors occur in the top 3.6 mm layer of water at the highest wind speed for the contaminated condition since the velocity gradients are larger in the presence of surfactant in the near-surface region. We used the results of Cowen and Monismith (1997) and Prasad *et al.* (1992) to estimate the errors in the DPIV data. The errors were estimated using the raw displacement data in the top 3.6 mm layer of water at the wind speed of 8.1 m s^{-1} in the presence of surfactant. The PIV error computation procedure described in Siddiqui (2002) was used to estimate the velocity and vorticity errors. Following is the detailed step-by-step procedure for the error estimation in the DPIV data.

1. The mean values of the largest velocity gradients in the streamwise and vertical directions were obtained from the raw DPIV data. The mean streamwise velocity gradient was 3.5%, and the mean vertical velocity gradient was zero. Therefore, the errors were estimated for the streamwise velocity base on the mean streamwise velocity gradient.

2. The errors due to velocity gradient were estimated using figure 5(a) in Cowen and Monismith (1997), which is the plot of the errors as a function of the particle size base on velocity gradient of 3%. The errors corresponding to a particle diameter of 1.0 pixel were estimated because this was the smallest particle diameter that Cowen and Monismith (1997) considered. The errors for a particle diameter of 1.0 pixel were,

$$E_u = 0.1 \text{ pixels} \tag{A.1}$$

where E_u is the errors associated with the streamwise velocity.

3. As mentioned above, the particle diameter was 0.43 pixels in the present study, so the errors corresponding to smaller particle diameter should be accounted for. The bias (peak locking) and RMS errors due to a particle diameter of 0.43 pixels were estimated using figure 13 in Prasad *et al.* (1992), which shows the errors as a function of particle diameter. Using this figure, we found that the errors associated with a particle diameter of 0.43 pixels would be 35% larger than the errors associated with a particle diameter of 1.0 pixel. The final error estimate based on a 35% increase in errors was,

$$E_u = 0.135 \text{ pixels} \tag{A.2}$$

4. The in-plane vertical displacement on the basis of the mean and standard deviation of the vertical displacement was,

$$W = \overline{w} + \sigma_w = 4.1 \text{ pixels} \approx 144 \text{ μm} \quad \text{(A.3)}$$

The out-of-plane motion was expected to be less than or equal to the vertical displacement. The out of plane motion was negligible because it was less than the thickness of the laser light sheet, which was 300 μm.

5. The error corresponding to AGW interpolation was estimated from figure 5(f) in Cowen and Monismith (1997), and it was 0.08 pixels.

The total the streamwise velocity error was estimated to be,

$$E_u = 0.135 + 0.08 = 0.215 \text{ pixels} \quad \text{(A.4)}$$

This error in velocity units is,

$$E_u = 0.3 \text{ cm s}^{-1} \quad \text{(A.5)}$$

We assumed that the errors in the horizanotal and the vertical velocities were the same. Since the larger velocity gradients (i.e. $\partial u / \partial y$) will cause errors in both u and w. The resultant velocity, V, can be computed as $V = \sqrt{u^2 + w^2}$. Thus the error in V can be computed as,

$$E_V = \sqrt{E_u^2 + E_v^2} = 0.42 \text{ cm s}^{-1} \quad \text{(A.6)}$$

The errors in the vorticity measurements were estimated using the errors in the velocity measurements. The vorticity (ω) is given by,

$$\omega = \frac{\partial u}{\partial y} - \frac{\partial w}{\partial x} \quad \text{(A.7)}$$

where, $\partial u / \partial y$ and $\partial w / \partial x$ are the streamwise and vertical velocity gradients, respectively. The streamwise velocity gradient can be written as,

$$\frac{\partial u}{\partial y} = \frac{\Delta u}{\Delta y} \tag{A.8}$$

where, $\Delta u = u_1 - u_2$, is the streamwise velocities difference at two grid points and, Δy is the vertical distance between the two grid points. In this study, the central difference method was used to compute vorticity. The variance of the errors (E^2) in Δu can be estimated as,

$$E^2(\Delta u) = E^2(u_1) + E^2(u_2) = 2\,E^2(u) = 2\,(0.3)^2 = 0.18 \text{ cm}^2 \text{ s}^{-2} \tag{A.9}$$

where $E^2(\Delta u)$, $E^2(u_1)$ and $E^2(u_2)$ are the variance of the errors in Δu, u_1 and u_2, respectively (Kennedy and Neville 1976). The vertical distant between two grid points (Δy) in the present case for central scheme is equal to 0.168 cm. The variance of the errors in $\partial u / \partial y$ is then given by,

$$E^2(\Delta u/\Delta y) = E^2(\Delta u)/\Delta y = 0.18/0.168 = 1.07 \text{ s}^{-2} \tag{A.10}$$

We assumed that the errors in w were equal to those in u, and the vertical and horizontal differences between two grid points are the same in present study; therefore, variance of the errors in $\partial w / \partial x$ is given by,

$$E^2(\Delta w/\Delta x) = E^2(\Delta w)/\Delta x = 0.18/.168 = 1.07 \text{ s}^{-2} \tag{A.11}$$

The variance of the errors in the vorticity, $E^2(\omega)$, is then given by,

$$E^2(\omega) = E^2(\Delta u/\Delta y) + E^2(\Delta w/\Delta y) = 2.17 \text{ s}^{-2} \tag{A.12}$$

Thus, the RMS error in the vorticity, $E(\omega)$, is given by,

$$E(\omega) = \sqrt{E^2(\omega)} = 1.5 \text{ s}^{-1} \tag{A.13}$$

Hence, the errors in the instantaneous velocity and vorticity estimates are ± 0.42 cm s^{-1} and ± 1.5 s^{-1}, respectively.